



# BRNO UNIVERSITY OF TECHNOLOGY

VYSOKÉ UČENÍ TECHNICKÉ V BRNĚ

## CENTRAL EUROPEAN INSTITUTE OF TECHNOLOGY BUT

STŘEDOEVROPSKÝ TECHNOLOGICKÝ INSTITUT VUT

## MAGNETIC VORTEX BASED MEMORY DEVICE

PAMĚTOVÁ BUNKA ZALOŽENÁ NA MAGNETICKÝCH VORTEXECH

**DOCTORAL THESIS**

DIZERTAČNÍ PRÁCE

**AUTHOR**

AUTOR PRÁCE

**Meena Dhankhar**

**SUPERVISOR**

ŠKOLITEL

**Ing. Michal Urbánek, Ph.D.**

**BRNO 2020**

# Abstract

Magnetic vortices are characterized by the sense of in-plane magnetization circulation and the polarity of the vortex core, each having two possible states. As a result, there are four possible, stable magnetization configurations that can be utilized for a multibit memory device. This thesis presents the selective writing of vortex states by electric current pulses and electric readout of the vortex states in a magnetic disk. Prior to the electric measurements, static readout of vortex states is carried out by MFM, and then by MTXM, after applying different current pulses to switch the vortex states. Later, we added all-electric static and finally dynamic readout of the vortex state.

Vortex circulation control is based on a geometrical asymmetry formed by cropping one side of the magnetic disk. The flat edge of the disk provides a preferential direction defining the sense of circulation during the nucleation process. Polarity control is generally achieved in a two-step process. Firstly, a homogeneously magnetized perpendicular magnetic anisotropy layer placed at the bottom of the disk imposes a defined vortex polarity upon nucleation of a vortex. Secondly, a fast-current pulse is used to toggle switch the vortex polarity, if needed. Hence, we are able to set the desired vortex state by sending a low amplitude nanosecond pulse that sets the circulation followed by a high amplitude picosecond pulse, which sets the polarity. The vortex states are then detected by electric spectroscopy via the anisotropic magnetoresistance effect. The samples for all the static and dynamic measurements are prepared by e-beam lithography and the lift-off technique.

# Abstrakt

Magnetické vortexy jsou charakterizovány směrem stáčení magnetizace a polarizací vortexového jádra, přičemž každá z těchto veličin nabývá dvojice stavů. Ve výsledku jsou tak k dispozici čtyři možné stabilní konfigurace, čehož může být využito v multibitových paměťových zařízeních. Tato dizertační práce se zabývá selektivním zápisem stavů magnetického vortexu v magnetickém disku pulzem elektrického proudu stejně jako jejich následným elektrickým čtením. Před samotnou realizací elektrických měření byla provedena statická měření přepínání stavů vortexu pomocí různých proudových pulzů v kombinaci s technikami MFM a následně MTXM. Následně byl realizován dynamický odečet stavu vortexu kompletně založený na elektrických měřeních.

Ovládání cirkulace vortexu je založeno na geometrické asymetrii vytvořené oříznutím magnetického disku a vytvořením fazety. Plochý okraj disku definuje preferenční smysl stáčení cirkulace během procesu nukleace vortexu. Řízení polarity se obvykle provádí ve dvou krocích. V prvním kroku, homogenně magnetizovaná vrstva s kolmou magnetickou anizotropií umístěná na dně disku definuje výchozí polaritu vortexu v době nukleace. V druhém kroku, je-li to nutné, je polarita vortexu přepnuta pomocí rychlého proudového pulzu. Proto je možné nastavit požadovaný stav cirkulace vysláním nanosekundového pulsu s nízkou amplitudou, následované nastavením polarity pikosekundovým pulsem s vysokou amplitudou. Stav vortexů jsou pak detekovány elektrickou spektroskopií prostřednictvím anizotropní magnetorezistence. Vzorky pro všechna statická a dynamická měření byly připraveny pomocí elektronové litografie v kombinaci s lift-off procesem.

## Keywords

Magnetic vortex, Magnetization dynamics, Electron-beam lithography, Magnetic microscopy, Magnetoresistance, Polarity switching, Circulation switching, Electric writing and readout.

## Klíčová slova

Magnetický vortex, dynamika magnetizace, elektronová litografie, magnetická mikroskopie, magnetorezistivita, přepínání polarity, přepínání cirkulace, elektrický zápis a čtení.

DHANKHAR, Meena. *Magnetic vortex based memory device*. Brno, 2020. Doctoral thesis. Brno University of Technology. Central European Institute of Technology BUT. Supervisor Michal URBÁNEK.

I hereby declare that I have written my thesis titled *Magnetic vortex based memory device* independently, under the guidance of the supervisor, Ing. Michal Urbánek, Ph.D, and using the technical literature and other sources of information, which are all adequately cited in the thesis and detailed in the list of literature at the end of the thesis.

Ing. Meena Dhankhar

Firstly, I would like to express my sincere gratitude to my supervisor Ing. Michal Urbánek, Ph.D. His outstanding diligence, skillful guidance, immense support, and motivation have paved my way during the whole Ph.D. study and my journey in CEITEC. I could not have imagined having a better supervisor for my Ph.D. study.

Then my admiration and gratitude go to Prof. RNDr. Tomáš Šikola, Ph.D., for continuous support during my Ph.D. study and related research, for his patience, motivation, and immense knowledge. He is a humble and very supportive person.

I would like to thank prof. RNDr. Jiří Spousta, Ph.D., for teaching me swimming and for his support. I am also grateful to thank Ing. Vojtěch Uhlíř, Ph.D., for his skillful guidance and time-to-time discussion about my work.

I would like to thank my family for their continuous support and love. I want to thank my colleagues for surrounding me with a generous and cheerful environment, discussion, help, and useful hacks to have me a joyful life in Brno as a foreigner.

Ing. Meena Dhankhar

# Contents

<b>1. Introduction and Goals</b>	<b>3</b>
<b>2. Theoretical Background</b>	<b>6</b>
2.1 Micromagnetic energies	6
2.2 Magnetization dynamics	9
2.3 Magnetic Vortex	10
2.4 Electrical transport measurements of vortex dynamics	26
<b>3. Characterization Techniques</b>	<b>30</b>
3.1 Magnetic force microscopy	30
3.2 Magnetic transmission X-ray microscopy (MTXM)	31
3.3 Magneto-optical Kerr effect	32
3.4 Detection of vortex circulation using Anisotropy magnetoresistance (AMR)	33
3.5 Heterodyne detection of vortex states by dynamic AMR measurement	35
<b>4. Sample Fabrication</b>	<b>39</b>
4.1 Lithography techniques for nanofabrication	39
4.2 Ion beam etching using the negative mask	42
4.3 Sample preparation for MTXM	43
4.4 Sample preparation for dynamic AMR measurement	48
4.5 Sample preparation for combined (Oersted field and spin torque excitation) measurements	52
<b>5. Experiments and Discussion</b>	<b>54</b>
5.1 Static readout of vortex states by MFM	54
5.2 Polarity control by PMA layer	56
5.3 Electric readout of vortex states	61
5.4 All electric control (switching and readout) of vortex states	66
5.5 Reliability of vortex states switching	72
5.6 Resonance frequency splitting	73
<b>6. Conclusion</b>	<b>75</b>
<b>Appendix A</b>	<b>77</b>
<b>Appendix B</b>	<b>80</b>

<b>References .....</b>	<b>82</b>
<b>List of acronyms and abbreviations .....</b>	<b>96</b>
<b>List of Symbols .....</b>	<b>98</b>
<b>Own Publications .....</b>	<b>100</b>

# 1. Introduction and Goals

The idea of using the electron spin degree of freedom is one of the promising trends for future electronics. Interestingly, the electron spin can be used in association with the electron charge for the added functionality of semiconductor devices. The concept of electronics with a ‘spin’ degree of freedom is known as spintronics. Spintronic devices are expected to have significant improvement in terms of size, speed, information density, power consumption, non-volatility, and robustness. The main applications of spintronics are in data storage devices [1, 2]. Other applications include magnetic sensors [3], magnetic vortex-based transistors [4], logic circuits, or radio-frequency (rf) devices [5–7]. Recent studies have shown magnetic vortices as spin-wave emitters [8] using two antiferromagnetically coupled disks in a heterostructure, providing a system with much higher eigenfrequencies when compared to a single magnetic disk with a vortex state.

Current memory technology (DRAM) has a significant drawback in their volatility, which means that the stored data needs to be refreshed continuously, consuming power even when no operation is performed. Novel types of memories, such as non-volatile magnetic random-access memory (MRAM) [9–11], are coming into the market as a low-power alternative to the standard semiconductor-based memory devices [12]. In MRAM, information is stored in form of relative alignment of magnetization of the memory cell magnetic layer and read out by monitoring variations in their magneto resistivity. The antiparallel alignment of the magnetic layers leads to a high resistance state, and parallel alignment leads to a low resistance state, where each state represents a logic ‘0’ or ‘1’. This memory technology can be further improved by exploiting the properties of a magnetic vortex [13–20].

The vortices are curling magnetization structures [21–29] formed in micron or nano-sized magnetic disks and polygons [30–40]. They have four different magnetization configurations (vortex states) that can be used for a multibit memory device and for performing logic operations [41]. The vortex states are characterized by the polarity of vortex core, pointing either up ( $p = +1$ ) or down ( $p = -1$ ) and by the circulation of the magnetization in the plane of the disk, curling either counterclockwise ( $c = -1$ ) or clockwise ( $c = +1$ ). The resulting four possible states are independent and can also provide a basis for multibit memory cells and logic gates. They can be controlled by applying a static out-of-plane (polarity control [42]) or in-plane (circulation control [43]) magnetic fields. However, both the polarity and the circulation can be switched more effectively in a dynamic regime by using fast-rising magnetic fields [44–46].

The goal of the work is to study the process of selective switching of a magnetic vortex into the desired vortex state and to build a prototypical device that allows fully electric writing and readout of vortex states at the nanosecond timescale. The control of polarity as well as of circulation has been experimentally demonstrated separately, but an experimental demonstration of a simple allowing of selective switching into each of four vortex states together with all-electrical detection is still missing.

To dynamically switch the vortex core polarity, the vortex core must be driven into a gyrotropic precession either by an alternating magnetic field [44, 47] or by a magnetic field pulse [48]. The



switching proceeds through the creation and subsequent annihilation of a vortex-antivortex pair due to a dynamical distortion of the vortex core. This distortion is caused by an effective field, called the gyrofield, which is proportional to the vortex core velocity [49]. The vortex core is switched when its velocity exceeds a critical velocity for switching, which is approx.  $320 \text{ m/s}^{-1}$  for Permalloy. This approach has the disadvantage that the vortex core polarity can be only toggle switched from one polarity to another and back without the possibility of controlling the final polarization state. This can be avoided by using rotating in-plane fields to excite the gyrotropic motion of the vortex core [50]. In this approach, vortex gyration is excited, and the core polarity can be switched only if the sense of the rotating field coincides with the vortex gyration sense defined by the vortex polarity. It has also been shown that the selective switching of the vortex core polarity is possible by the excitation of the azimuthal spin waves using several periods [51], by using a perpendicular magnetic anisotropy layer [52, 53], or even a single period [54] of the rotating in-plane magnetic fields in the GHz frequency range.

Selective switching of the circulation requires expelling the vortex core out of the disk and then reforming a new vortex with a required sense of spin circulation. It can be achieved by using a fast-rising in-plane magnetic field pulse that drives the vortex core into the far-from-equilibrium gyrotropic precession and annihilates the vortex during the first half-period of the precessional motion if the vortex core reaches the disk boundary [45]. The resulting circulation of the new vortex is controlled by a disk asymmetry [55, 56] and by the direction of the magnetic field pulse. This approach allows for fast switching with the field amplitudes reduced by 50% when compared to the switching using static fields.

Most of the experiments on magnetic vortices performed so far used advanced and often very complicated magnetic microscopy methods for the identification of the individual vortex states. For the successful application of magnetic vortices as the multibit memory cells, an electric readout of all vortex states must be performed. Nakano et al. presented a dynamic method of electric readout of the polarity of the vortex core [57, 58]. The vortex core is driven into gyrotropic precession, and the magnetoresistive signal is detected in the center of the magnetic vortex memory cell via a small magnetic tunnel junction [59] (MTJ). The phase shift between driving and measured signal enables to identify the vortex core polarity. A magnetoresistive readout of the vortex circulation should be possible via a ‘fixed’ vortex layer using the exchange bias effect and magnetic vortex imprinted into an antiferromagnet [60, 61]. However, switching the vortex circulation in these configurations may prove problematic, as any magnetic layer in the vicinity of the magnetic disk can influence the nucleation of the newly formed vortex during circulation reversal.

Although the simultaneous control of circulation and polarity has already been demonstrated [53], and the readout is done by magnetic force microscopy (MFM). Still, the electrical readout of vortex states has higher significance to provide a sufficient statistic. To write the circulation and polarity independently, a nanosecond and picosecond current pulse were used, respectively. In contrast, the switching of polarity was controlled by the PMA layer, and the circulation switching was controlled by the shape anisotropy of the disk. There was no need to switch the circulation or polarity previously or later because the current pulses don’t affect the other state.

This doctoral thesis is divided into six chapters. Following the introduction, Chapter 2 explains the micromagnetic theory basics, which involve energies at play in different vortex states and vortex dynamics. The chapter also explains the principle of switching, different vortex states, dc voltage

rectified spectrum equation, and circulation and polarity estimation. Chapter 3 is devoted to the characterization techniques used during doctoral work. Chapter 4 is dedicated to the fabrication of samples by the lithography technique. The most used technique was electron beam lithography (EBL), followed by the deposition and sample check. Chapter 5 describe the experimentally acquired results, mainly by an electrical method and the discussion about the writing and readout of different vortex states and their statistic. Finally, Chapter 6 concludes the work.

## 2. Theoretical Background

### 2.1 Micromagnetic energies

The magnetic state of an object is a result of minimizing the total free energy, and it reflects either a local or an absolute energy minimum [62]. There are several contributions to total energy [63] viz.

$$\varepsilon_{tot} = \varepsilon_d + \varepsilon_{ex} + \varepsilon_a + \varepsilon_z + \dots \quad (2.1)$$

The significant contributions are the dipolar energy  $\varepsilon_d$ , exchange energy  $\varepsilon_{ex}$ , anisotropy energy  $\varepsilon_a$ , and Zeeman energy  $\varepsilon_z$ . Other contributions to the total energy may also appear due to the applied stress, the magnetostriction, the Dzyaloshinskii - Moriya interaction (DMI), etc...

#### *Dipolar energy*

The dipolar energy arises from the interaction of magnetic moments, which creates a stray field and demagnetizing field. The stray field acts outside a magnet and the demagnetizing field within it. The dipolar energy, also called demagnetizing energy, reads as:

$$\varepsilon_d = -\frac{1}{2}\mu_0 \int_V \vec{M} \cdot \vec{H}_d dV . \quad (2.2)$$

Factor  $\frac{1}{2}$  is introduced to avoid counting twice the interaction of the moment A with B and B with A [64].  $\vec{H}_d$  is the demagnetizing field, opposes the magnetization which creates it and is given as:

$$\vec{H}_d = -\hat{N}\vec{M} , \quad (2.3)$$

Here,  $\hat{N}$  is the demagnetizing factor or the demagnetizing tensor.  $\vec{M}$  is the magnetization vector and can be defined as the volume density of magnetic dipoles. In materials, magnetic induction  $\vec{B}$  is defined as:  $\vec{B} = \mu_0(\vec{H} + \vec{M})$ , where  $\mu_0 = 4\pi \times 10^{-7} H/m$  is the permeability of free space and  $\vec{H}$  is the magnetic field intensity.

#### *Exchange energy*

The exchange interaction is described by the Heisenberg Hamiltonian [62, 65, 66]

$$\mathcal{H}_{ex} = -\sum_{i \neq j} J_{i,j} \vec{S}_i \cdot \vec{S}_j , \quad (2.4)$$

where  $J_{ij}$  is the exchange constant. The value  $J_{ij} > 0$  indicates the ferromagnetic alignment between the neighboring spins and  $J_{ij} < 0$  indicates the antiferromagnetic alignment between the neighboring spins  $S_i$  and  $S_j$  [67].

In a magnetic continuum, the exchange energy [68, 69] can be expressed by the integral over the sample volume  $V$ :

$$\varepsilon_{ex} = \int_V A \left[ (\nabla m_x)^2 + (\nabla m_y)^2 + (\nabla m_z)^2 \right] dV, \quad (2.5)$$

where  $A$  is the exchange stiffness ( $\text{Jm}^{-1}$ ) and  $m_x, m_y, m_z$  are the components of the unit magnetization vector  $\vec{m}$ . Some energy relations are concerned only with the local direction of the magnetization, not with the magnitude. So, it is appropriate to define a unit vector pointing in the direction of the magnetization as:

$$\vec{m} = \frac{\vec{M}}{M_0}, \quad (2.6)$$

where  $\vec{M}$  is the magnetization vector, and  $M_0$  is the spontaneous magnetization. Both the magnetization vector  $\vec{M}$  and spontaneous magnetization  $M_0$  is supposed to have a constant magnitude, but their direction varies from point to point as of the unit vector [70, 71].

The value of  $A$  reads:

$$A \sim J S^2 z_c / a_L, \quad (2.7)$$

where  $a_L$  is the lattice parameter,  $z_c$  is the number of atoms per unit cell, and  $J$  is the exchange constant. The typical value of  $A$  for Permalloy is  $13 \times 10^{-12} \text{ Jm}^{-1}$  and  $31 \times 10^{-12} \text{ Jm}^{-1}$  for cobalt [72]. The exchange interaction is isotropic.

Further, the competition between the exchange energy and the dipolar energy is given by the exchange length [62].

$$l_{ex} = \sqrt{\frac{2A}{\mu_0 M_S^2}} \quad (2.8)$$

The exchange length value for both Permalloy and cobalt is 3.4 nm for  $M_S = 0.84 \times 10^6 \text{ Am}^{-1}$  and  $1.44 \times 10^6 \text{ Am}^{-1}$ , respectively [62].

### *Anisotropy energy*

The origin of the magnetocrystalline anisotropy is the spin-orbit coupling. The spin-orbit coupling causes the magnetization vector to align along a preferential crystallographic direction, called the easy axis [67]. In case of the uniaxial anisotropy [73], the first term of anisotropy energy is given as [62].

$$\varepsilon_a = \int_V K_u \sin^2 \theta \, dV, \quad (2.9)$$

where  $K_u$  is the anisotropy constant, and  $\theta$  is the angle between the magnetization vector and the easy axis.

### *Zeeman energy*

If an external magnetic field  $\vec{H}_{app}$  acts on a magnetic moment, it aligns the moment in the field direction. While a misalignment causes the Zeeman energy.

The Zeeman energy is given as follows [65]

$$\varepsilon_Z = -\mu_0 \int_V \vec{M} \cdot \vec{H}_{app} \, dV. \quad (2.10)$$

### *Other energy terms*

Above we have mentioned the four main energy terms that are always present in a magnetic system, but some other energy terms can also be found there.

- The local stress may be generated by the magnetostriction of ferromagnetic material when trying to change their shape and dimensions during magnetization [64].
- Low symmetry materials can exhibit weak antisymmetric coupling, called Dzyaloshinskii - Moriya interaction (DMI) [74, 75].

### *Effective field*

In the equilibrium state, the total energy must be minimized. This condition yields the effective magnetic field  $\vec{H}_{eff}$  [62]:

$$\vec{H}_{eff} = \frac{2A}{\mu_0 M_s} \nabla^2 \vec{m} - \frac{1}{\mu_0 M_s} \frac{\partial \varepsilon_a}{\partial \vec{m}} + \vec{H}_d + \vec{H}_{app}. \quad (2.11)$$

For which

$$\vec{M} \times \vec{H}_{eff} = 0, \quad (2.12)$$

holds. Equation (2.12) describes that the torque on the magnetization vanishes in equilibrium or minimum energy state.

Let us recall that the first term in the eq. (2.11) originates from the exchange energy, the second term from the anisotropy energy, the third term from the dipolar energy, and the last one from the Zeeman energy [67, 76].

## 2.2 Magnetization dynamics

The Larmor precession describes the precession of the magnetization vector around the effective magnetic field as [62, 77, 78]:

$$\frac{\partial \vec{M}}{\partial t} = -\gamma \vec{M} \times \mu_0 \vec{H}_{eff} , \quad (2.13)$$

Where  $\gamma = \frac{e}{2m_e}$  is the gyromagnetic ratio [77]. The torque produced by an effective magnetic field changes the magnetization vector in the torque direction. Then the precession of the magnetization vector around the effective magnetic field is given by the Larmor angular velocity  $\vec{\omega} = \gamma \mu_0 \vec{H}_{eff}$ . If the  $\vec{H}_{eff}$  is constant, the magnetic moment is precessing around the effective field in a circular motion as in Fig 2.1(a).

It is necessary to take the dissipation into account. Damping (or dissipation) term was added to the equation (2.13) to ensure the relaxation of magnetization to the direction of  $\vec{H}_{eff}$ . Historically, two different phenomenological approaches were proposed.

Landau and Lifshitz first described the damping in 1935, who proposed the dissipative term as [79]:

$$-\frac{\lambda}{M_s} [\vec{M} \times (\vec{M} \times \mu_0 \vec{H}_{eff})] . \quad (2.14)$$

where  $\lambda > 0$  is the speed of magnetization relaxation.

Then the Landau – Lifshitz equation (LL) written as [79, 80]:

$$\frac{\partial \vec{M}}{\partial t} = -\gamma \vec{M} \times \mu_0 \vec{H}_{eff} - \frac{\lambda}{M_s} [\vec{M} \times (\vec{M} \times \mu_0 \vec{H}_{eff})] , \quad (2.15)$$

In 1955 Gilbert proposed the damping term as [80]:

$$\frac{\alpha}{M_s} \left( \vec{M} \times \frac{\partial \vec{M}}{\partial t} \right) . \quad (2.16)$$

Then the Landau – Lifshitz – Gilbert equation (LLG) written as [80]:

$$\frac{\partial \vec{M}}{\partial t} = -\gamma \vec{M} \times \mu_0 \vec{H}_{eff} + \frac{\alpha}{M_s} \left( \vec{M} \times \frac{\partial \vec{M}}{\partial t} \right) , \quad (2.17)$$

where  $\alpha$  is the damping coefficient.

When considering the damping, the magnetization vector precesses with the Larmor angular velocity around the effective field towards the equilibrium in a spiral motion, as in Fig 2.1 (b).

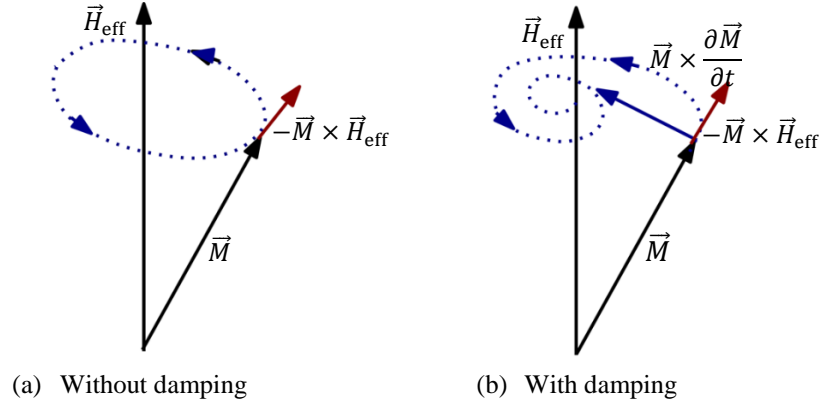


FIG 2.1 Dynamics of the magnetization vector. (a) The magnetization vector precesses in a circular motion around the  $\vec{H}_{eff}$  without damping. (b) The magnetization vector precesses in a spiral motion around the  $\vec{H}_{eff}$  with damping (adapted from [81]).

In 1987 Mallison [82] showed that the two historical approaches (LL and LLG equation) are equivalent to the mathematical term but not in physics terms. When large damping is considered, profound differences arise between the two forms. In the Landau-Lifshitz case, a physically implausible situation arises, whereas the Gilbert form's behavior with high damping remains in accord with common sense.

Which he described as:

- For small damping ( $\alpha \ll 1$ ), the two damping forms are equivalent. In case of the LLG equation, the system behaves as non-dissipative, and the magnetization trajectory stays circular.
- For ( $\alpha = 1$ ), the radial component of the dissipation energy term in the LLG equation has a maximum value and causes fast switching.
- For high damping ( $\alpha \gg 1$ ), dissipation energy becomes more apparent, and magnetization dynamics exhibit almost no precession and slow switching.

### 2.3 Magnetic Vortex

The magnetic vortex is formed due to the interaction between the exchange and dipolar energy. Within a specific length scale, the exchange and dipolar energy have the same value; below this length scale, the exchange interaction prevails, and parallel alignment of spins is preferred. At a larger length scale, the dipolar interaction prevails, and flux closure patterns are preferred. The high exchange energy at the center favors the parallel alignment of the magnetic moments, and the vortex core is formed. In contrast, the dipolar energy causes the circulation of the magnetization around the vortex core.

The magnetic vortex [83] structure has four possible independent states. The four vortex states are defined by the polarity of the vortex core, pointing either up ( $p = +1$ ) or down ( $p = -1$ ) and by the circulation of magnetization in the plane of disk, curling either clockwise ( $c = +1$ ) or counterclockwise ( $c = -1$ ) as shown in Fig 2.2. The combination of polarity and circulation defines the chirality (handedness) of a vortex, which can be either right-handed ( $cp = +1$ ) or left-handed ( $cp = -1$ ).

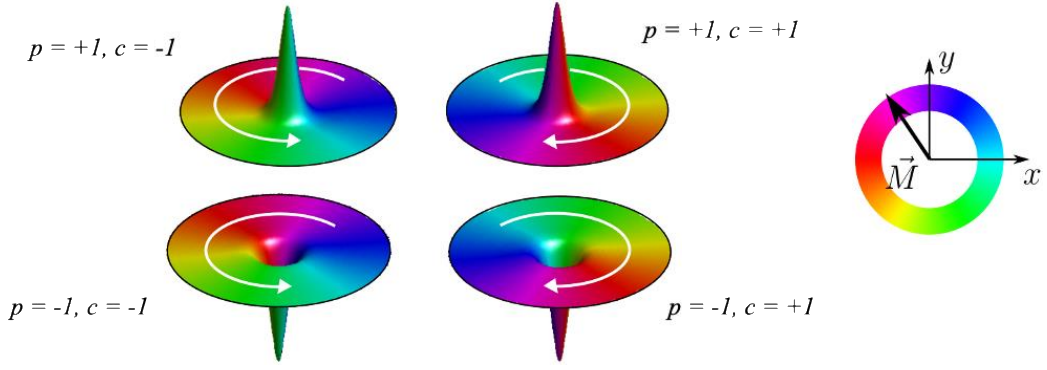


FIG 2.2 The four possible vortex configurations described with the combination of polarity  $p$  and circulation  $c$  (adapted from [84]).

If we consider a disk of the radius  $R$  and thickness  $L$  with the position polar coordinates  $C$  and  $\varphi$ . Then the thickness-dependent vortex core with the radius  $a$  is given as [85, 86]:

$$a = 0.68l_{ex} \left( \frac{L}{l_{ex}} \right)^{1/3}, \quad (2.18)$$

where  $l_{ex}$  is the exchange length.

Magnetization inside ( $C < a$ ) and outside ( $a < C < R$ ) the vortex core is given as [85]:

$$\text{For } C < a \quad \begin{cases} m_x = \frac{-2aC}{a^2 + C^2} \sin \varphi \\ m_y = \frac{-2aC}{a^2 + C^2} \cos \varphi \\ m_z = \sqrt{1 - \left( \frac{-2aC}{a^2 + C^2} \right)^2} \end{cases} \quad \text{For } a < C < R \quad \begin{cases} m_x = -\sin \varphi \\ m_y = \cos \varphi \\ m_z = 0 \end{cases} \quad (2.19)$$

### 2.3.1 Magnetization reversal of a vortex. Rigid vortex model

The magnetization reversal process is initiated by the shift of the vortex core with an applied field. Upon further increase of the field, the vortex annihilates as the core is expelled out of the disk. When the magnetic field decreases from some high saturated value, a new metastable vortex phase [87, 88] is formed at the nucleation field  $B_{nuc}$  and the moments are aligned in the shape of the letter “C”, which is typical in some disks. Sometimes the moment is also aligned in the shape of letter “S”, which is expected in bigger disks [89]. Upon further decreasing the magnetic field, this “C” phase leads to vortex nucleation, which quickly moves to equilibrium at the disk center [88, 90–92]. Correspondingly, we find an abrupt decrease in average magnetization.

The rigid vortex model describes the shift in the vortex core while preserving its shape in response to the external field as in Fig 2.3 and represents the susceptibility, magnetization distribution, and vortex annihilation field for low magnetic fields.



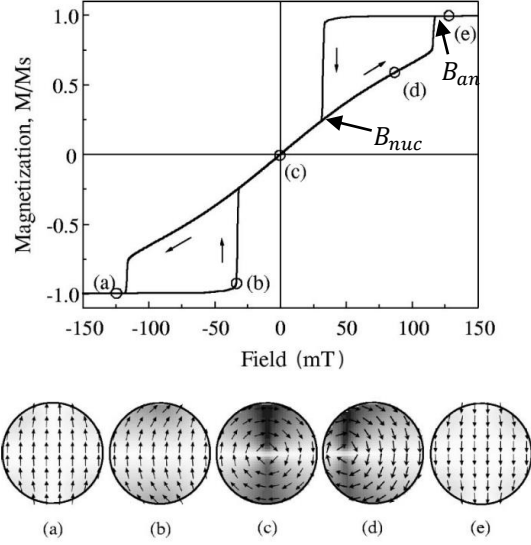


FIG 2.3 The typical hysteresis loop and magnetization reversal process due to the vortex nucleation, displacement, and annihilation, as calculated with a micromagnetic solver [93, 94].

Further, RVM gives the vortex core displacement  $s$  perpendicular to the applied field  $B$  using the initial magnetic susceptibility  $\chi(0)$ [95]:

$$s = \chi(0) \frac{BR}{\mu_0 M_s}. \quad (2.20)$$

Guslienko et al. calculated the initial susceptibility  $\chi(0)$  for  $L \ll R$

$$\chi(0) = \frac{2\pi}{\beta \left[ \ln\left(\frac{8}{\beta}\right) - \frac{1}{2} \right]}, \quad (2.21)$$

Here, the aspect ratio  $\beta = L/R$ . The initial susceptibility is a characteristic property that reflects the reversible vortex displacement in an applied field.

The average magnetization in the disk volume  $V$  in the direction of the applied field is given as:

$$(M)_V = \chi(0) \frac{B}{\mu_0}. \quad (2.22)$$

The vortex annihilation field can be calculated by considering the core displacement  $s = R$ ,

$$B_{an} = \frac{1}{\chi(0)} \mu_0 M_s. \quad (2.23)$$

A vortex formation depends on the disk geometry, such as thickness and radius. Magnetic disks with a radius less than the single domain [96] radius do not support vortex formation as the vortex state is unstable. In Fig 2.4, the in-plane single domain [97] state is shown in the region of a smaller radius and less thickness. The out-of-plane magnetization state is shown with a smaller radius and a comparatively higher thickness.

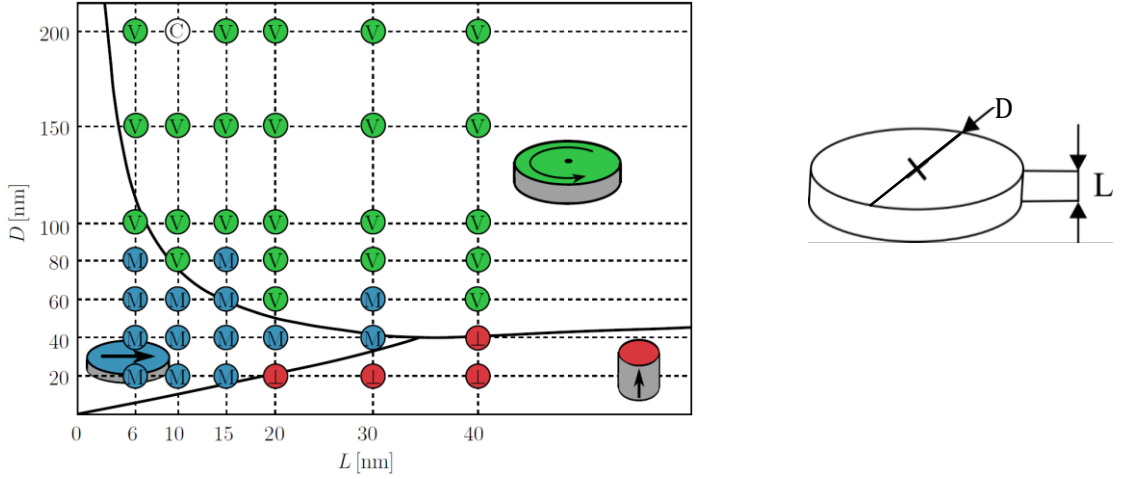


FIG 2.4 Phase diagram showing the stability of a magnetic vortex concerning the core displacement from its center simulated by OOMMF for circular nanodots with the diameter  $D$  and thickness  $L$ . Very small disks form monodomains, either in-plane (denoted M) or out-of-plane (denoted  $\perp$ ). The vortex states (denoted by V) occur for a suitable combination of thickness and radius. Metastable C-states are denoted by C [84, 98–100].

### 2.3.2 Vortex stability in the static magnetic field

#### (i) Effect of in-plane magnetic field on magnetic vortex

The magnetic field displaces the vortex core in the perpendicular direction of the applied field. So, when the in-plane magnetic field is applied to the disk, it will displace the vortex core away from the center towards the disk circumference, as in Fig 2.5(d). This will increase the magnetization along the field direction, as in Fig 2.5(e). Upon further increase in the magnetic field, the magnetization is aligned parallel to the field direction, and the vortex core disappears; this is called the annihilation field  $B_{an}$  [101–103]. The nucleation is a more complicated process. When the magnetic field is decreased from the fully saturated state, a new metastable phase forms at the nucleation field  $B_{nuc}$  and the magnetic moment is aligned in the shape of the letter “C”, which is typical in some disks as shown in Fig 2.5(a). Sometimes the moment is also aligned in the shape of the letter “S” or processed through the more complicated vortex pair state or buckling state, which is expected in bigger disks as in Fig 2.5(b). Upon further decrease of the magnetic field, this “C” state leads to the vortex core's nucleation, which quickly moves to the equilibrium position at the center of the disk. Usually, the nucleation field is defined as the field where the in-plane saturated state becomes unstable. In real disks, the vortex core's nucleation occurs, preferably at the defects, usually at the disk's side. So, from these, we can consider three magnetic states (the vortex state, C- state, and the saturated state) [85, 89, 93, 104, 105].

$$B_{nuc}(\beta, R) = 4\pi \left[ \vec{F}(\beta) - \frac{1}{\pi} \left( \frac{l_{ex}}{R} \right)^2 \right] \quad (2.24)$$

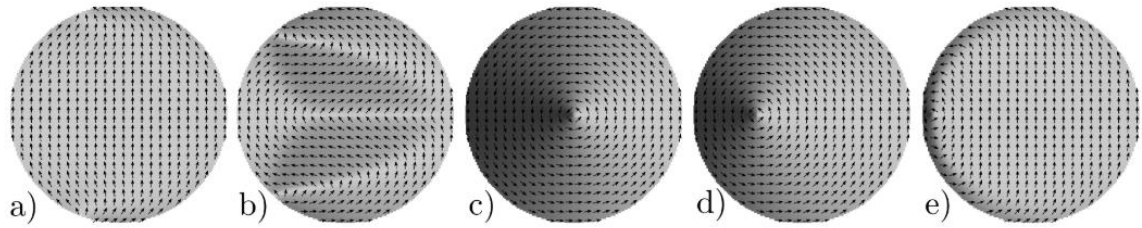


FIG 2.5 Micromagnetic simulation of a) C-state, b) S-state, c) vortex state at zero field, d) displaced vortex, and e) vortex state right before annihilation; calculated in Object Oriented Micromagnetic Framework (OOMMF) [89, 106].

The vortex-pair state consists of two vortex cores around which the magnetization is curling in the opposite sense (opposite circulations). Micromagnetic simulations show that the two cores of the vortex-pair state always have opposite polarities (giving the same handedness for both vortices of the pair) as in Fig 2.6(b). Upon the field decrease, the cores move towards each other, decreasing the net magnetization along the field direction until they annihilate, and a single vortex core is formed in the disk. As the polarity and circulation of the two competing vortices are opposite, the final vortex state will be random for symmetry reasons. However, this is difficult to realize in real samples because the geometrical symmetry can be broken due to lithographic imperfections and surface roughness of the substrate. In thin disks (e.g., 15 nm), the two vortex cores never unpin from the disk boundary before the vortex is nucleated. The in-plane magnetization forms the letter S, so this state is also called the S-state [93, 107].

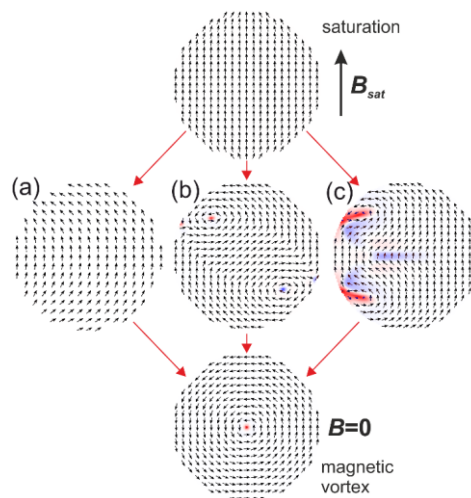


FIG 2.6 Magnetic vortex nucleates upon the field decrease from saturation proceeding through different nucleation states visualized by micromagnetic simulations: (a) nucleation through C states, (b) nucleation through the vortex-pair state, (c) and through buckling state. The blue-white-red color scale represents the perpendicular component of magnetization [89].

The buckling state is favored in large disks. The characteristic features of the buckling state are three Bloch domain walls with in-plane magnetization curling around them, as shown in Fig 2.6(c). When the applied field is decreased, the three-domain walls move towards each other until a vortex state is formed. The buckling state has a lower symmetry than the vortex-pair state. The in-plane magnetization shape indicates the final circulation of the vortex, as shown in Fig 2.6(c), and the circulation will become counterclockwise. Even though the situation is less evident for the final polarity state, the simulations

show that the  $m_z$  components at the disk edge will become dominant over those at the disk, and the vortex core polarity will be defined by the  $m_z$  component of the red domains.

(ii) *Effect of out-of-plane magnetic field on magnetic vortex*

When the out-of-plane magnetic field is applied to the disk, the magnetic moments lying in-plane at remanence are tilted out-of-plane in the field's direction.

The two things happen:

- 1) If the field is parallel to the core polarity, it will be considered a parallel state ( $p + 1$ ) or up polarity.
- 2) If the field is antiparallel to the core polarity, it will be described as an antiparallel state ( $p - 1$ ) or down polarity.

When the applied field is parallel to the core polarity, it is supporting the vortex core and widening the core. On the other hand, if the applied field is antiparallel to the core polarity, it reduces the core size.

When the applied out-of-plane field exceeds the saturation field  $\vec{H}_s \cong 4\pi M_s \hat{N}$ , then the magnetization is fully saturated out-of-plane.

### 2.3.3 Magnetic vortex dynamics

(i) *Gyration*

Gyration is the lowest frequency excitation mode of a magnetic vortex, which describes the precession of the vortex core around its equilibrium point with an applied field and describes by the dynamic equation of motion derived from Thiele's equation [108, 109] as:

$$\vec{G} \times \vec{C} - \hat{D}\vec{C} - \frac{\partial W(\vec{C})}{\partial \vec{C}} = 0, \quad (2.25)$$

where  $\vec{G}$  is the gyrovector,  $\vec{C}$  is the position of vortex core,  $\hat{D}$  is the damping constant, and  $W$  is the potential energy. The first term  $\vec{G} \times \vec{C}$  corresponds to the gyrotropic force. The coordinate systems are considered, such as the origin coincides with the disk center, and the  $z$ -axis is parallel to the disk symmetry axis. So, the gyrovector points in the  $\hat{z}$  direction ( $G = (0, 0, G_0)$ ) and the position of the vortex core as  $C = (x, y, 0)$ .

The second term  $\hat{D}\vec{C}$  indicate the damping force, and the damping constant is written as  $\hat{D} = \frac{G_0}{2} \ln\left(\frac{C}{a}\right)$ . After neglecting the second (damping) term from the above equation, we get the equation for the circular motion of the vortex core, which can be written as:

$$\vec{G} \times \vec{C} - \frac{\partial W(\vec{C})}{\partial \vec{C}} = 0, \quad (2.26)$$

here  $\vec{G} = -G_0 p \hat{z}$  and  $G_0 = -2\pi p L M_s \hat{z} / \gamma$  is the polarity ( $p$ ) dependent [110–113] gyrovector. The parameter  $p$  is the vortex core polarization,  $L$  is the disk thickness, and  $\gamma$  is the gyromagnetic ratio. The potential energy  $W$  is associated with a restoring force which helps to move the vortex core back to the center and defined by a parabolic function as:

$$W = \frac{1}{2} \kappa C^2, \quad (2.27)$$

where  $\kappa$  is the effective stiffness constant and can be further defined as:

$$\kappa = \kappa_m - \kappa_{ex} = \frac{\pi M_s^2 L^2}{4\mu_0 C} - \frac{2\pi AL}{C^2} \quad (2.28)$$

Here  $\kappa_m$  is stiffness constant of magnetostatic energy, and  $\kappa_{ex}$  is the exchange energy stiffness constant.

The various forces acting on the magnetic vortex core is shown in Fig 2.7(a). When the external magnetic field is applied to the magnetic disk, the vortex core is moved away from the disk center's original equilibrium position. The vortex core gyrates at a specific frequency around a new equilibrium point, defined by the applied field's amplitude. The gyrovector force compensates the restoring force, which forces the vortex core back to the equilibrium position. The damping force slows down the vortex core gyration. As a result, this makes the vortex core move towards the new equilibrium point in a spiral trajectory. Finally, when the field is turned off, the vortex core moves back to the disk center equilibrium position in a spiral motion. The gyration of the vortex core in a potential well is shown in Fig 2.7(b).

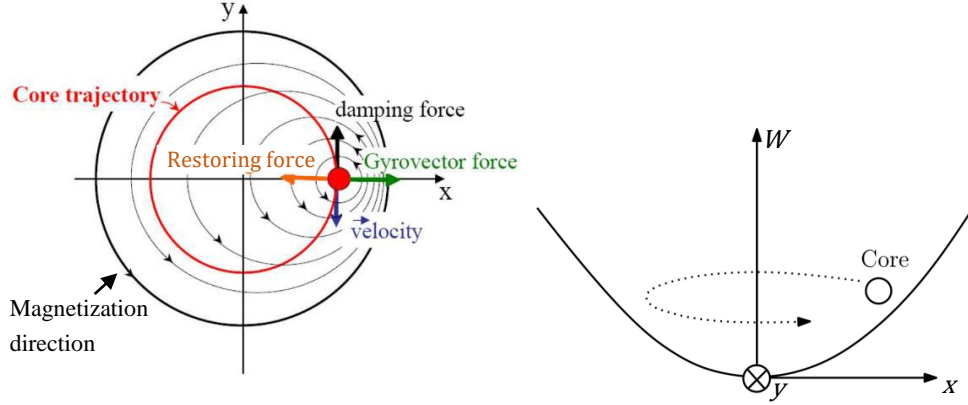


FIG 2.7 Sketch of the magnetic forces driving the gyrotropic mode in a disk (the core is represented by the red dot) [114, 115]. (b) The potential well with magnetostatic energy expanded to the second-order in vortex-core displacement [116]. The dashed arrows indicate the orbital motion of the vortex core.

The equation 2.26 can be solved as:

$$\vec{G} \times \vec{C} = \begin{bmatrix} \hat{x} & \hat{y} & \hat{z} \\ 0 & 0 & G_0 \\ \dot{x} & \dot{y} & 0 \end{bmatrix} = -\dot{y}G_0\hat{x} + G_0\dot{x}\hat{y}, \quad (2.29)$$

$$\text{and } \frac{\partial W}{\partial C} = \kappa C,$$

So, the homogenous set of the first-order differential equations can be written as [95]:

For  $x$ -axis

$$\begin{aligned} -\dot{y}G_0 - \kappa x &= 0, \\ \dot{y} + \frac{\kappa}{G_0}x &= 0. \end{aligned} \quad (2.30)$$

For  $y$ -axis

$$\begin{aligned} G_0\dot{x} - \kappa y &= 0, \\ \dot{x} - \frac{\kappa}{G_0}y &= 0. \end{aligned} \quad (2.31)$$

From this, we get a set of the second-order differential equations:

$$\ddot{x} + \left(\frac{\kappa}{G_0}\right)^2 x = 0, \quad \ddot{y} + \left(\frac{\kappa}{G_0}\right)^2 y = 0. \quad (2.32)$$

The solution of the above equations shows the harmonic oscillation with equal translational eigenfrequency  $\omega = \kappa/|G_0|$ .

If we consider susceptibility  $\chi$  and eigenfrequency  $\omega$  [117, 118] as independent of the position of the vortex core, the trajectory of the vortex core will be circular with the center at the disk center [119].

The polarity of the vortex core describes the sense of gyration of the vortex core, as shown in Fig 2.8. If the polarity is up, the sense of gyration of the vortex core is counterclockwise, while if the polarity is down, the sense of gyration is clockwise. If the force is pointing towards the left, it will give counterclockwise circulation, and if the force is pointing right, it describes clockwise circulation.

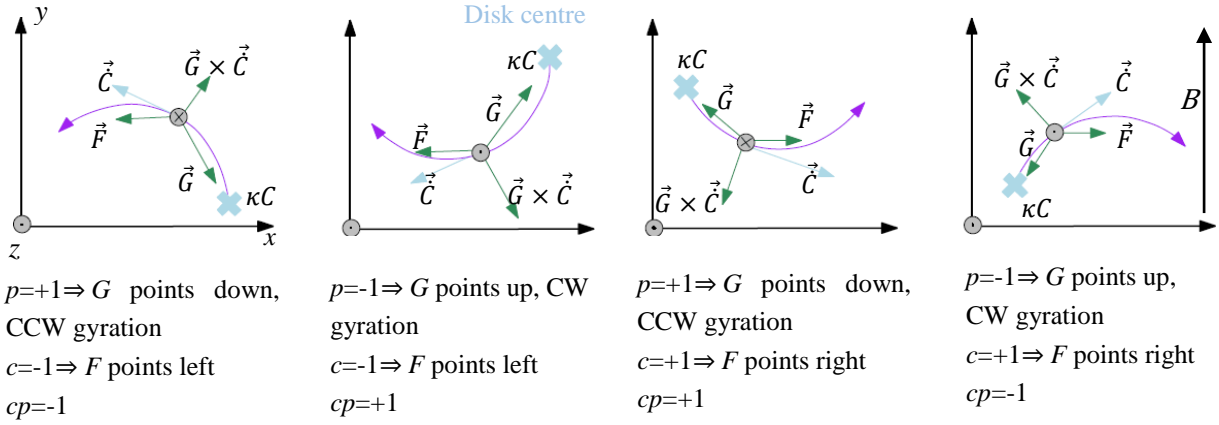


FIG. 2.8 Gyration of a vortex core for different vortex states.

### (ii) Pinning of magnetic vortices

The vortex dynamics is also affected by the pinning defects in the materials [120]. Pinning defects cause discontinuous vortex motion as a function of the applied magnetic field, which was firstly described by Uhlig et al. [121]. Further, when a vortex is pinned by a defect, gyrotropic frequency  $\omega_G$  increases significantly from the predicted value by the equation:

$$\omega_G = \pm \frac{\kappa \vec{G}}{2\pi(\vec{G}^2 + \vec{D}^2)} \quad (2.33)$$

Where the positive sign is for clockwise mode, and a negative sign is for counterclockwise mode, and the sign of  $\vec{G}$  is determined by the sign of core polarity  $p$ , and the phenomena were observed by Compton and Gowell [122]. Fig 2.9 shows a vortex core's motion in pinned orbit (with defect) and in unpinned orbit (without defect).

The fluctuation of  $\omega_G$  due to pinning suggests the existence of a depinning threshold for a given position of the vortex core. When  $\omega_G$  was measured as a function of pulse amplitude at different core positions,  $\omega_G$  showed transitions from high to low values with increasing amplitude.

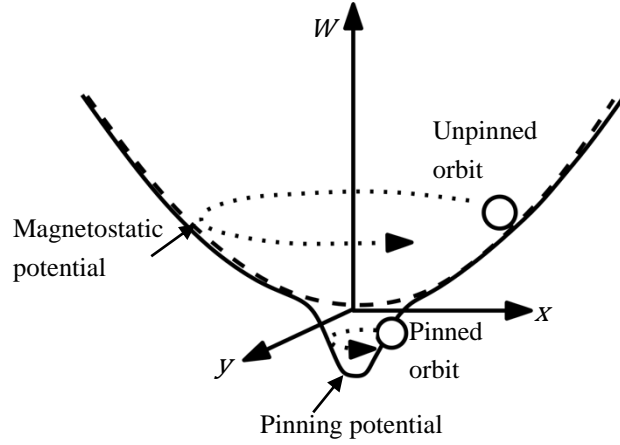


FIG 2.9 Schematic of the potential energy, including a parabolic magnetostatic potential (dashed curve) and a Gaussian pinning potential due to a point-like defect. The dotted arrows indicate the pinned and unpinned orbits of the vortex core [116].

A pinning defect induces a pinning potential [123–126], which locally confines the vortex core. At low excitation amplitude, the vortex core remains within the range of the pinning site; as the magnitude of excitation increases, the radius of the core's orbit about its equilibrium position also increases. When the radius of the core's orbit exceeds the range of the pinning potential, the core is depinned and  $\omega_G$  decreases [116].

(iii) *Vortex core trajectory induced by external stimuli*

We will derive the vortex dynamics in the circular disk under the application of the external static field  $H_{ext}$ , radio frequency (RF) spin-torque  $u$ , and the RF Oersted field  $he^{i\omega t}\hat{y}$ . For the calculation, we will start with the modified Thiele equation including the spin torque term [28], [127]

$$\vec{G}(p) \times (u - \vec{C}) = -\frac{\delta W}{\delta \vec{C}} - \alpha \widehat{D}\dot{\vec{C}} + \beta \widehat{D}u \quad (2.34)$$

where  $u$  is the spin torque interaction term of the current and the magnetization, which is further given as  $u = \frac{\mu_B p (-J e^{i\omega t})}{e M_s} \hat{x} = u_0 e^{i\omega t} \hat{x}$  and is proportional to the current density  $J$ , Bohr magneton  $\mu_B$ , and spin polarization  $p$  with electron charge  $e$ . Here, we assumed that the current is injected into the  $x$ -axis. The potential energy  $W$ , by the combination of Zeeman, magnetostatic, and exchange energy can be written as  $W(C) = \frac{1}{2} \kappa C^2 + q \cdot (\vec{H} \times \vec{C})$ , where  $q = c q_0 \hat{z} = \pi c M_s L C \hat{z}$ ,  $(\vec{H} \times \vec{C}) = (\vec{H}_x y - \vec{H}_y x)$ .

The magnetic field  $\vec{H}$  is given as  $\vec{H} = \vec{H}_{ext} + Re\{h_{ext} e^{i\omega t} \hat{y}\}$  and the external field  $\vec{H}_{ext} = (\vec{H}_x, \vec{H}_y)$  is applied in the disk plane, where  $h_{ext}$  is the amplitude of the RF-Oersted field generated by the RF current flowing through the disk and the electrodes.

The vortex core position can be written in the following form [127, 128] :

$$\vec{C} = \begin{pmatrix} x \\ y \end{pmatrix} = \begin{pmatrix} x_0 + Re\{X e^{i\omega t}\} \\ y_0 + Re\{Y e^{i\omega t}\} \end{pmatrix} \quad (2.35)$$

Here,  $x_0$  and  $y_0$  are the equilibrium positions of the vortex core in the external static magnetic field.  $X$  and  $Y$  are the complex oscillation amplitudes. By substituting eq (2.35) into equation (2.34), we get the following eq.:

$$\begin{aligned}
i\omega \begin{pmatrix} \alpha\tilde{D} & -G_0p \\ G_0p & \alpha\tilde{D} \end{pmatrix} \begin{pmatrix} X \\ Y \end{pmatrix} e^{i\omega t} + \kappa \begin{pmatrix} x_0 + Xe^{i\omega t} \\ y_0 + Ye^{i\omega t} \end{pmatrix} \\
= \begin{pmatrix} cq_0(H_y + h_{ext}e^{i\omega t}) + \beta\tilde{D}u_0e^{i\omega t} \\ G_0pu_0e^{i\omega t} - cq_0H_x \end{pmatrix}
\end{aligned} \quad (2.36)$$

For the zero RF current,  $J = 0$ , all the terms concerned with the oscillation that corresponds to the RF spin-torque  $u$ , RF-Oersted field  $h_{ext}$ , and the oscillation amplitude  $X$  are removed. Therefore, after putting  $J = u_0 = h_{ext} = X = Y = 0$  in eq. (2.36), we get the equilibrium position as:

$$\begin{pmatrix} x_0 \\ y_0 \end{pmatrix} = \frac{cq_0}{\kappa} \begin{pmatrix} H_y \\ -H_x \end{pmatrix} \quad (2.37)$$

By substituting Eq. (2.37) into eq. (2.36), we will get the new equation describing vortex dynamics:

$$\begin{pmatrix} \kappa + i\omega\alpha\tilde{D} & -i\omega G_0p \\ i\omega G_0p & \kappa + i\omega\alpha\tilde{D} \end{pmatrix} \begin{pmatrix} X \\ Y \end{pmatrix} = \begin{pmatrix} cq_0h_{ext} + \beta\tilde{D}u_0 \\ G_0pu_0 \end{pmatrix} \quad (2.38)$$

By the vortex dynamics eq., we obtain the oscillation amplitude of the vortex core as,

$$\begin{pmatrix} X \\ Y \end{pmatrix} = \begin{pmatrix} X' + iX'' \\ p(Y' + iY'') \end{pmatrix} \quad (2.39)$$

Where,

$$\begin{aligned}
X'(\omega) &= u_0 \frac{\tilde{\beta}\tilde{\kappa}(\omega_\gamma^2 - \omega^2) + (1 + \tilde{\alpha}\tilde{\beta})\alpha_*\omega^2}{(1 + \tilde{\alpha}^2)\{(\omega_\gamma^2 - \omega^2)^2 + (\alpha_*\omega)^2\}} + h_{ext} \frac{c\tilde{q}_0\{\tilde{\kappa}(\omega_\gamma^2 - \omega^2) + \alpha_*\tilde{\alpha}\omega^2\}}{(1 + \tilde{\alpha}^2)\{(\omega_\gamma^2 - \omega^2)^2 + (\alpha_*\omega)^2\}} \\
X''(\omega) &= u_0\omega \frac{-\tilde{\beta}\tilde{\kappa}\alpha_* + (1 + \tilde{\alpha}\tilde{\beta})(\omega_\gamma^2 - \omega^2)}{(1 + \tilde{\alpha}^2)\{(\omega_\gamma^2 - \omega^2)^2 + (\alpha_*\omega)^2\}} + h_{ext}\omega \frac{c\tilde{q}_0\{-\tilde{\kappa}\alpha_* + \tilde{\alpha}(\omega_\gamma^2 - \omega^2)\}}{(1 + \tilde{\alpha}^2)\{(\omega_\gamma^2 - \omega^2)^2 + (\alpha_*\omega)^2\}} \\
Y'(\omega) &= u_0 \frac{\tilde{\kappa}(\omega_\gamma^2 - \omega^2) + (\tilde{\alpha} - \tilde{\beta})\alpha_*\omega^2}{(1 + \tilde{\alpha}^2)\{(\omega_\gamma^2 - \omega^2)^2 + (\alpha_*\omega)^2\}} - h_{ext} \frac{c\tilde{q}_0\alpha_*\omega^2}{(1 + \tilde{\alpha}^2)\{(\omega_\gamma^2 - \omega^2)^2 + (\alpha_*\omega)^2\}} \\
Y''(\omega) &= u_0\omega \frac{-\tilde{\kappa}\alpha_* + (\tilde{\alpha} - \tilde{\beta})(\omega_\gamma^2 - \omega^2)}{(1 + \tilde{\alpha}^2)\{(\omega_\gamma^2 - \omega^2)^2 + (\alpha_*\omega)^2\}} - h_{ext}\omega \frac{c\tilde{q}_0(\omega_\gamma^2 - \omega^2)}{(1 + \tilde{\alpha}^2)\{(\omega_\gamma^2 - \omega^2)^2 + (\alpha_*\omega)^2\}}
\end{aligned} \quad (2.40)$$

Here,  $X'$  ( $X''$ ) and  $Y'$  ( $Y''$ ) are the x and y component of the real part (imaginary part) of the oscillation amplitude of the vortex core position, respectively. To simplify the notation, we introduce a few reduced parameters:

$$\begin{aligned}
\tilde{\alpha} &= \alpha \frac{\tilde{D}}{G_0}, & \tilde{\beta} &= \beta \frac{\tilde{D}}{G_0}, & \tilde{\kappa} &= \frac{\kappa}{G_0}, \\
\tilde{q}_0 &= \frac{q_0}{G_0}, & \alpha_* &= \frac{2\tilde{\alpha}\tilde{\kappa}}{1 + \tilde{\alpha}^2}, & \omega_\gamma &= \frac{\tilde{\kappa}}{\sqrt{1 + \tilde{\alpha}^2}}
\end{aligned} \quad (2.41)$$

Finally, the vortex core position is described by Eqs. (2.35), (2.37), (2.39) and (2.40).

#### (iv) Resonance splitting

A radio frequency (rf) field  $H_{rf}$  is applied to the disks to explore the frequency and amplitude-dependent dynamics of magnetic vortices [129]. As the magnitude of rf field increases, the resonance peak corresponding to the vortex translational mode splits into two different peaks, where separation increases with rf field. This resonance splitting is unusual in a single magnetic vortex, as this is a nondegenerate mode. However, the simulations do not show any indication that the high field response should differ with the low field [130–132]. In Fig 2.10(a) at low rf field, a single symmetric peak is visible. As the rf field is increased, the peak gets broadens and starts splitting, where one peak increases



in frequency and other decreases. Fig 2.10(b) shows the resonance splitting with the increase of rf current amplitude.

The increase in resonance frequency with the magnetic field is related to the increasing curvature of the energy profile [133]. The critical  $h_{rf}$  and splitting magnitude are relatively insensitive to external field  $H$ . However, the frequencies below the critical  $h_{rf}$ , vary little for small  $H$  but take a negative slope for larger  $H$ , which may be related to the asymmetry of the energy profile of shifted vortex [133]. For disks, the splitting effects were detected at even smaller  $h_{rf}$ . The vortex translational mode splitting or fold-over effect [134] was thus observed at large  $h_{rf}$  (nonlinear regime).

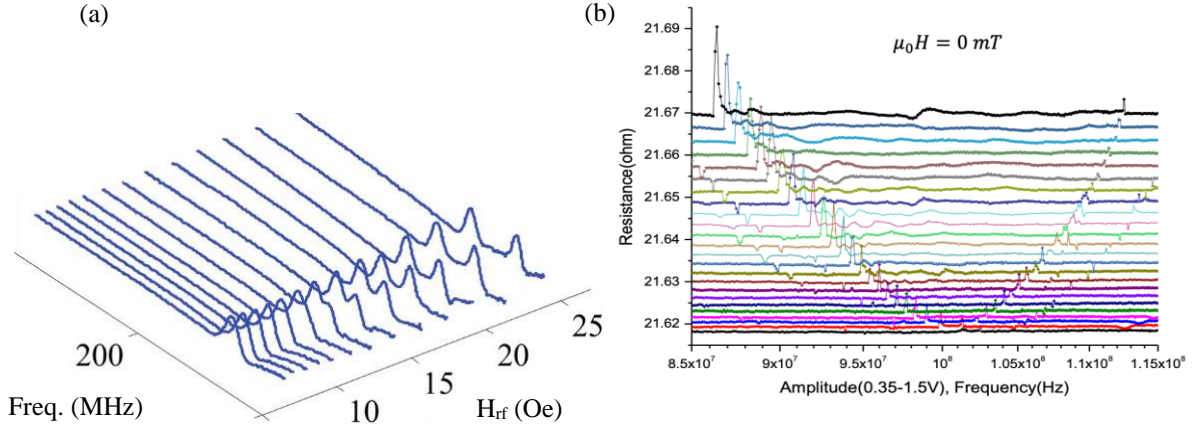


FIG 2.10 (a) Microwave spectra for an ellipse minor axis,  $H= 60$  Oe as a function of rf field  $h_{rf}$  [116, 130] (b) Experimentally observed the resonance splitting at high rf amplitude at zero field of a 4  $\mu\text{m}$  circular disk with symmetric placed electrodes.

G.de Loubens et al. [135] also showed the bistability of vortex core dynamics in a single magnetic disk subjected to a perpendicular bias magnetic field that varied in a wide range from positive to negative values. In a specific range of bias field magnitude, there are two stable gyrotropic modes of vortex core rotation having different frequencies and opposite polarity, which corresponds to the opposite orientation of vortex core relative to the direction of bias magnetic field. The difference in frequencies of these two stable gyrotropic modes is proportional to the magnitude of the applied bias field  $H$  and also to the dot aspect ratio  $\beta$ .

#### (v) *Dynamic vortex annihilation*

We have described gyration as the solution of Thiele's equation without considering the external magnetic force. Now we will define the solution with time-dependent general external force  $\vec{F}(t)$ , and consequently, by assuming a magnetic field pulse with a linear rise time [20], [95]. The equation of motion of the vortex core assumed to moves as a rigid object can be written as:

$$\vec{G} \times \vec{C} - \widehat{D}\dot{\vec{C}} - \frac{\partial w(\vec{C})}{\partial \vec{C}} = \vec{F}(t). \quad (2.42)$$

After neglecting the second (damping) term from the above equation, we get

$$\vec{G} \times \vec{C} - \frac{\partial w(\vec{C})}{\partial \vec{C}} = \vec{F}(t), \quad (2.43)$$

where  $\vec{F}(t) = -\frac{2}{3}\pi cLRM_s[\vec{B}(t) \times \hat{z}]$  is the time-dependent excitation force. The parameter  $c$  is the circulation, and  $R$  is the radius of the disk. In the beginning, we consider the vortex core at the center of the disk with zero velocity, such as:

$$x(0) = y(0) = \dot{x}(0) = \dot{y}(0) = 0.$$

The direction of the external force for the applied in-plane magnetic field  $B = (0, B, 0)$  parallel with the  $x$ -axis will be  $\vec{F}(t) = [F(t), 0, 0]$ . Now the first-order differential equations can be written as:

$$\dot{y} + \omega x = \frac{\vec{F}(t)}{G}, \quad \dot{x} - \omega y = 0. \quad (2.44)$$

By solving these equations for a constant external force, we get a circular vortex core trajectory with the vortex core center at  $S = (s, 0, 0)$  and the radius  $s = \frac{R\chi B}{\mu_0 M_s}$ , where  $F_0 = \kappa s$ .

If we consider a time interval  $(0; t_{rise})$  and a linear increase in the magnetic field from zero to a maximum value  $B_{max}$ . Then the velocity along the  $x$ -axis at an instantaneous position  $S$  is given as:

$$v_s = \frac{s_{max}}{t_{rise}}, \quad (2.45)$$

$$\text{where } s_{max} = \frac{R\chi B_{max}}{\mu_0 M_s} \quad \text{at } t_{rise} \leq \frac{2\pi}{\omega}. \quad (2.46)$$

If we take,  $\vec{F}(t) = \kappa v_s t$  then

$$\ddot{x} + \omega^2 x = \omega^2 v_s t, \quad \ddot{y} + \omega^2 y = \omega v_s. \quad (2.47)$$

Now the solution concerning the initial conditions is given as:

$$x(t) = v_s \left( t - \frac{1}{\omega} \sin \omega t \right), \quad y(t) = \frac{v_s}{\omega} (1 - \cos \omega t). \quad (2.48)$$

These equations describe the cycloidal trajectory of the vortex core, as shown in Fig 2.11(c). The component of vortex core velocity is the following:

$$\dot{x}(t) = v_s(1 - \cos \omega t), \quad \dot{y}(t) = v_s \sin \omega t. \quad (2.49)$$

By using eq. (2.45) and (2.46), the magnitude of vortex core velocity can be described as:

$$v(t) = 2v_s \sin\left(\frac{\omega t}{2}\right) = \frac{2R\chi}{\mu_0 M_s} \frac{B_{max}}{t_{rise}} \sin\left(\frac{\omega t}{2}\right). \quad (2.50)$$

The vortex core moves with the fastest speed in the cycloidal trajectory with a velocity of

$$v_{max} = 2v_s = \frac{2R\chi}{\mu_0 M_s} \frac{B_{max}}{t_{rise}}. \quad (2.51)$$

At time  $t > t_{rise}$ , if we consider the external magnetic field as  $B_{max}$  and the vortex core center  $S_{max} = (s_{max}, 0, 0)$  we get a circular trajectory of the vortex core with the radius  $|C(t_{rise}) - S_{max}|$  as shown in Fig 2.11(c) and the core velocity with a constant magnitude of

$$v(t_{rise}) = \frac{2s_{max}}{t_{rise}} \sin\left(\frac{\omega t_{rise}}{2}\right). \quad (2.52)$$

The maximum distance of the vortex core in  $x$ -axis can be written as:

$$x_{max} = s_{max} + |C(t_{rise}) - S_{max}| = s_{max} + \frac{2s_{max}}{\omega t_{rise}} \sin\left(\frac{\omega t_{rise}}{2}\right). \quad (2.53)$$

### Conditions for efficient dynamic vortex annihilation

The first condition for the dynamic annihilation can be described from the disk geometry. When the vortex core moves along its trajectory, it has to reach some minimum distance  $R_{an}$  from the disk center. This minimum distance is called the annihilation radius  $R_{an}$ , which is about 15% smaller than the disk radius  $R$  [45, 95, 136]. So, the condition is:

$$x_{max} \geq R_{an} \quad (2.54)$$

Second, to avoid the vortex polarity switching (see Section 2.3.4), the maximum core velocity  $v_{max}$  must not exceed the critical velocity  $v_{crit}$

$$v_{max} < v_{crit} \quad (2.55)$$

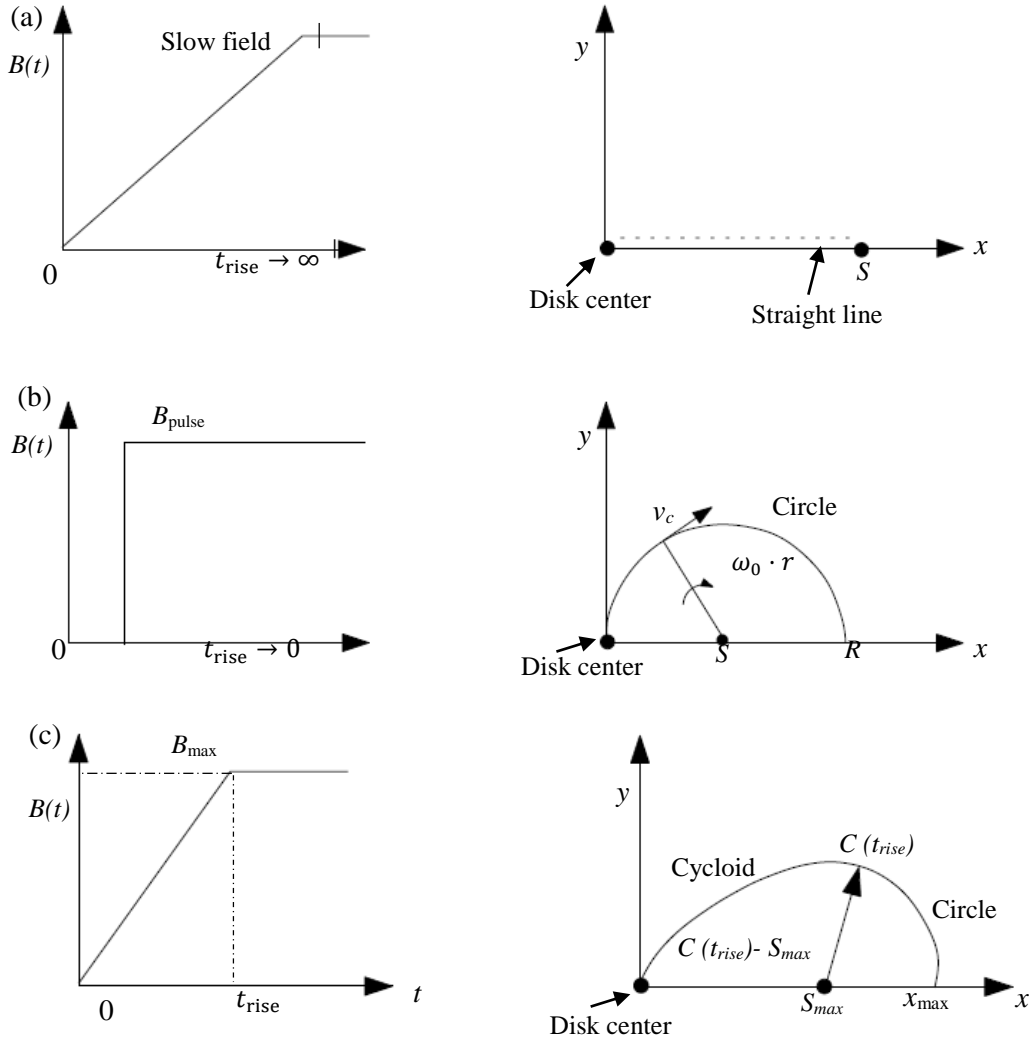


FIG 2.11 (a). With the infinite rise time, the vortex core moves in a straight path. (b) With  $t > t_{rise}$ , the trajectory of the vortex core is circular. (c) Linear increase of the magnetic field to  $B_{max}$  during the time interval  $(0, t_{rise})$  and constant magnetic field for  $t > t_{rise}$ . The trajectory of the vortex core is cycloidal in the interval  $(0, t_{rise})$  and circular for  $t > t_{rise}$ . [95].

### 2.3.4 Vortex polarity Switching

#### (i) Mechanism of core reversal

When the excitation field is applied, the vortex core starts gyrating around its equilibrium point. The distortion of the current out-of-plane vortex structure starts occurring. Simultaneously, a magnetic dip starts appearing at the inner part of the core trajectory, on the opposite side of out-of-plane magnetization. The out-of-plane component starts increasing with the time and reaches a full out-of-plane orientation in the opposite direction. When the vortex core reaches its critical velocity [137], the magnetic dip splits, and the vortex-antivortex pair is created. The newly formed vortex-antivortex moves apart, and the antivortex annihilates with the original vortex. After that, only one vortex remains in the structure with opposite polarization [44, 138–145], as shown in Fig 2.12.

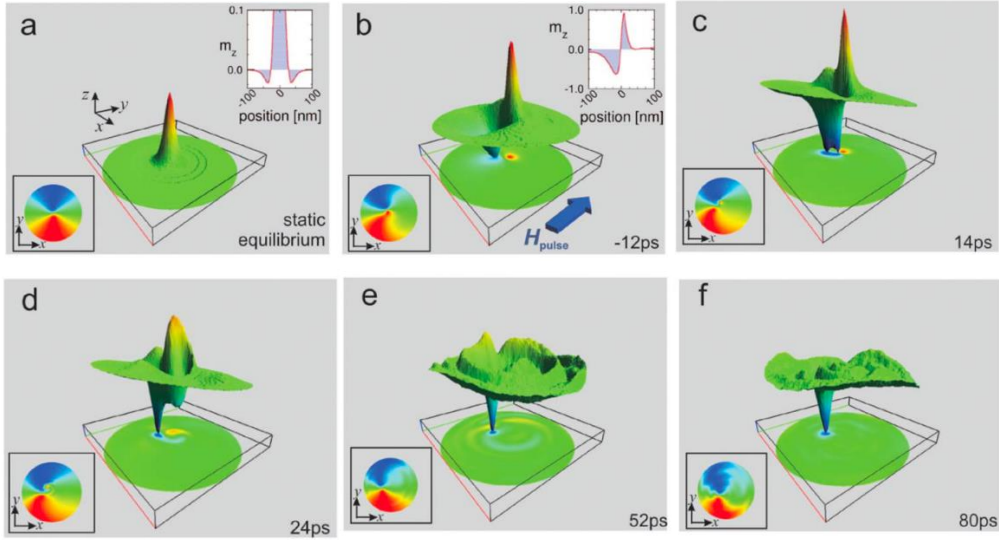


FIG 2.12 Topography of  $m_z$  during the core switching process. (a) Static equilibrium. The cutline on the upper right shows the small negative dip in  $m_z$  near the core. (b) Formation of a large negative dip of  $m_z$  by the gyrofield. The cutline goes along the diameter through the vortex core and the adjacent dip. (c) Pair creation leads to two separate points with  $m_z = -1$ . (d) The original vortex core annihilates with the new antivortex. (e) Spin waves are emitted after the annihilation. Finally, a vortex core with opposite polarization remains. (f) The insets on the lower left show the  $x$  component of the magnetization (red:  $m_x = 1$ , blue:  $m_x = -1$ ). The times are relative to the pulse maximum [139].

This vortex core switching is induced by the gyrofield originating from the dynamic deformation of magnetization around the vortex core. This deformation further leads to the vortex core instability and the vortex core switching by the nucleation and annihilation of the vortex-antivortex pair. The main contribution to the gyrofield is short-range exchange interaction, and the relation between the critical velocity and exchange interaction is written as:

$$v_{cri} \cong 1.66\gamma\sqrt{A}$$

where  $v_{cri}$  is the critical velocity, and  $A$  is the exchange interaction. The critical velocity for Permalloy is  $\sim 320$  m/s. The switching of vortex core polarity at the critical velocity is shown in Fig 2.13(b), while Fig 2.13(a) shows the gyration of a displaced vortex core at zero external field.

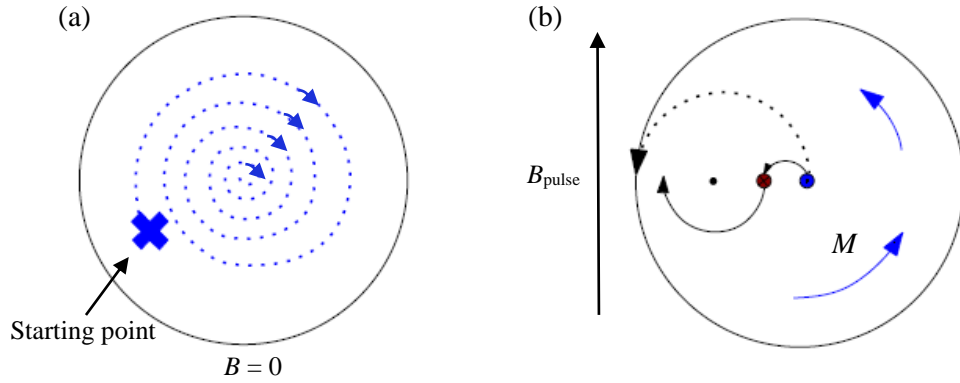


FIG 2.13 (a) Gyration of the vortex core in zero external magnetic field. The core was initially displaced by the external magnetic field  $B_{ext}$  and gyrates around the disk center in the spiral motion (caused by damping). (b) The vortex core annihilation for optimal magnetic field pulse parameters (black dotted line). In case that the critical velocity is exceeded, the core polarity switching prevents the core annihilation.

(ii) *Switching of the vortex core*

The phenomena of the switching of vortex core polarity were first shown by T. Okuno et al. in 2002 [146] by micromagnetic simulation and A. Thiaville et al. in 2003 [147]. They showed the switching of vortex core polarity by the static magnetic field, perpendicular to the vortex plane. The magnetic field strength of the order of 500 mT was required to crush the original vortex core polarity and to establish the opposite vortex core polarity. This high value of field strength is needed to overcome the high energy barrier of a vortex core.

In 2006, B. Van Weayenberge [44] experimentally demonstrated the vortex core switching by a low amplitude in-plane magnetic field driving the core above its critical velocity. An in-plane sinusoidal magnetic field was applied to the magnetic structure, resulting in the gyrotropic movement of the vortex core around its equilibrium vortex core position. The gyrotropic frequency depends on the vortex structure and typically in the order of 100 MHz to 1 GHz. [139, 148, 149].

In 2006, Kasai et al. also demonstrated that the magnetic vortex core could be resonantly excited by an ac current through a ferromagnetic circular dot where the current frequency is tuned to the eigenfrequency, originating from the confinement of vortex core in the dot [150]. However, in 2007, Yamada et al. discovered that the higher excitation current induces even the switching of the core magnetization during the circular motion. This can be described that the spin current can apply a torque on the magnetic moment when the spin direction of the conduction electrons has a relative angle to the local magnetic moment. This leads to the hypothesis that any type of spin structure with spatial variation can be excited by spin-polarized current in a ferromagnet. When the ac current is applied, the vortex core first moves in the direction of spin current; this originates the spin-transfer effect. The off-centered core is then forced back towards the center by the restoring force, and because of the gyrotropic nature of the vortex core, it starts the circular motion around the dot center. This precessional motion is then amplified by the current to reach a steady orbital motion, where the spin transfer from the current is balanced with the damping. The direction of precessional motion depends on core magnetization [1, 140, 151–159].

In 2009, Weigand et al. showed the vortex core switching by the in-plane magnetic field pulse [48] and further explored by other groups [153–156].

Kammerer et al. in 2011 and 2012 experimentally demonstrate the switching of magnetic vortex core by spin-wave excitation with in-plane rotating GHz magnetic field [51, 54].

### 2.3.5 Vortex Circulation switching

The direction of the in-plane magnetization circulation is independent of the vortex core's gyration and, hence, the vortex core polarity.

#### (i) Mechanism of circulation switching

Circulation is the rotational direction of in-plane magnetic moment whirling either clockwise (CW) or counterclockwise (CCW). The circulation reversal proceeds through the nucleation, displacement, and annihilation of the vortex [164]. When the magnetic field is applied, the vortex core is displaced from its center, perpendicular to the applied magnetic field, and the displacement value depends on the strength of the magnetic field. Upon further increase of the magnetic field, the magnetic moment is aligned all in one direction, and the vortex core is expelled out of the disk; this happens at the annihilation field  $B_{an}$ . The process of circulation switching is already explained in section 2.5.

While the sense of magnetization circulation that form as the field is removed can be controlled, either by exploiting asymmetry in the structure shape [43, 45, 95, 165] or the spectral distribution of the applied magnetic field [166]. While in a perfectly circular disk, the probability of the formation of CW and CCW distribution is equal.

#### (ii) Switching of vortex circulation

In 2001, Schneider et al. used the shape asymmetry (D shape disk) for selective circulation switching. In the disk, with the flat edge on one side of the disk, the vortex can easily nucleate through the flat edge assisted by the larger demagnetizing field than that at the round edge [43] shown in Fig 2.14.

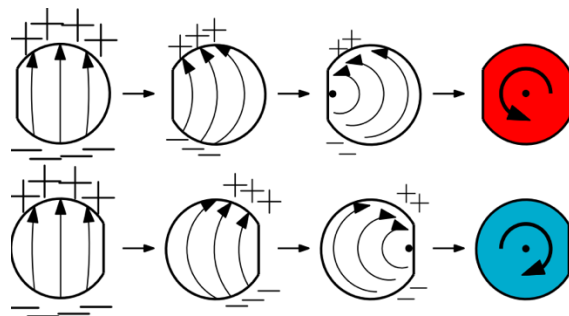


FIG 2.14 Schematics of the nucleation process of a vortex state in an asymmetric disk. The magnetic field decreases from left to right. While reducing the field, magnetization goes from saturation to a C-state. For the magnetic field in the vertical direction, the C-state is formed either on the left or the right side of the disk – the side is defined by the asymmetry position for a tapered disk. After reaching the nucleation field  $B_{nuc}$ , a vortex core appears on the asymmetry. The final vortex state is formed when the field is completely turned off [106].

In 2013, Uhlir et al. demonstrated the selective switching of circulation by thickness modulation (tapered disk). They used a fast-rising in-plane magnetic field pulse that drives the vortex core into a gyrotropic precession and annihilates the vortex during the first half period of precessional motion at the disk boundary. The resulting circulation of a new vortex was controlled by a disk asymmetry in the form of a thickness gradient and the direction of the magnetic field pulse. This approach allows for fast switching, with the field amplitude reduced by more than 50% compared to the switching using a static field. [45, 95, 136].

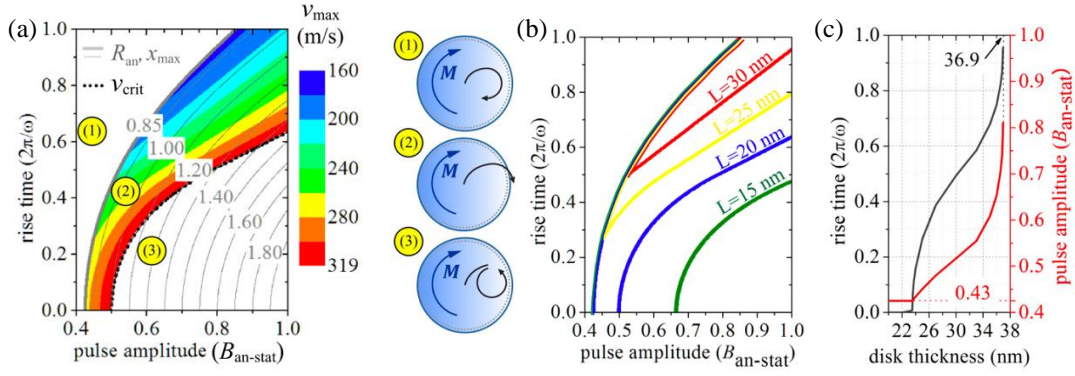


FIG. 2.15 (a) Shows the region of successful vortex core annihilation [color coded, marked as (2)]. Two boundaries define the region: the thick gray line at  $x_{max} = 0.85R$  for the annihilation radius and the black dotted line at  $v_{max} = 320$  m/s for the critical velocity  $v_{crit}$ . In region (1), above the annihilation radius boundary, the maximum amplitude of the translational motion of the vortex core is too low, and the core gyrates inside the disk. In region (3), below the critical velocity boundary, the core switches its polarity and reverses its sense of gyration. (b) Phase diagram showing the regions of successful vortex core annihilation in permalloy disks with different thicknesses. The lowest amplitude boundary on the left remains the same for all thicknesses. The critical velocity boundary moves to the top left with increasing disk thickness, which means the region of successful vortex core annihilation is progressively shrinking. (c) Thickness dependence of the minimum pulse amplitude (red line) and the corresponding minimum pulse rise time (black line) needed for successful vortex core annihilation [95].

The controlled switching of circulation [167] was also studied by applying an asymmetric field to the magnetic structure. The asymmetric field was enough to break the symmetry of circulation direction during the nucleation process [168–171]. The dynamic switching was also simulated by a uniform field pulse [172].

All the above papers describe theoretically or experimentally, individual control of polarity and circulation, but no-one describes the selective switching of a particular vortex state. Then in 2014, G. Shimon et al. [53] experimentally demonstrated the independent control of polarity and circulation. They used the perpendicular magnetic anisotropy (PMA) layer for the control of the vortex core polarity. The PMA layer  $[Co/Pd]_n$  was used along with the NiFe layer on the top, and the two layers were separated by the Ti spacer. The purpose of the PMA layer was to stabilize the vortex core polarity in the top NiFe free layer against the external field and also against the thermal disturbance after a particular vortex state is set. At the same time, the circulation was controlled by introducing thickness modulation in the NiFe layer for an additional shape anisotropy. They used the magnetic force microscopy (MFM) method for the detection of the vortex states.

## 2.4 Electrical transport measurements of vortex dynamics

### 2.4.1 Magnetoresistance

Magnetoresistance is defined as a change of resistance of a material under an applied magnetic field.

$$\text{magnetoresistance} = \frac{R - R_{\text{sat}}}{R_{\text{sat}}} \cdot 100\% \quad (2.56)$$

The electrical resistance in a conducting material arises due to the processes of scattering (collision) of electrons such as electron-phonon scattering, electron-electron scattering, electron-impurity scattering. Strong scattering processes produce a short mean free path and a large resistance, whereas weak scattering processes produce long mean free paths and lower resistance. The change in the scattering



amplitude can change the resistance. When this change is obtained using a magnetic field, the phenomena is called magnetoresistance [173]. The spin degree of freedom of electrons may also contribute to such a scattering process, affecting the resistance of materials. In magnetic materials, the spin-dependent effect is large, which strongly affects the conduction processes, and finally, the resistance of the materials. The scattering, due to interaction between the spin of conduction electrons and the spin of localized electrons, has a significant contribution in the conduction process. In magnetic materials, the spin directions of electrons can be controlled using magnetic fields. Thus, the scattering amplitude related to spin-dependent scattering can be changed, which may result in a significant change of resistance on the application of the magnetic field.

Here we list some of the important magnetoresistance types:

- Anisotropic magnetoresistance (AMR): It is the change of resistance when the electric current is perpendicular or parallel to the internal magnetization [174, 175]. This effect was first discovered by William Thomson in 1856.
- Giant magnetoresistance (GMR): This is an extrinsic effect and connected to the external field. In GMR, the two magnetic layers are separated by a nonmagnetic metallic spacer, and it also depends on the angle between the two magnetizations [176].
- Tunnel magnetoresistance (TMR): In TMR, two magnetic layers are separated by a nonmagnetic insulating spacer. This effect is based on the spin-dependent tunneling [177, 178].

#### 2.4.2 Calculation of spin-transfer torque and RF Oersted field

When the current flows through a ferromagnet, it becomes spin-polarized and carries angular momentum. The current remains polarized in the neighboring nonmagnetic layers so that the angular momentum carried by the current can interact with the magnetization in the subsequent magnetic layers. The spin current exerts a spin-transfer torque [157, 179–185] on the magnetization in the device. For a large amount of current, this torque leads to precession and reversal. The first work on the spin-transfer torque comes in the 1970s and 1980s, with Berger’s prediction that spin-transfer torque should be able to move the magnetic domain walls [186, 187].

Most devices have small cross-sectional areas for two reasons. First, usually high current densities are required to transfer enough angular momentum to affect the magnetization. The heat generated by the current would destroy the device itself if it were not concentrated in a small area with good thermal contact to a large mass. Second, the relative effect of the Oersted field as compared to the direct spin-transfer decreases as the cross-sectional area decreases. For a uniform current density and uniform magnetization, the spin-transfer torque is uniform. The spin-transfer torque then couples strongly to the uniform precession mode. The torque per area is independent of the area for constant current density. The Oersted field, on the other hand, is non-uniform and does not couple to the uniform precession of a uniform magnetization. As the cross-sectional area decreases, the magnetization tends to become more uniform, and it becomes harder to excite non-uniform modes. Also, besides the maximum Oersted field decreases as the area decreases for a constant current density. In a small disk, the contribution of the Oersted field is small, whereas, in a larger micron size disk, the Oersted field dominates.

When the alternating current is injected into the ferromagnetic disk, it excites the gyrotropic motion of the vortex core, which leads to oscillation in resistance [123, 128, 152, 188–192]; it can be further mixed



with input rf current to generate a measurable rectified dc voltage [134, 167, 193–195]. These rectifying spectra can precisely detect vortex dynamics. Below we calculate the rectifying voltage [128, 193, 196–200].

(i) *Rectifying voltage*

The electrical resistance arising from the AMR effect in permalloy disk depends on the vortex core position. When the direction of the electrical current is parallel to the magnetization, the magnetoresistance increases, whereas the magnetoresistance decreases when the current direction is perpendicular to the magnetization. When the position of the core  $C = (x, y)$  is shifted from the center of the disk  $(x_R, y_R)$ , the disk resistance is expressed as [128, 193, 194]:

$$R = R_0 - a_x(x - x_R)^2 + a_y(y - y_R)^2 \quad (2.57)$$

Here,  $x$  and  $y$  are the vortex core position,  $x_R$  and  $y_R$  are the centers of electrode gap, and  $a_x, a_y$  are proportionality constant.  $R_0$  is the resistance for  $x=x_R, y=y_R$ . After substituting eq (2.32) in eq. (2.57),

$$\begin{aligned} R(t) = & R_0 - a_x\{(x_0 - x_R)^2 + X'^2 \cos^2 \omega t + X^2 \sin^2 \omega t + 2(x_0 - x_R)X' \cos \omega t - \\ & 2X'X'' \cos \omega t \sin \omega t - 2(x_0 - x_R)X'' \sin \omega t\} + a_y\{(y_0 - y_R)^2 + Y'^2 \cos^2 \omega t + Y''^2 \sin^2 \omega t + \\ & 2P(y_0 - y_R)Y' \cos \omega t - 2Y'Y'' \cos \omega t \sin \omega t - 2P(y_0 - y_R)Y' \sin \omega t\} \end{aligned} \quad (2.58)$$

The rectified dc voltage  $V_{dc}$  can be derived by multiplying the resistance  $R$  and rf current  $I = I_0 e^{i\omega t}$ , where  $I_0$  is the amplitude of current and the rectified voltage can be described as:

$$V_{dc} = -a_x I_0 (x_0 - x_R) X' + a_y I_0 p (y_0 - y_R) Y' \quad (2.59)$$

After substituting Eqs. (2.34) and (2.37) into Eq. 2.59, we obtain [127, 193, 194]

$$\begin{aligned} V_{dc} = & \frac{I_0 a}{(1+\tilde{\alpha}^2)\{(\omega_Y^2 - \omega^2)^2 + (\alpha_* \omega)^2\}} \times \left\{ -\frac{\tilde{q}_0}{\kappa} c H_y u_0 \{ \tilde{\beta} \tilde{\kappa} (\omega_Y^2 - \omega^2) + \alpha_* (1 + \tilde{\alpha} \tilde{\beta}) \omega^2 \} - \right. \\ & \frac{\tilde{q}_0^2}{\kappa} H_y h_{ext} \{ \tilde{\kappa} (\omega_Y^2 - \omega^2) + \alpha_* \tilde{\alpha} \omega^2 \} + x_R u_0 \{ \tilde{\beta} \tilde{\kappa} (\omega_Y^2 - \omega^2) + \alpha_* (1 + \tilde{\alpha} \tilde{\beta}) \omega^2 \} + \\ & x_R \tilde{q}_0 c h_{ext} \{ \tilde{\kappa} (\omega_Y^2 - \omega^2) + \alpha_* \tilde{\alpha} \omega^2 \} y_R p u_0 \times \{ \tilde{\kappa} (\omega_Y^2 - \omega^2) + (\tilde{\alpha} - \tilde{\beta}) \alpha_* \omega^2 \} + y_R \tilde{q}_0 c p h_{ext} \alpha_* \omega^2 - \\ & \left. \frac{\tilde{q}_0}{\kappa} c p H_x u_0 \{ \tilde{\kappa} (\omega_Y^2 - \omega^2) + (\tilde{\alpha} - \tilde{\beta}) \alpha_* \omega^2 \} + \frac{\tilde{q}_0^2}{\kappa} p H_x h_{ext} \alpha_* \omega^2 \right\} \end{aligned} \quad (2.60)$$

We can consider the proportionality constant  $a_x \sim a_y = a$  because of the rotational symmetry in the circular disk. The Oersted field from the RF current can be calculated by Biot-Savart's law. After the calculation of Oersted field and current density in the system, the comparison between the Oersted field  $q_0 h_{ext}$  and spin torque  $G u_0$  is

$$q h_{ext} : G u_0 \sim 8 : 1 \quad (2.61)$$

The above results indicate that the RF-Oersted field is more dominant than the spin torque in micron-scale disks. After simplifying the vortex dynamics equation, the rectifying spectra can be written as [98], [99], [127] :

$$V_{dc} = -\frac{I_0 a \tilde{q}_0^2 h_{ext} (\omega_Y^2 - \omega^2)}{(1+\tilde{\alpha}^2)\{(\omega_Y^2 - \omega^2)^2 + (\alpha_* \omega)^2\}} H_y + \frac{I_0 a \frac{\tilde{q}_0^2}{\kappa} h_{ext} \alpha_* \omega^2}{(1+\tilde{\alpha}^2)\{(\omega_Y^2 - \omega^2)^2 + (\alpha_* \omega)^2\}} p H_x \quad (2.62)$$

The first term is proportional to the  $y$ -component of the external field, and the spectrum shape correlates with the dispersion function. The second term is proportional to the polarity and  $x$ -component of the external field, and the spectrum shape corresponds to the Lorentzian function.

Fig 2.16(a) shows the schematic of polarity estimation simulated from the equation 2.62 over a range of external field in  $x$ -direction, whereas Fig 2.16(b) shows the circulation estimation simulated over a range of external field in  $y$ -direction.

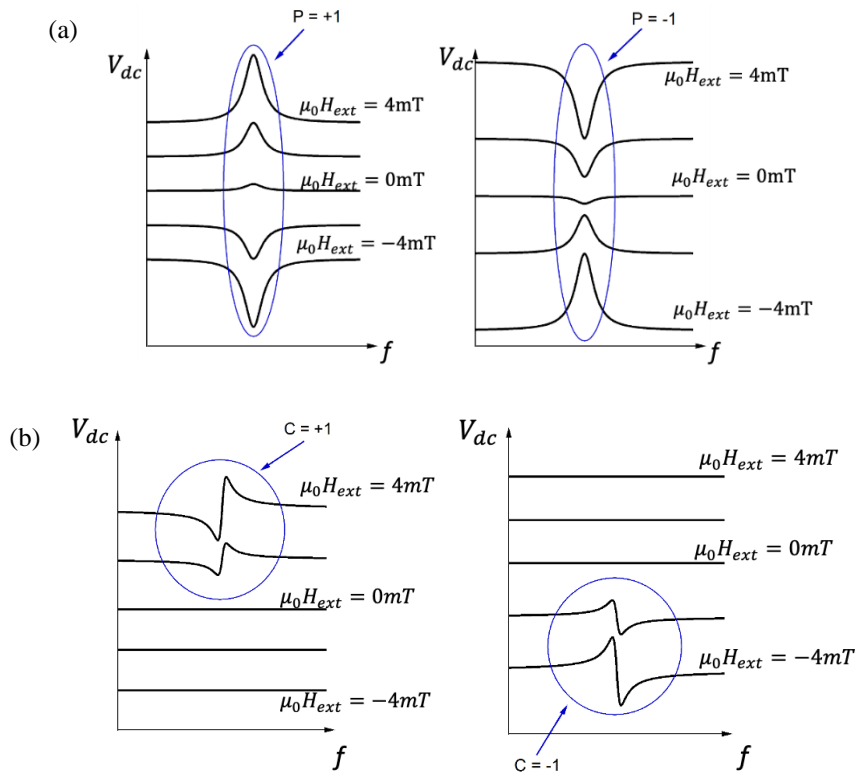


FIG 2.16 (a) Drawing of voltage spectrum peaks showing the up and down polarity derived from the dc voltage equation. (b) Shows the drawing of clockwise and counterclockwise circulation and voltage spectrum shape and signal in the positive and negative field.

## 3. Characterization Techniques

This chapter describes the techniques used for the characterization of magnetic vortices. The focus is on the selective writing and electrical readout [201] of the vortex states. The various methods involve the sensing of polarity and also the circulation of a vortex state by magnetic force microscopy [202, 203] (MFM), Magnetic transmission X-ray microscopy (MTXM) using magnetic circular dichroism (XMCD) [204–210], Lorentz transmission electron microscopy (LTEM) [211]. Static anisotropy magnetoresistance measurement (AMR) [89, 212–215] can detect the annihilation and nucleation field and the sense of the spin circulation. The Magneto-optical Kerr effect (MOKE) can be used to measure hysteresis loops of the whole disk. Most of the techniques mentioned above are used in the static regime because the measurement times are very long compared to the characteristic timescale of the magnetization processes. The method capable of providing fully time-resolved experiments is mainly the MTXM and TR-MOKE. MTXM can observe magnetic vortex dynamics during the annihilation, nucleation, and relaxation of the vortex core. At the same time, this measurement can happen if you get the time scale in ALS synchrotron, and it is not easily accessible and not usable for applications, and TR-MOKE has a low resolution on domains. To avoid these issues, we made an electrical setup at our institute for heterodyne detection using the AMR effect to read out the vortex states [128, 134, 167, 193, 194, 196, 216, 217]. This setup also allows the application of the magnetic field pulses to write the desired vortex state selectively.

### 3.1 Magnetic force microscopy

Magnetic force microscopy [218] (MFM) is atomic force microscopy [219] (AFM) with probes coated by the magnetic layer. The AFM technique relies on the measurement of force acting between the sample and a very sharp tip. The tip is made of Si and mounted on a cantilever, which has built on a holder. The tip has a radius of less than 10 nm, and it is coated with a thin magnetic layer to make it sensitive to the magnetic field. The sample is scanned with the tip, and forces acting on the tip are deduced from the deflection of cantilever. The deflection is further detected optically by a laser beam reflected from the cantilever's backside towards a four-quadrant photodiode, as shown below in Fig 3.1 (a). Optical detection is used to visualize the small deflection of the cantilever.

MFM is one of the standard methods for imaging the magnetic nanostructures. It uses non-contact AFM probes. In this mode, the cantilever is forced to oscillate at its resonance frequency by the piezo-driven element placed under the holder. The MFM microscope works in a “Lift-mode”, where the probe scans the sample surface twice, as shown in Fig 3.1 (b). The first scan is done in the contact mode and provides the topography details where the feedback is ON. In contrast, the second scan is done at some height (~10-20 nm) where the magnetic force dominates and depends on the deflection caused by the cantilever stray field above the sample surface, and the feedback is OFF.

Mostly hard magnetic CoCr tips are used. If they are appropriately magnetized along the tip direction ( $z$ -direction), they will have well defined and constant magnetization. But for our purpose, we used the

Olympus AC240TS probes, which were home-made [72], permalloy, and cobalt coated. Generally, permalloy coated tips have a lower magnetic moment.

The low moment tips are needed because the standard ones may displace the vortex core. However, permalloy is a soft magnetic material, so it can be easily re-magnetized, which forbids measurement in the external fields. The cobalt coated tips are harder to be re-magnetized so that they can be used for the vortex core imaging in the external fields.

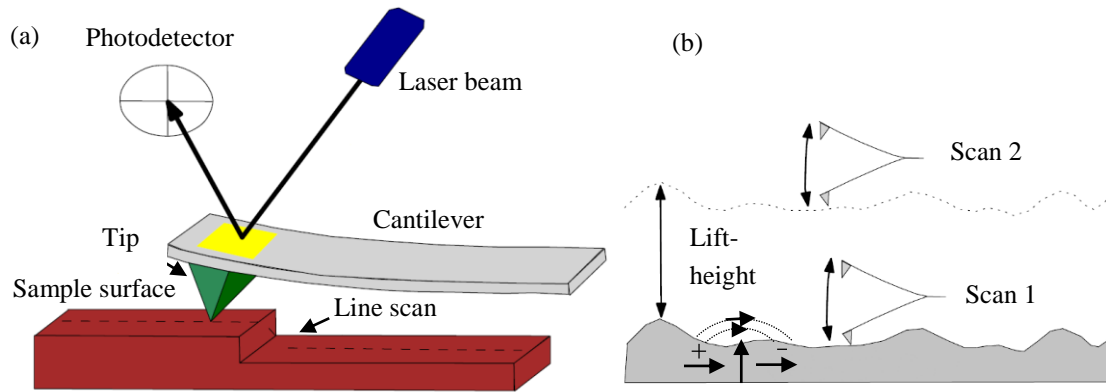


FIG 3.1 (a) Basic principle of AFM. The cantilever tip scans the sample surface, and a four-quadrant photodiode detects the deflection [220]. (b) Lift mode, where at scan one, the topography is measured, and at scan two, the magnetic stray field is detected.

### 3.2 Magnetic transmission X-ray microscopy (MTXM)

This technique is widely used for the element-specific characterization of the magnetic thin film and multilayers. The simplest explanation of x-ray absorption is based on the spin-orbit interaction in the single-electron model. The most used absorption edge is  $L_{2,3}$  of 3d transition metals ( $2p - 3d$  transition). In case of Fe metal at  $L_3$  edge, left circularly polarized photons (LCP) excite 37.5% spin-down electrons and 62.5% spin-up electrons. The situation is reversed in case of  $L_2$  absorption edge, LCP photons excite 75% spin-down electrons and 25% spin-up electrons. While right circularly polarized (RCP) photons give an inverse proportion of the excited spins at two edges. The excited electrons are moved to the magnetically split 3d band, as shown in Fig 3.2. Where in  $L_3$  absorption edge, the RCP photons will be much less absorbed than LCP photons. The opposite happens in the case of  $L_2$  edge [81, 221]. MTXM requires polarized x-ray photons, which can be obtained at a synchrotron radiation source where electrons are circulating in the storage ring and emit electromagnetic radiation.

#### Experimental setup

The XM-1 microscope located at the beamline 6.1.2 at the Advanced Light Source (ALS), Berkeley, USA, was used for time-resolved magnetic imaging, as shown in Fig 3.3. The XM-1 microscope has a spatial resolution of 25 nm, which is determined by the Fresnel-zone plates. Magnetic contrast is obtained using X-ray magnetic circular dichroism (XMCD), giving absorption coefficients proportional to the projection of the magnetization on the direction of the incoming X-rays. The experimental geometry allowed us to measure the out-of-plane magnetization component in the standard setup. Using a unique holder, where the sample can be oriented at  $60^\circ$  to the X-ray beam, it could also measure the in-plane magnetization component. For the permalloy disks, the images were acquired at the Fe  $L_3$  edge (707 eV).

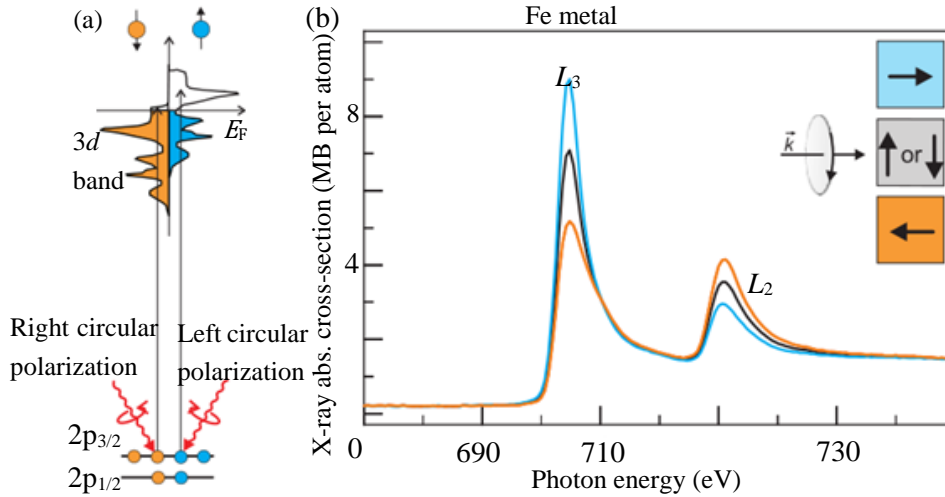


FIG 3.2 XMCD effect for the L-edge absorption in Fe metal [81].

The time-resolved experiments are based on a pump-probe technique enabling the stroboscopic imaging of reproducible events [222]. The time structure of the ALS in 2-bunch mode operation allows synchronizing magnetic field pulses (pump) with the X-ray photon flashes (probes) and recording the temporal evolution of the magnetization in nanodisks for different delays between the magnetic field pulses and photon flashes. The temporal resolution is given by the length of photon flashes (70 ps), arriving at the sample separated by 328 ns. The typical acquisition time for one image is approx. 120 s, i.e., one image is an average of  $\sim 3.7 \times 10^8$  events.

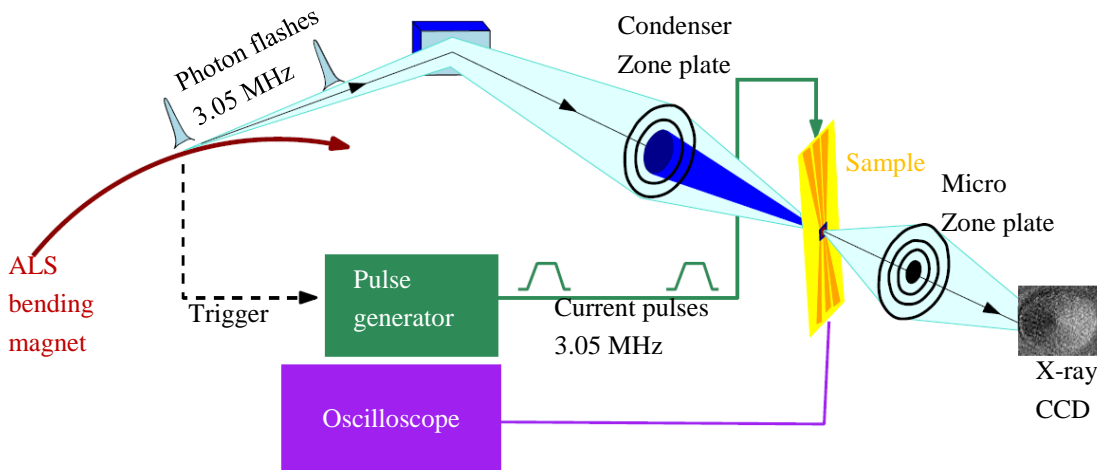


FIG 3.3 Experimental setup for magnetic transmission x-ray microscopy [95].

### 3.3 Magneto-optical Kerr effect

The Magneto-optical Kerr effect is used as one of the significant characterizing techniques to probe the magnetic properties of the sample. It relies on the change of polarization of light upon reflection from a magnetic sample [223]. It has three possible configurations: Polar, longitudinal, and transversal, as shown in Fig 3.4.

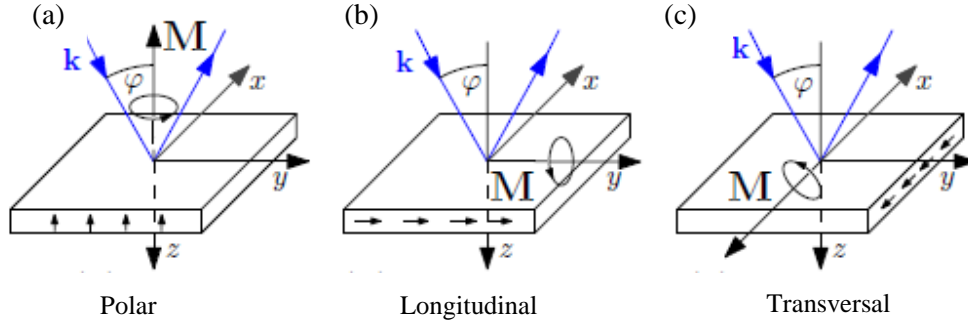


FIG 3.4 Three possible configurations of the Magneto-optical Kerr effect [224].

Lukas Flajsman built the Miranda Kerr apparatus at CEITEC, and more detail is described in his master thesis [224]. He-Ne laser is used as a light source to focus a 500 nm spot and provide a scanning capability of 20  $\mu\text{m}$  scan size. The sample was placed into an electromagnet for varying external magnetic fields produced by a current source. The detector consists of a polarizing beam splitter and two photodiodes. The signal was read by a home-made data acquisition card connected to the photodiodes. For our purpose, we only need the hysteresis loop of the materials; however, the apparatus may also be used for scanning the Kerr microscope. Fig 3.5 shows the vortex measurement, done on permalloy disk by MOKE.

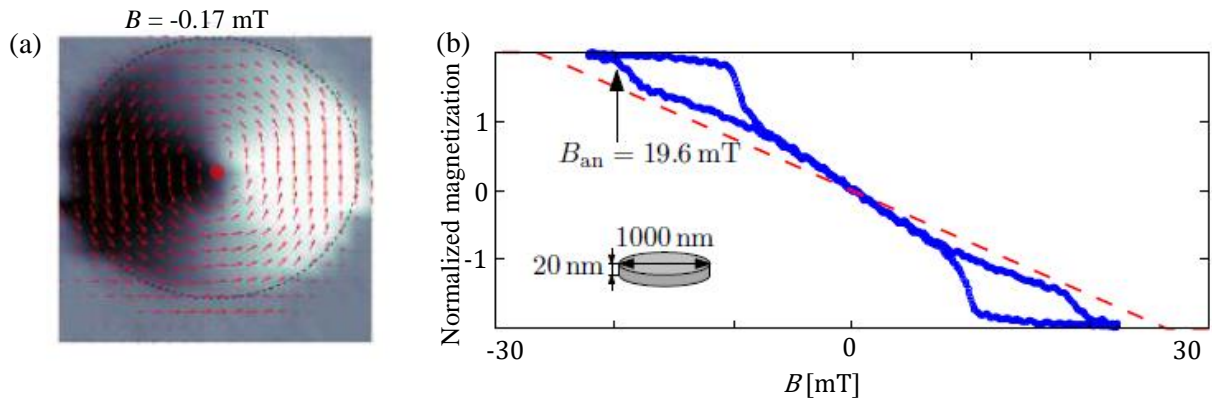


FIG 3.5 (a) vortex state in an external magnetic field. The arrows show the measured vector of magnetization for every individual grid point. The background color corresponds to  $\vec{M}_y$ . (b) Longitudinal magnetization is measured for the permalloy disk. The red curve shows the RVM model [224].

### 3.4 Detection of vortex circulation using Anisotropy magnetoresistance (AMR)

The change in resistivity of a specimen is dependent on the relative direction of the applied magnetic field and the current flow. Generally, resistivity decreases when the applied field and flowing current are perpendicular, while it increases when they are parallel. Resistivity can be defined as:

$$\rho(\varphi) = \rho_{\perp} + (\rho_{\parallel} - \rho_{\perp}) \cos^2 \varphi, \quad (3.1)$$

Where  $\varphi$  is an angle between current density  $\vec{j}$  and magnetization  $\vec{M}$ . Resistance is  $\rho_{\parallel}$  for  $\varphi = 0^\circ$  and  $\rho_{\perp}$  for  $\varphi = 90^\circ$ . We can define the magnetoresistance as a relative change of resistance concerning the saturation value as written in equation 2.56:

$$\text{magnetoresistance} = \frac{R - R_{\text{sat}}}{R_{\text{sat}}} \cdot 100\%$$

### Detection of vortex circulation by AMR

We used the static AMR [215] to detect the vortex circulation. There are two-probe [214, 225] and four-probe [212, 213, 226, 227] AMR methods for detecting the vortex circulation.

We placed the electrodes on one half of the disk, causing the high current density between the electrodes, while the other half of the disk has low current density. If the magnetic field is applied in the  $y$ -direction, then the vortex core moves in the  $x$ -direction. If all the magnetic moments are aligned in the  $y$ -direction, it is called a saturation state and has the highest saturation resistance. If the vortex core is shifted either in between the electrodes or away from the electrodes, it has less resistance because some magnetization is in the  $x$ -direction, also as shown in Fig 3.6.

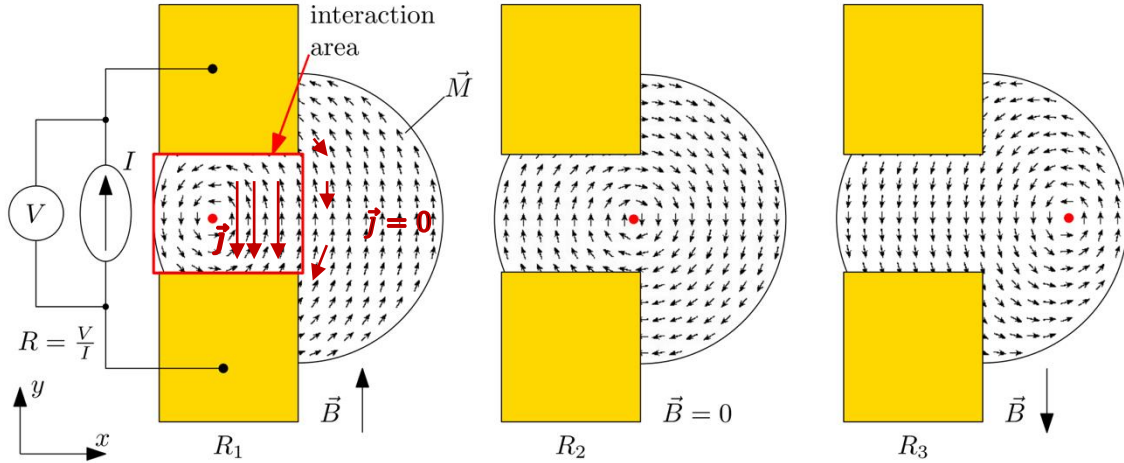


FIG 3.6 Detection area is between the electrodes marked by the red rectangle. Three different positions of the vortex core to the magnetic field are shown. The measured resistance increases (decreases), as the core is shifted outside (inside) the electrodes by the magnetic field. Based on equation (3.1). We can say  $R_1 < R_2 < R_3 < R_{\text{sat}}$ . (adapted from [106]).

We swept the magnetic field from saturation to saturation and performed many cycles, as shown in Fig 3.7. We found out that the presence of a peak only indicates the vortex nucleation through S-state; while the vortex nucleates directly from the saturation, there should be no peak. We swept the magnetic field around the zero value. The core displacement shows a drop or rise of measured resistance, which gives the vortex circulation based on the slope in resistance at zero field. The magnetoresistance curves show a minimum when the vortex core is displaced in the middle of the contact pads, and the position of the minima is either in positive or in negative field depending on the vortex circulation.

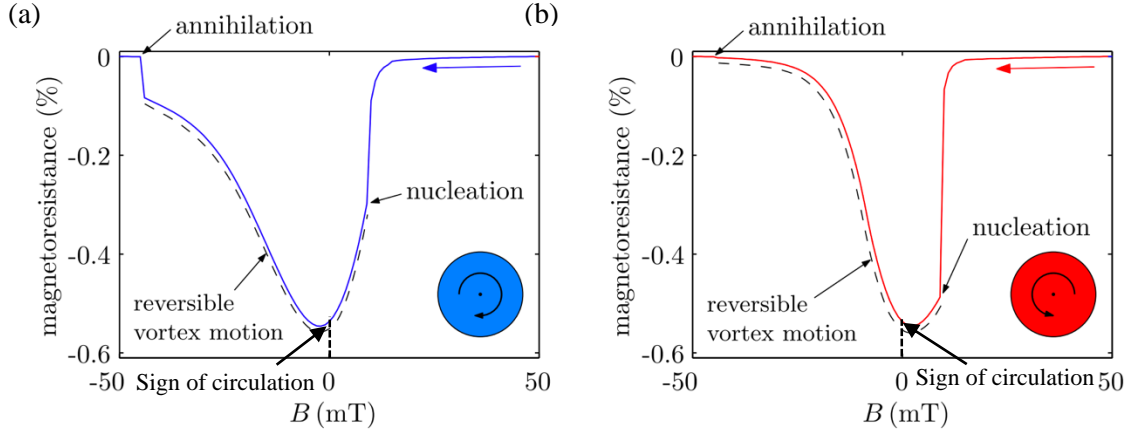


FIG 3.7 (a, b) AMR curve for each (clockwise and counterclockwise) circulation distinguished by the opposite slope at  $B = 0 \text{ mT}$  (From [106]). After the nucleation of a vortex state, the curves follow the reversible vortex motion until it is annihilated. The annihilation step is different because the change is much bigger when the core is annihilated between the electrodes.

### 3.5 Heterodyne detection of vortex states by dynamic AMR measurement

The circulation is possible to measure with static AMR, whereas for polarity, we need dynamic AMR measurement. The AMR depends on the angle between the axis of current flow and the magnetization direction. In a single orbit of vortex core, the resistance will increase twice because both the right and left displacement of the core increases the disk resistance. In case of symmetric placed electrodes on the disk, the change in resistance is described as  $\Delta R \propto x^2 - y^2$ , where  $(x, y)$  is the time-dependent core position measured concerning the disk center. There is no rectified voltage, as the voltage change  $\Delta V \propto \Delta R I_{rf}$  is symmetric around the zero. This symmetry can be changed either by using the non-equilibrium field around the center of the disk or by the asymmetric placement of the electrodes around the disk center. The asymmetric placed electrodes provide a non-zero rectified voltage at resonance because the change in resistance is unequal in left and right displaced electrodes [128, 193, 194, 196]. The asymmetry in the external field dependence can be explained by considering the difference in vortex circulation and the asymmetric electrode position. For the dynamic AMR measurement, we placed the asymmetric electrodes (shifted in the  $x$ -direction) over the disk.


#### 3.5.1 Polarity readout


For the polarity readout, the external field is applied in the  $x$ -direction, displaces the vortex core in the  $y$ -direction. When the rf signal flows through the electrodes to the ferromagnetic disk, it gives a perpendicular rf field, which will keep the vortex core to gyrate at its position, which further leads to oscillation in the resistance. When the rf frequency is equal to the resonance frequency, we will measure a non-zero rectified dc voltage signal. This can be further described by the dc voltage equation 2.62. The first term in the equation is proportional to the  $y$  component of the external field and describes the circulation only. The second term is proportional to the polarity  $p$  and the  $x$  component of the external field and represents only the polarity.



$$V_{dc} = -\frac{I_0 a \tilde{q}_0^2 h_{ext} (\omega_Y^2 - \omega^2)}{(1 + \tilde{\alpha}^2) \{ (\omega_Y^2 - \omega^2)^2 + (\alpha_* \omega)^2 \}} H_y$$

$$+ \frac{I_0 a \frac{\tilde{q}_0^2}{\tilde{\kappa}} h_{ext} \alpha_* \omega^2}{(1 + \tilde{\alpha}^2) \{ (\omega_Y^2 - \omega^2)^2 + (\alpha_* \omega)^2 \}} p H_x$$

Dispersion function 

Lorentzian function 

The change in core polarity can change the sense of core gyration and the sign of rectified voltage, generating a core polarity dependent voltage peak for  $H_x > 0$  at gyrotropic frequency. For a particular core polarity, the signal polarity is also changed by changing the sign of  $H_x$ . As the dc voltage is directly proportional to the polarity  $p$  and external field value in the  $x$ -direction; thus, when the external field is applied in the positive direction, the voltage signal will be positive. We will get the up polarity ( $p = +1$ ), and when the external field is applied in the negative direction, the output voltage will also be in the negative direction. It will define the negative polarity ( $p = -1$ ), as shown in Fig 3.8.

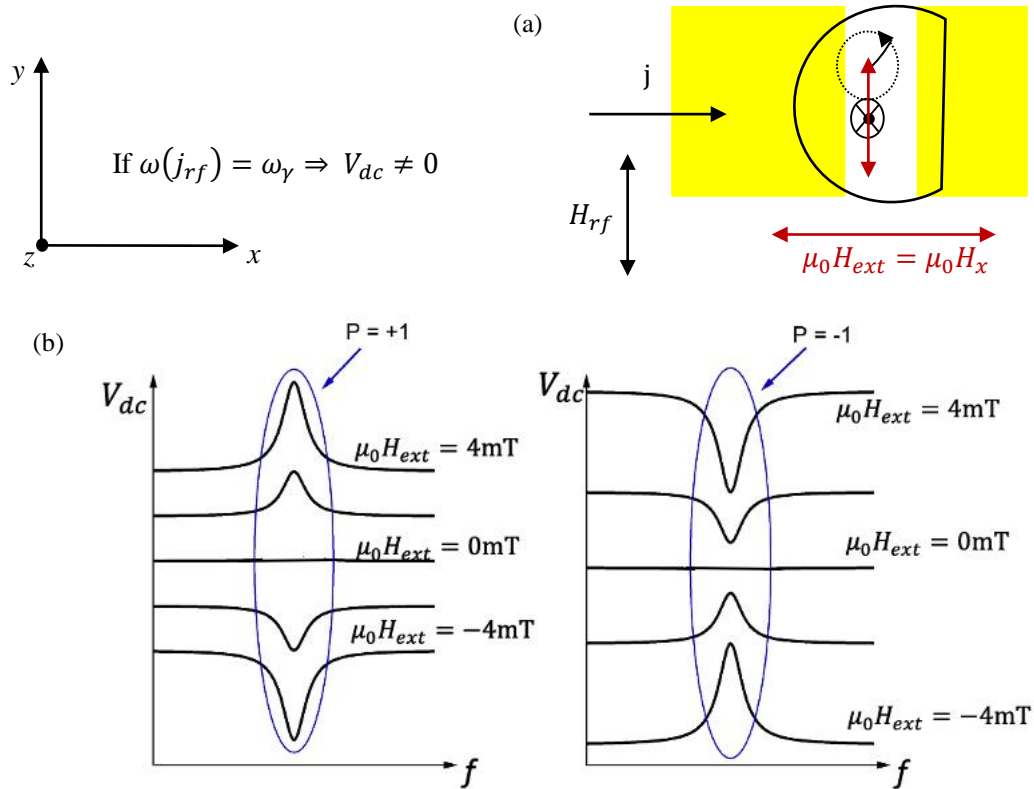


FIG. 3.8 (a) Configuration of the asymmetric electrodes over D shaped disk. (b) Drawing of voltage spectrum peaks showing the up and down polarity derived from the dc voltage equation.

### 3.5.2 Circulation readout

For the circulation readout, the external field is applied in the  $y$ -direction, and the vortex core moves in the  $x$ -direction. Whenever the vortex core moves under the Au electrode, the rectified voltage signal decreases. In contrast, the rectified voltage signal is detected if the vortex core is in between the gap of electrodes.

The gap of the center conductive stripline is shifted to the  $x$ -direction from the center of the disk, as shown in Fig 3.9(a). This asymmetric electrode position affects the asymmetric external field dependence of the rectifying voltage, as in Fig 3.9 (b & c). The external field dependence of rectifying voltage spectra changes as the sign of circulation is reversed. When the external field is applied in  $+y$  direction with clockwise circulation, the vortex core moves to the  $+x$  direction, which is in between the gap of electrodes, and we can see the rectifying voltage spectra as in Fig 3.9(b). On the other hand, when the external field is applied in  $+y$  direction with counterclockwise circulation, the vortex core moves to the  $-x$ -direction below the electrode, and the rectifying voltage spectra vanishes as in Fig 3.9(c).

When the external field is applied in the  $-y$  direction for clockwise circulation, the vortex core moves in the  $-x$  direction, below the Au electrode, and there is no voltage spectrum. In contrast, when the external field is applied in the  $-y$  direction for counterclockwise circulation, the vortex core moves in the  $+x$  direction in between the gap of the electrodes, and we get the rectifying voltage signal.

The voltage spectrum shape for circulation can also be described by the dc voltage equation 2.62, where the first term is proportional to the  $y$  component of the external field. The voltage spectrum shape

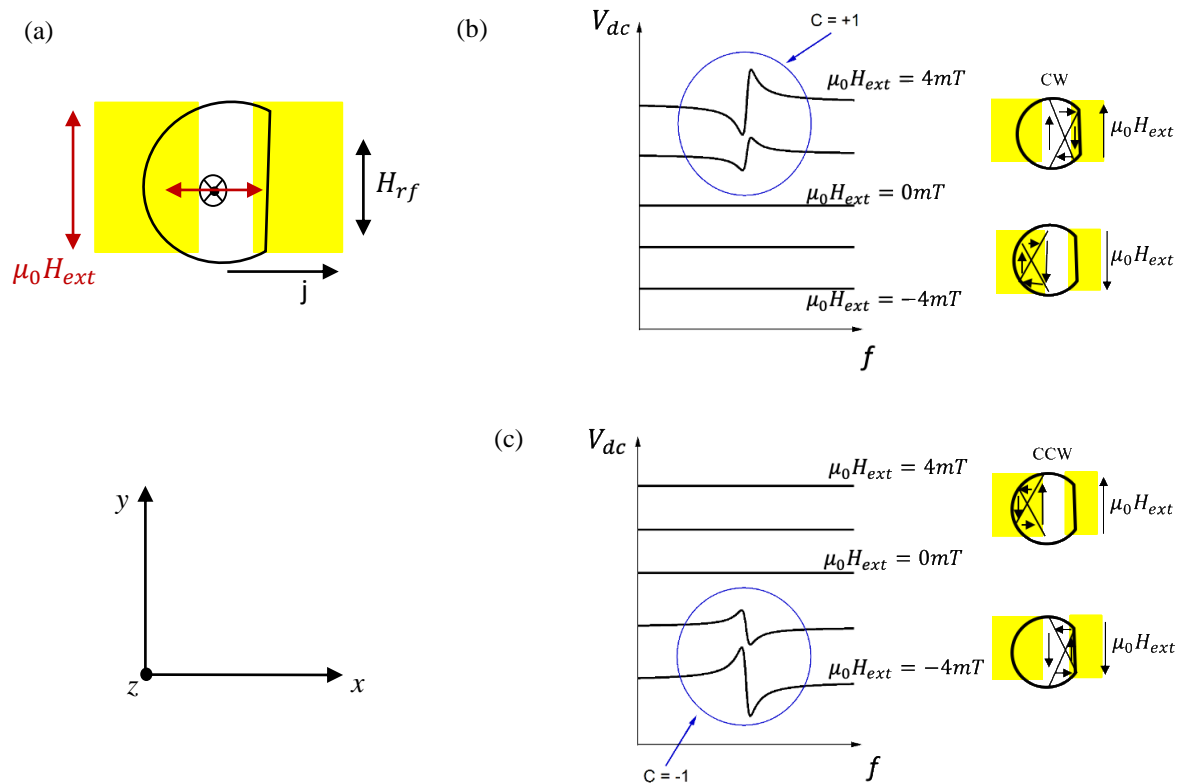


FIG 3.9 (a) Schematic of electrodes over the disk and the external field is applied in  $y$ -direction so that the core moves in  $x$ -direction. (b) Illustration of clockwise circulation, and voltage spectrum shape, and signal in the positive and negative field. (c) Drawing of counterclockwise circulation with the application of the external field.

correlates with the dispersion function. Therefore, when the external field is applied in the  $+y$  direction, the minus sign will reverse the voltage spectrum shape, and we get the down to up signal with clockwise circulation. In contrast, when the external field is applied in  $-y$  direction, it will give up to down voltage spectrum shape with counterclockwise circulation.

### 3.5.3 Electrical Schematic

The electrical schematic for the dynamic AMR measurement is described in Fig 3.10. The signal generator sends the rf current for the readout of the vortex state. A Bias-tee was used to measure the rectified DC voltage between the electrodes, which separates the DC and RF components of the current. The pulse generator was used to send the pulses for controlling the vortex states. Rectification converts an oscillating sinusoidal voltage signal to DC voltage.

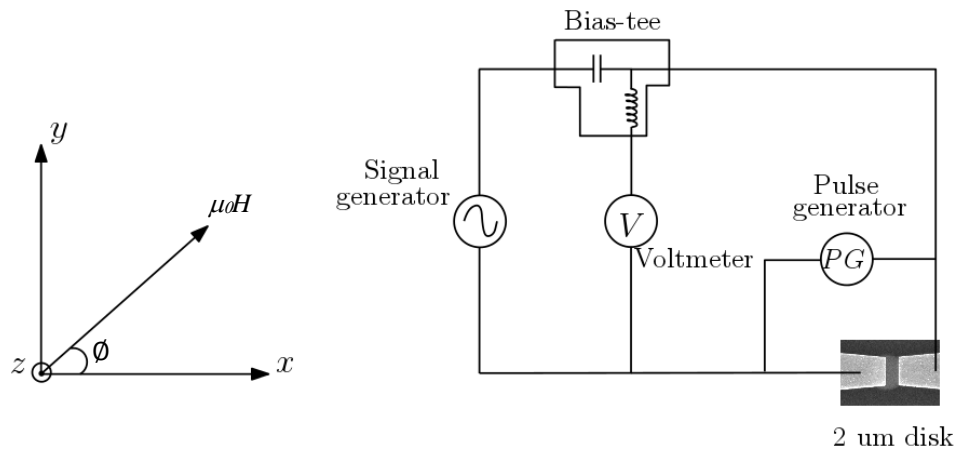


FIG 3.10 Electrical schematics for the dynamic AMR measurement. A signal generator was used to send out the continuous signal for readout, whereas a pulse generator was used to send out the pulses for the writing of vortex states. The magnetic field was applied to the sample in-plane and out-of-plane of the disk.

## 4. Sample Fabrication

In this chapter, we describe the preparation of the samples used in this thesis. Permalloy nanodisks with diameters ranging from 500 to 4000 nm and the thickness ranging from 20 to 40 nm on gold waveguides (1000-3000 nm) were fabricated by electron-beam lithography, photolithography, and by the lift-off process [228–230]. For the MTXM experiments, we fabricated a gold waveguide in the first step, and then we place magnetic disks on top of the waveguide in the second lithography step. The whole structure was fabricated on a 200 nm thick  $\text{Si}_3\text{N}_4$  membrane to ensure the transparency of soft x-rays. While for AMR measurement and other electrical measurements, the permalloy disk was patterned directly on the Si wafer in the first step, and the gold electrodes were patterned on the disk to measure the signal through the disk. The entire structure was fabricated on 100-300 nm thick  $\text{SiO}_2$  or  $\text{Si}_3\text{N}_4$  deposited over Si wafer to prevent any current leakage. For electrical measurement, the samples were wire-bonded to a custom-designed printed circuit board capable of working at frequencies up to 16 GHz. A detailed description of the whole process is described below.

### 4.1 Lithography techniques for nanofabrication

In nano and microfabrication, photolithography and electron-beam lithography [231–234] are the most widely used techniques. They are used to fabricate IC's (Integrated Circuits), MEMS (Microelectromechanical System), NEMS (Nanoelectromechanical System), Sensors, and produce structures smaller than 10 nm.

#### 4.1.1 Lithography resists

Lithography uses pattern transfer by exposing selected parts of the so-called resist layer by electrons, ions, or photons. The exposed (or unexposed) parts of the resist layers are removed by the developer.

There are two main types of resists used in the process:

1. *Positive resist*: In the case of positive resist, the exposed area dissolved during chemical development. The positive resist used in photolithography are AR-P 3100, AR-P 3200, AR-P 5300, and the positive e-beam resists are PMMA, CSAR 6200.
2. *Negative resist*: In the case of negative resist, the exposed area hardens and remains in place after chemical development. The negative photoresists are AR-N 4200, AR-N 4300, and negative tone e-beam resists are hydrogen silsesquioxane (HSQ), AR-N 7520.

Fig. 4.1 shows the positive and negative resist mask fabrication process.

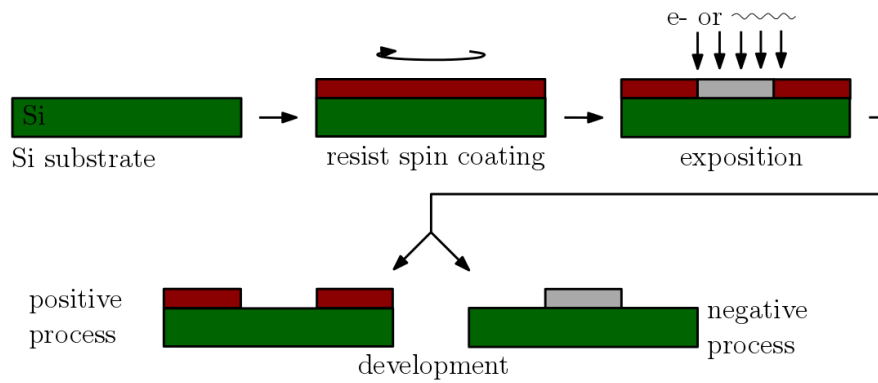


FIG 4.1 Schematics of a resist mask fabrication process. A resist layer is spin-coated onto a clean substrate, usually silicon wafers. The samples are then exposed by electrons or by photons and developed. The process can be either positive (exposed parts are dissolved) or negative (exposed parts remains) [106].

#### 4.1.2 Photolithography

The first and most widely used lithography [235–239] is photolithography using UV (ultraviolet) light ( $\lambda \cong 0.2 \mu\text{m}$  or  $\lambda \cong 0.4 \mu\text{m}$ ) or deep UV light ( $\lambda \leq 0.2 \mu\text{m}$ ), which is used to transfer the pattern from the mask on to the thin film. The UV light is transmitted through the transparent part of the mask; the exposed area will then be developed in the developer based on resist used. This makes the transfer of the pattern from the mask on the wafer. The wafer is then processed either by the etching or lift-off techniques to selectively remove the undesired portions. The steps for the photolithography preparation of wafers:

- *Spin coating of the resist:* The spin coating is a widely used procedure to deposit a uniform thin film of the solvent over the substrate. A circular substrate (wafer) or masks are used for the spin coating of photoresist. The photoresist is a radiation-sensitive organic polymer. To spin-coat the wafer, a small volume of the resist is dispensed to the wafer placed on the spin coater chuck. The wafer is held by the vacuum and rotated at high speed to get the desired thickness of resist film. Sometimes adhesion promotor is also used below the resist layer to enhance the adhesion between the resist and very top layer. For the best adhesion possible, the wafer must be cleaned correctly. As the resist is volatile, the extra amount of resist evaporates during spinning. The speed varies with the required film thickness. The thickness also depends on the viscosity and the concentration of the solution. The machine used for this purpose is called the spin coater or spinner. Spin coating can quickly produce uniform thin films in a micrometer to the nanometer range.
- *Soft bake of the resist:* After the spin coating of the resist, the resist needs to be soft-baked to remove the residual solvent and to densify the resist film. It also eliminates the stress from the resist layer, promotes adhesion, and helps in better processing later steps.
- *Exposure:* In the first step of exposure, the wafer does not require to be aligned with the mask, but in case of second and further exposures, the wafer needs to be aligned well with the features of the masks. Then the UV light is shined on the mask; the light will pass through the transparent area of the mask and expose the resist. Due to exposure to the photoactive compound of photoresist, the photoresist will undergo a selective chemical reaction in the exposed region.
- *Post-exposure bake:* Sometimes, after exposure, the resist needs to be baked for further chemical reaction, contrast enhancement, or stress relaxation.

- *Development*: In the development process, the selective dissolving of the resist takes place. Now, this selective dissolving depends on the type of photoresist used. After exposure of the positive photoresist, the exposed area will become soluble in the developer and removed during the developing process. The pattern after development is the same as on the mask. While in the case of negative photoresist, the exposed area undergoes a chemical reaction that causes crosslinking of the resist molecules, making it insoluble in the developer. The exposed area remains on the wafer, and the unexposed area is dissolved in the developer.
- *Hard bake*: Hard bake is an optional process. It is performed to remove the volatile compounds and water and make the resist stiffer and more durable in further etching process (e.g., wet chemical etching).

The main disadvantage of photolithography is its difficulty producing the structures below 100 nm directly because of the diffraction effect. There are techniques such as dual exposure or structure splitting, allowing to achieve higher resolution structures by application of subsequent processes. In R&D applications, this drawback is usually overcome by using electron-beam lithography, which is much slower but can achieve higher resolution.

#### 4.1.3 Electron-beam lithography

The electron beam lithography (EBL) [240–242] is quite a common technique in R&D, with a limited number of applications in industry. EBL offers high-resolution patterning by high energy electrons (2 to 100 keV). The beam can be focused into a narrow beam area in gaussian scanning systems or shaped into various geometric structures in shape-beam systems. This technique offers precise control of energy and dose delivered to the resist coated wafers. Quite commonly, the masks for photolithography are manufactured by this technique. Typically, the writing strategy does not require a hard mask. Instead, the beam position is precisely controlled by a computer-controlled pattern generator according to a design file.

The resolution of e-beam lithography does not depend only on the spot size of a focused beam, but it is also affected by the scattering of electrons inside the resist and the electron backscattering from the substrate. These effects influence a wider area than the spot size of the focused electron beam. This is called the proximity effect. The proximity effect influence can be suppressed by the application of a proximity correction algorithm. The algorithm calculates proximity corrected structures with modified shapes and doses. The resulting pattern may be quite complicated, and processing may be slow, which further prolongs the time of exposure.

The main advantage of the EBL is that it is a maskless and direct writing technique, and it can pattern up to relatively low resolution (nanopatterns). The main disadvantage is that it is time consuming due to the sequential scanning of an electron beam. Thus, it is suitable for exposure to low-area features.

#### 4.1.4 Lift-off

This technique is the simplest way to obtain the patterns, but it always contains irremovable edge defects. After exposure and development of the resist layer, the materials of interest are sputtered or evaporated onto the sample. The sputtering by the Kaufman or evaporator is more directional than sputtering by Magnetron. During sputtering, some substrate areas were shadowed by the resist layer, and the material cannot be deposited there. This process is called shadowing. While at the opposite edge, the sputtered material is deposited on the resist edge, and it cannot be removed by Lift-off, as

shown in Fig. 4.2. This problem can be solved by using the two resist layers with different exposure doses. The bottom layer with a lower dose undergoes a cut in the resist layer.

On the other hand, the shadowing effect is useful to fabricate tapered nanodisks, which helps in controlling the vortex core nucleation along the tapered side of the disk [95].

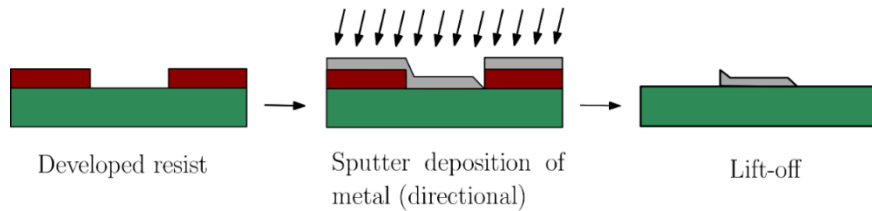


FIG 4.2 Lift-off process with the shadowing effect, where the substrate is not perpendicular to the Ion beam direction [106].

## 4.2 Ion beam etching using the negative mask

In the ion beam etching (IBE) process, an ion resistant mask is prepared on the layer, which is patterned. The below metal can be etched (sputtered) away from the surface by bombarding the sample by high energy ions (mostly  $\text{Ar}^+$ ). The mask can be made of ion resistant polymer or inorganic metal.

### 4.2.1 Resist masks

A negative tone e-beam resist can be used as a resist mask. Mostly hydrogen silsesquioxane (HSQ) [243] and AR-N 7520 are used as a resist mask. HSQ has a very high resolution in the best case  $\approx 5$  nm. An aqueous solution of tetramethylammonium hydroxide (TMAH) or sodium hydroxide (NaOH) is used as a developer. The exposure doses vary with the development processes and the pattern size. After exposure to e-beam, HSQ transforms into  $\text{SiO}_2$  with good etching resistance. For the methods using low doses ( $< 1000 \mu\text{C}/\text{cm}^2$ ), extra electron irradiation can be used to finish the transformation into  $\text{SiO}_2$  and improve the etching resistance. After the IBE process, the remaining mask can be etched in a buffered oxide etch (BOE) or hydrofluoric acid (HF).

The main drawback of using HSQ is, it has a shallow shelf life of only six months and a high price. There are also known adhesion problems of this resist with the sample, especially on the metal surface. Special treatment of extra cleaning of the surface of samples or some adhesion promoter is required.

The negative resist AR-N 7520 is also used as a resist mask. The resist has good resolution and a very low dose compared to HSQ and an easy development process. The disadvantage of this resist is that during the IBE process, resist gets overheated by the bombardment of the ions, and later it is hard to get rid of the resist. Although, some cooling media like fomblin oil can be used in a small drop below the sample surface to keep the sample cold during the IBE process.

The schematics of the ion beam etching process using a resist mask is shown below in Fig 4.3.

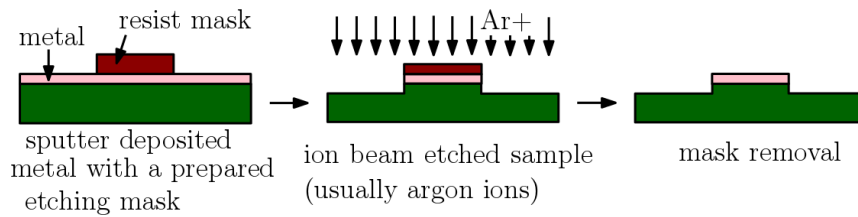


FIG 4.3 Schematics of the ion beam etching process using a resist mask. The patterned layer is sputtered away, and the remaining mask is chemically removed [106].

#### 4.2.2 Metal mask by positive lithography and lift-off

When a suitable resist is not available, a metal mask can be simply prepared by a positive lithography process with lift-off. However, this process has more steps than the previous resist mask process, as shown below in Fig. 4.4. Mostly titanium is used as a metal mask because of its availability and slower etching rate than other metals. The main problem with different metal masks is their removal. Chemicals that dissolve one metal also affect other metal; that's why it is hard to find a suitable etchant for one metal. In some applications, even a thin layer of the remaining metal mask is not suitable for the measurements. Some of the machines have a secondary ion mass spectrometer (SIMS), which is a surface-sensitive technique and stops the process just after the mask is etched but may leave some insignificant residues. This process will make the surface rough and also introduce some defects, which may not be suitable for our purpose.

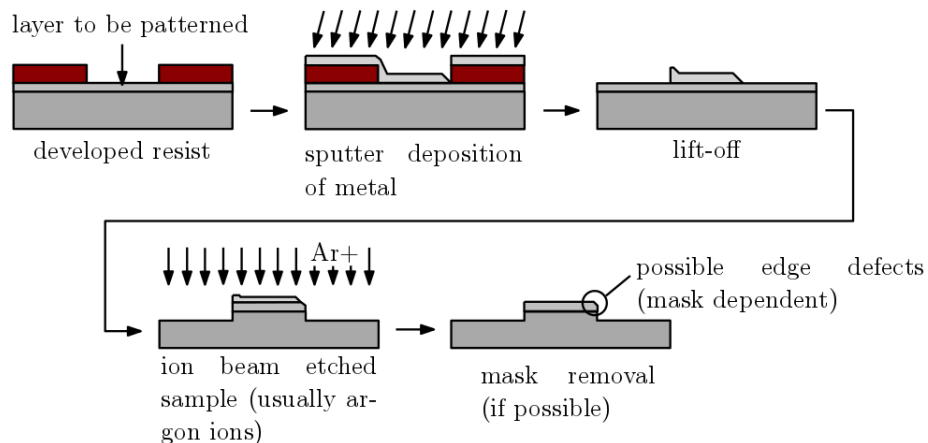


FIG 4.4 Schematics of the ion beam etching process using a metal mask. The mask is prepared by the lift-off process. The patterned layer is sputtered away, and the remaining mask can be chemically removed, or the process can be stopped precisely when the mask is sputtered away completely [106].

Sometimes aluminum can also be used as an etching mask. Its resistance to the ions is lower; therefore, a thicker mask is required. The left-over of aluminum after etching can be removed by TMAH, which is not aggressive to other metals. But TMAH also etches silicon; for this purpose, a substrate with a protective layer of  $\text{SiO}_2$  or  $\text{Si}_3\text{N}_4$  is the most suitable.

### 4.3 Sample preparation for MTXM

Below we described the fabrication steps used for the MTXM samples measurement. For the MTXM measurements, we used 200 nm thin  $\text{Si}_3\text{N}_4$  membranes. The Au waveguide was patterned over the  $\text{Si}_3\text{N}_4$  membrane in the first lithography step; then, the permalloy disks were placed over the Au waveguide in the second lithography step. The schematic of the whole fabrication process is shown in Fig. 4.5.



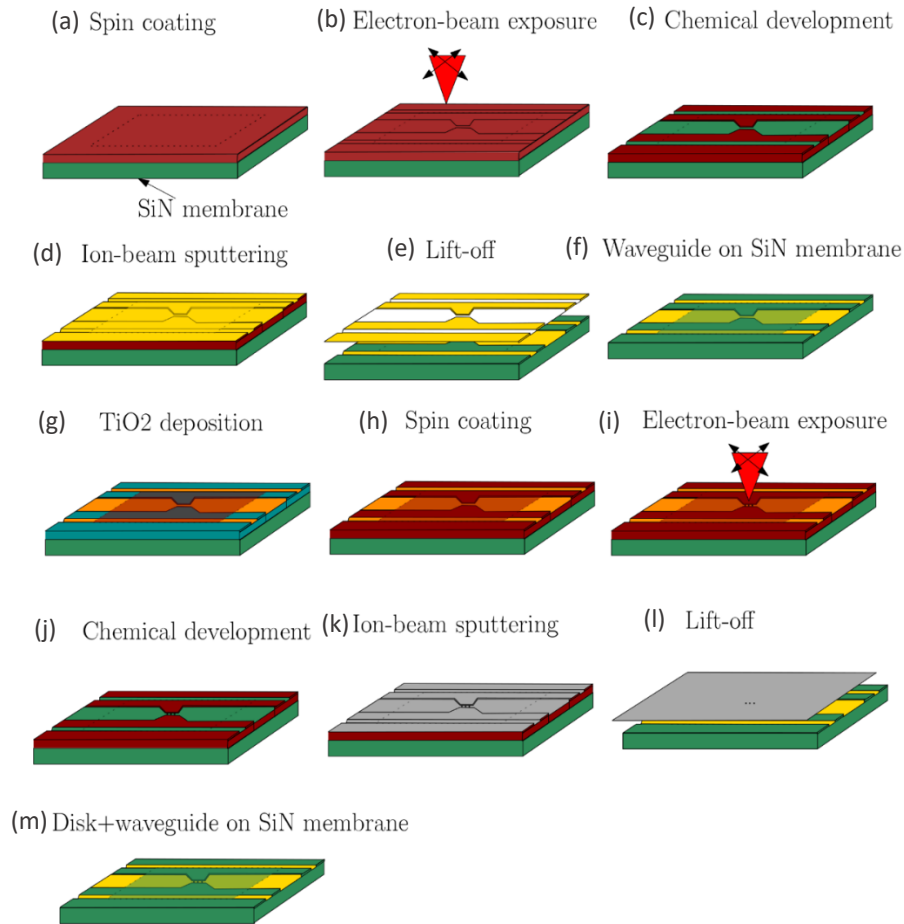


FIG 4.5 Fabrication steps for  $\text{Ni}_{80}\text{Fe}_{20}$  disk over gold waveguide on  $\text{Si}_3\text{N}_4$  membrane for MTXM measurement.

#### (a) Sample preparation and spin coating

The spin coating machine used in our laboratory is the spin coater Laurel 400. For our MTXM measurements, we used  $\text{Si}_3\text{N}_4$  membrane of a  $5 \times 5 \text{ mm}^2$  square frame with a  $3 \times 3 \text{ mm}^2$  wide and 200 nm thin central window for transparency of x-rays. The membrane could not be put on the spin coater vacuum chuck directly, as it would break the membrane. In this case, we glued the membrane to the  $10 \times 10 \text{ mm}^2$  of a silicon wafer to make it easy to work. The various steps used for the spin coating procedure are described below, and the spin-coated schematic image is shown in Fig.4.5 (a).

- Prebaking of  $\text{Si}_3\text{N}_4$  samples on a hot plate at  $180^\circ\text{C}$  for 15-20 minutes to remove the humidity from the samples.
- Spin coating of PMMA (poly-methyl-methacrylate) 950k (allresist AR-P 679.04) resist at 2000 rpm for 1-minute results in film thickness of approximately 350 nm. The spin curve of the resist can be easily found in an allresist datasheet [244].
- Soft baking of the samples on a hot plate at  $180^\circ\text{C}$  for 3 minutes to harden the PMMA layer.

#### (b) Electron-beam lithography (EBL) of the waveguide

Electron beam lithography is a technique used for patterning of nanostructures up to 10 nm resolution. We used e-beam writer MIRA3, which has a resolution of 25 nm, and RAITH 150two with a resolution of 5 nm [245]. Electron beam lithography is quite resembling SEM (scanning electron microscopy) technique. The main difference between the two is that in the electron beam

lithography technique, the electron beam scan over the sample (direct-write) according to the instructions by the pattern generator, while in SEM, an electron beam is raster scanning over the sample surface to collect the secondary electrons to form the image. We used the e-beam writer MIRA3 for our purpose.

We used positive resist, and the sample went twice through the whole fabrication steps described in this chapter to get the final structure for the time-resolved study of magnetization dynamics. The system should be well-calibrated, and there were also lots of parameters during exposure that needed special attention, as described in Table I. The patterns could be drawn in either Draw beam software, in Elphy software, or Klayout. We used Elphy software for patterning purpose, and the calibrated parameters for the patterning purpose are as given in Table 4.1. In the first patterning step, we exposed the waveguide, as shown in Fig. 4.5(b), which is used to apply the field pulses to the sample.

Table 4.1. The calibrated parameters for patterning by TESCAN MIRA3 are given as:

No.	Parameters	Pattern (waveguide & disk)
1.	Beam energy	20 KeV
2.	Beam current	250 pA
3.	Write field	100 $\mu\text{m}$
4.	Step size	10 nm
5.	Dose factor	260 $\mu\text{C}/\text{cm}^2$

(c) Chemical development

After the exposure, the samples were developed in MIBK based developer (allresist AR 600-56) for two minutes. The development was stopped using isopropyl alcohol for 30 s. The samples were washed in deionized water for 30 s and blow-dried by nitrogen while being held in a tweezer. The development of the sample is checked by optical microscopy. The schematic after chemical development is shown in Fig. 4.5 (c).

(d) Ion beam sputter deposition – Kaufman apparatus

Ion beam sputter (IBS) deposition uses accelerating ions from the source that are directed towards the target, which is to be sputtered. The sputtered material is deposited as a thin layer in a high vacuum chamber. The sputtered atoms are deposited to the target and also on the quartz crystal. The quartz crystal is placed inside the vacuum chamber for thickness measurement. A change in the resonant frequency of crystal and the knowledge about sputtered material can tell about the thickness of the layer. There are three main parts of the Kaufman apparatus:

*Vacuum chamber:* The chamber is a cryogenically pumped system at  $\sim 10^{-7}$  mbar working pressure and operates at  $\sim 10^{-6}$  mbar pressure.

*Ion source:* Mainly wire filament cathodes and neutralizer can be used as an ion source, which is made of W or Ta. There are two ion sources, primary and secondary ion source. The primary ion

source is used to sputter away the material, and the secondary ion source is used for the pre-cleaning of the sample surface before deposition. When the argon gas is injected into the chamber, the high electric field causes the gas to ionize, creating the plasma discharge. The use of reactive gases inside the chamber reduces the lifetime of an ion source.

*Targets:* In our Kaufman apparatus, we can place three targets at a time, but we can use only one target at a time for the sputtered deposition. The use of the target depends on the user application. Generally, the deposition rate varies with the used targets, which further depends on the density of the material, and lots of other parameters also.

The main advantage of the ion beam sputter deposition is that the ion beam provides control over the ion energy, angle of incidence, and beam current. The parameters can be controlled separately to get the desired thickness.

For the waveguides, we used Ti/Au or Ti/Cu and permalloy material for disks. The purpose of the Ti layer was to make an adhesive contact between the nitride and SiO<sub>2</sub> coated Si wafers and the Au layer, and the thickness of the Ti layer was 3-5 nm, and the Au or Cu thickness was 80-120 nm. Thicker Au and Cu layer are suitable for wire bonding and high current rate. The deposition rate of Ti and permalloy was 0.6-0.7 Å/S, and Au was ~2.6 Å/S, and the working pressure of the chamber should be ~10<sup>-7</sup> mbar. The schematic after Ti/Au sputtering is shown in Fig. 4.5(d).

#### (e) Lift-off

It is the most straightforward process to get the desired patterns after the sputtering process. The material of interest was deposited on a chemically developed substrate by sputtering (or evaporation). Then the resist was dissolved in some solvent, generally acetone or PG remover. The part of the material, which was deposited directly on the substrate, would remain on the substrate while the rest was washed away with resist remover.

After lift-off, we got the samples with Ti/Au waveguide structure and the alignment marks, as shown in Fig. 4.5(f). The samples went through the same steps again for the fabrication of the magnetic disks on the waveguide.

#### (f) TiO<sub>2</sub> deposition

The samples with the waveguide and alignment marks were put into atomic layer deposition system Ultratech/CambridgeNanoTech Fiji 200 to deposit 20 nm of the TiO<sub>2</sub> layer to make the insulating layer between the waveguide and the disks, not to short circuit the waveguide and the disks. We used Ti precursor Tetrakis(dimethyl amido)titanium (TDMAT) and H<sub>2</sub>O for deposition of TiO<sub>2</sub> by oxygen plasma, grown at a rate of 0.51 Å/cycle. The schematic after TiO<sub>2</sub> deposition is shown in Fig. 4.5(g).

#### (g) Spin coating of samples for the second step

We used a double layer of resists to get a nice round shaped disk. During e-beam exposure, the bottom resist would get exposed more. After development, it provided refined undercut for the disks to avoid any shadowing effect and a seamless lift-off process. The steps for the spin coating are described below, and the schematic after the spin coating is shown in Fig. 4.5(h):

- Prebake the samples on the hot plate at 180°C for 15 minutes to remove the humidity.

- Spin coating of allresist AR-P 617.02 at 4000 rpm for 1 minute, gave approx. 30 nm thick layer of resist.
- Soft bake the samples on the hot plate at 180°C for 3 minutes to harden the resist.
- Spin coating of PMMA 950k (allresist AR-P 679.04) resist at 4000 rpm for 1-minute, results in approx. 270 nm thick resist film.
- Soft bake of samples at 180°C for 3 minutes to harden the resist.

#### (h) Electron beam lithography of disks

The second lithographical pattern of the disks was created in the GDS format and uploaded to our e-beam lithography system by RAITH 150 two. Global and local marks created in the previous lithography steps on the samples were used to align disks in the right position and for the write field alignment. We exposed the disks area with the electron dose of  $220 \mu\text{C}/\text{cm}^2$  with the beam energy of 20 keV. Beam current of 200-300 pA and step-size 10 nm was used for exposing the area of the disks. The schematic for e-beam exposure of disk is shown in Fig. 4.5(i).

#### (i) Chemical development

After exposure, the samples were developed in MIBK based developer (Allresist AR 600-56) for 1 minute, followed by a stopper (IPA) for 30 seconds. Samples were then rinsed in deionized water for 30 sec. and blow-dried in nitrogen. The schematic of patterned Au waveguide and disks after chemical development is shown in Fig. 4.5 (j).

#### (j) Ion-beam sputter deposition

Home built ion-beam sputter deposition system with broad beam Kaufman-type ion source was used for a directional deposition of 20-50 nm thick permalloy ( $\text{Ni}_{80}\text{Fe}_{20}$ ) layer, and the sputtered permalloy schematic is shown in Fig. 4.5 (k). The samples were tilted by 30 degrees and were not rotated during the deposition. The directional deposition, in combination with the shadowing effect of the thick resist walls, resulted in tapered disks on one side. These taper disks were used for controlled switching of the vortex circulation [45]. The deposition rate for permalloy was 0.5-0.7  $\text{\AA}/\text{s}$ , and the working pressure of the chamber was approx.  $10^{-6}$  mbar.

#### (k) Lift-off

The samples were then placed in acetone for one hour. The membranes were then sprayed with acetone while being held in a tweezer until the excess metal was removed. If the excess metal remained on the samples, the samples were placed back to the beaker with acetone, and the procedure was repeated. Optionally, a megasonic bath can be used to help with the lift-off procedure. The schematic during the lift-off of disks is shown in Fig.4.5(l), and the finished schematic of permalloy disks over Au waveguide on  $\text{Si}_3\text{N}_4$  membrane is shown in Fig. 4.5(m).

We got the final structure consisting of permalloy disks over Ti/Au waveguide on the SiN membrane [246]. The scanning electron microscope (SEM) image of the finished sample is shown in Fig. 4.6.

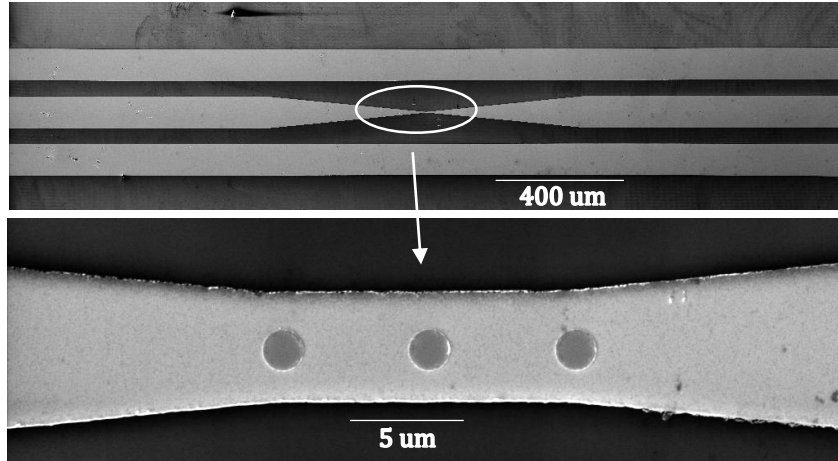


FIG 4.6 (a) Scanning electron microscope image of the gold waveguide with permalloy disks on it. (b) Closer view of disks over the waveguide.

#### 4.4 Sample preparation for dynamic AMR measurement

We used 100-200 nm thick  $\text{Si}_3\text{N}_4$  deposited over Si wafer. The permalloy disk was lithographically prepared directly on  $\text{Si}_3\text{N}_4$  in the first step; then, the gold electrodes were connected to the disk to excite and measure the disk simultaneously. The schematics for the sample preparation steps are shown below in Fig. 4.7.

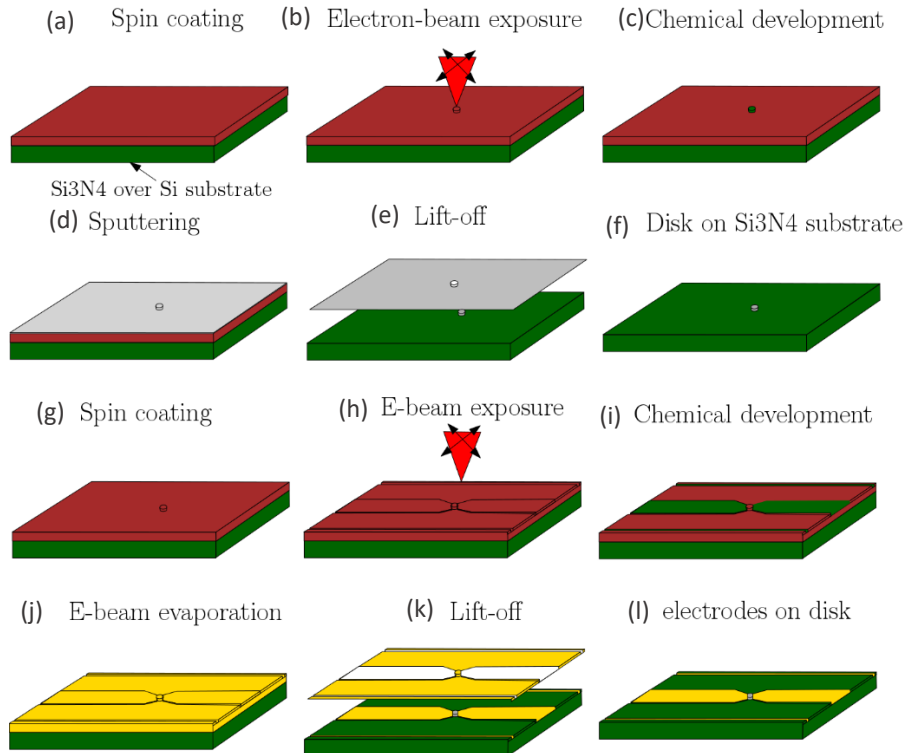


FIG 4.7 Fabrication steps for the gold electrodes over the permalloy disk on Si substrate with  $\text{Si}_3\text{N}_4$  layer for all-electric and read-out measurements.

##### (a) Spin coating

For this batch of samples, we used the SUSS Microtec RCD8 semi-automatic spin coater. This machine can be used for spin coating of small pieces as well as wafers up to 200 mm. We also used

2 and 4-inch wafers to have more samples with a bit extra time and work instead of one by one small sample piece. It saved a lot of time and hard work. The schematic for the spin-coated sample is shown in Fig. 4.7 (a).

We used a double layer of resist to get a nice round shaped disk. During e-beam exposure, the bottom resist would get exposed more, and after development, it provided refined undercut for disks to avoid any shadowing effect and seamless lift-off process. The steps for spin coating were:

- Prebaking the samples on a hot plate at 180°C for 15 minutes to remove the humidity.
- Spin coating of allresist AR-P 617.02 at 4000 rpm for 1 minute gave approx. 30 nm thick layer of resist.
- Soft baking of the samples on the hot plate at 180°C for 3 minutes to harden the resist.
- Spin coating of PMMA 950k (allresist AR-P 679.04) resist at 4000 rpm for 1-minute results in approx. 270 nm thick resist film.
- Soft baking of samples at 180°C for 3 minutes to harden the resist.

(b) Electron beam lithography of disks

The first lithography pattern of the disk with global and local alignment marks was created in the GDS format and uploaded to our e-beam lithography system by RAITH150 Two [245]. Global and local marks on the samples were used for the alignment and proper placement of the second pattern (Au electrodes). The parameters used during the exposure of disk are written below in Table 4.2, and the schematic of e-beam exposure of disk is shown in Fig. 4.7 (b).

Table 4.2. The calibrated parameters for patterning by RAITH150 Two are given as:

No.	Parameters	Pattern (waveguide & disk)
1.	Beam energy	20 KeV
2.	Aperture size	30 μm
3.	Beam current	0.3 nA
4.	Write field	100 μm
5.	Step size	8 nm
6.	Dose factor	220 μC/cm <sup>2</sup>

(c) Chemical development

After exposure, the samples were developed in MIBK based developer (allresist AR 600-56) for 1 minute, followed by a stopper (IPA) for 30 seconds. Samples were then rinsed in deionized water for 30 sec. and blow-dried in nitrogen. The bottom layer of resist doesn't need any special developer; it can be developed by the same developer as used for the upper PMMA resist layer development. The developed disk over the Si sample is shown in Fig. 4.7(c).

(d) Electron beam evaporation/ Magnetron sputtering

We used two sputter deposition techniques for thin film deposition.

*Electron Beam Physical Vapor Deposition (EBPVD) (BESTEC):* EBPVD is a form of physical vapor deposition in which a target anode is bombarded with an electron beam produced by a charged tungsten filament under high vacuum. The electron beam causes atoms from the target to transform into the gaseous phase. These atoms then precipitate into solid form and coat everything in a vacuum chamber with a thin layer of anode material. The permalloy material deposited by EBPVD is suitable for lift-off purposes because the redeposition of material over the resist edge is less. We deposited 20-60 nm of the permalloy ( $\text{Ni}_{80}\text{Fe}_{20}$ ) layer with a deposition rate of  $\sim 1 \text{ \AA/s}$ .

*Magnetron sputtering system (BESTEC):* Magnetron sputtering is another form of the plasma coating process, where the magnetic field is used to keep the plasma in front of the target. The ions are bombarded to the target surface to sputter away the material. The vacuum chamber is filled with inert gases, such as argon. A high voltage creates the glow discharge, resulting in the acceleration of ions to the target surface. The argon ions will sputter away the material from the target surface, gives the sputtered coating layer on the sample. Magnetron sputtering was used for the PMA (perpendicular magnetic anisotropy) multilayer deposition. The PMA layer is a multilayer stack, as shown in Fig. 4.8, grown by the co-sputtering of Co and Pt targets, and the sputtered metallic layer (PMA + NiFe) is drawn in Fig. 4.7 (d).

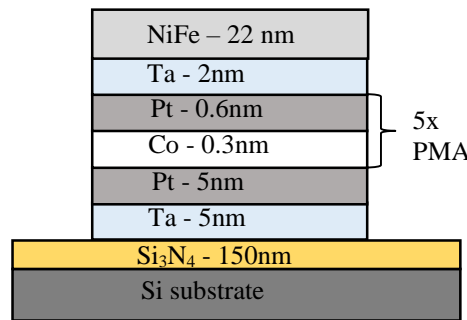


FIG 4.8 Schematic of the sample layer structure, PMA multilayer consisted of five repetitions of 0.3 nm Co and 0.6 nm Pt metal.

Both techniques (EBPVD and Magnetron sputtering) provides the control of electron or ion energy and the angle of incidence. These parameters can be controlled independently, which are necessary to get the desired thickness. The deposition rate was  $\sim 0.5 \text{ \AA/s}$ , and the working pressure of both systems was approx.  $10^{-7}$  mbar.

(e) Lift-off

The samples were then placed in acetone for one hour. Then the samples were sprayed with acetone to remove the excess metal from the sample surface. If the excess metal remained on the sample, the sample was placed back in the beaker with acetone, and the procedure was repeated. Optionally, an ultrasonic bath can be used to support the lift-off procedure. The Drawing of lift-off is shown in Fig. 4.7 (e), and the result of the above five steps are drawn in Fig. 4.7 (f).

(f) Spin coating

We got the samples with the permalloy disk or PMA disk on  $\text{SiO}_2$  over Si substrate. The samples were then spin-coated for the next step.

- Prebaking of samples on a hot plate at 180°C for 15-20 minutes to remove humidity from the samples.
- Spin coating of PMMA (poly-methyl-methacrylate) 950k (allresist AR-P 679.04) resist at 2000 rpm for 1-minute results in film thickness of approximately 390 nm. The spin curve of the resist can be easily found in an Allresist datasheet.
- Post-baking of the samples on a hot plate at 180°C for 3 minutes to harden the PMMA layer.

(g) Electron beam lithography/Direct laser writing (DWL) of electrodes

Direct laser lithography is a fast and high-resolution lithography system used for direct writing of wafers and masks. In our laboratory, we have DWL 66FS laser lithography system. The system can utilize various lasers, which makes it possible to expose nearly all photoresists, including UV resists like SU8. For our samples, we used AR-P 3540 optical resist with 1.4  $\mu\text{m}$  thickness.

The second lithographical pattern of electrodes was created in the GDS format and uploaded to our e-beam lithography system by RAITH150 Two for individual samples or DWL 66FS for a 2 inch or 4-inch wafer. Global and local marks on the samples were used to align and proper placement of electrodes over the disk. The electrodes on RAITH150 Two were exposed with an electron dose of 250  $\mu\text{C}/\text{cm}^2$  at the beam energy of 20 keV with 120  $\mu\text{m}$  aperture. It provides the beam current of 4.5-5 nA, and a step-size of 20 nm was used for exposing the electrodes. The e-beam exposure process of the waveguide is shown in Fig. 4.7 (h).

(h) Chemical development

After exposure, the samples were developed in MIBK based developer (allresist AR 600-56) for 1 minute, followed by a stopper (IPA) for 30 seconds. Samples were then rinsed in deionized water for 30 sec. and blow-dried in nitrogen.

(i) Electron-beam evaporation

Electron-beam evaporator was used for the deposition of the Ti/Au (5/100 nm) layer for the electrodes. The thin layer of Ti was used for the better adhesion of gold over the substrate. The deposition rate for Ti was  $\sim 0.6 \text{ \AA}/\text{s}$ , and for Au was  $\sim 1 \text{ \AA}/\text{s}$ . The working pressure of the chamber was  $\sim 10^{-7}$  mbar.

(j) Lift-off

The samples were then placed in acetone for one hour, followed by the spraying with acetone to remove the excess metal or ultrasonic can also be helpful during the lift-off process. The schematic of the final Au waveguide on disk is shown in Fig. 4.7 (l), and the SEM image is shown in Fig. 4.9.



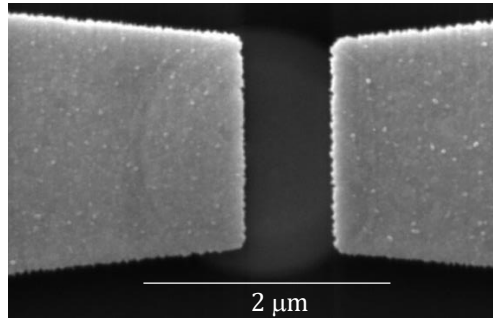


FIG 4.9 SEM image of D shaped 2  $\mu\text{m}$  disk and Au electrodes for static AMR and dynamic AMR measurement.

#### 4.5 Sample preparation for combined (Oersted field and spin torque excitation) measurements

We used 250 nm thick  $\text{SiO}_2$  deposited over Si wafer. The NiFe disk was lithographically exposed on the  $\text{SiO}_2$  in the first step, and then the gold electrodes were connected to the disk to measure the resistivity of the permalloy disk. Another Au waveguide was placed on the top to create the dynamic magnetic field used for disk excitation. The disk and electrodes were separated from the waveguide with a 30 nm thin  $\text{SiO}_2$  insulating layer. The various steps for the fabrication of samples are the same, as described in section 4.5. The schematic is shown in Fig.4.10, and the SEM image is shown in Fig.4.11.

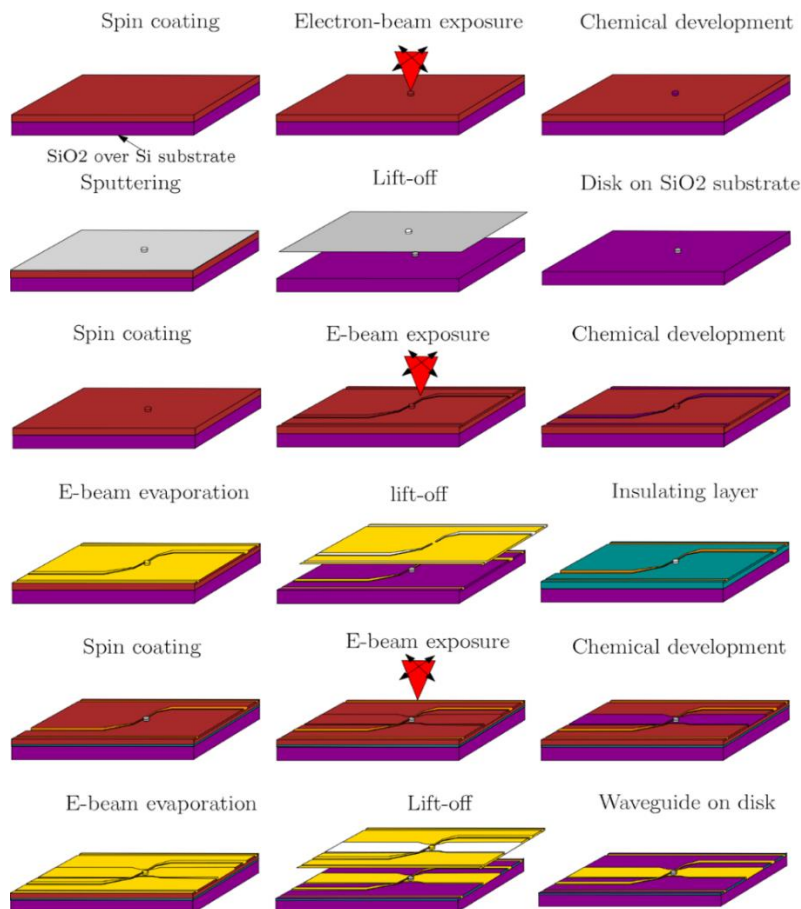


FIG 4.10 Fabrication steps for the gold waveguide over the permalloy disks connected with gold electrodes on  $\text{SiO}_2$  substrate for AMR and other electrical measurements.

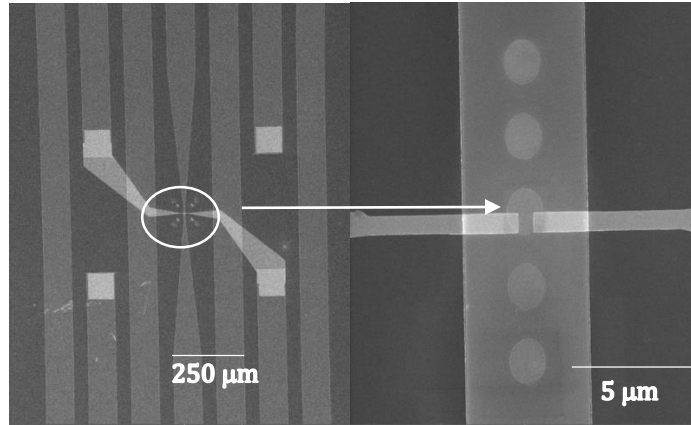


FIG 4.11 SEM image of the gold waveguide with permalloy disk to excite the disk and the signal is measured with the gold electrodes.

## 5. Experiments and Discussion

In this chapter, we will describe the results acquired by various measurement techniques. We start with the static readout of vortex states by MFM and then MTXM while applying different field pulses to switch the vortex states. Later, we added all-electric static and finally dynamic readout of the vortex state. For the electrical measurements, the polarity was controlled using the PMA multilayer and switched by applying a picosecond current pulse. In contrast, the circulation was controlled using the shape anisotropy (D-shaped disk) and switched by applying a nanosecond current pulse. Finally, the statistics of vortex states switching was carried out to determine the reliability of the device.

### 5.1 Static readout of vortex states by MFM

Magnetic force microscopy measurements were done by Bruker Dimension Icon Scanning probe microscope. We used the MFM technique for sensing the polarity and the circulation after applying either the static external field or a magnetic field pulse. As the stray field [87] is present only at the vortex core in a magnetic disk, the readout of polarity is straightforward, while the sensing of spin circulation needs a modified approach. For the circulation readout, we can either put the sample into the magnetic field and measure the position of the displaced vortex, or we can make a small cut (defect) into the disk (by Focused Ion Beam) to break flux closure as shown in Fig 5.1 (b). We used Olympus AC240TS probes sputter-coated with 30-50 nm of Co and NiFe to imaging the displaced vortex core.

#### (a) Sample Description

An array of disks was fabricated by e-beam lithography and lift-off procedure. We used 200-300 nm thick SiO<sub>2</sub> deposited onto a Si wafer. The permalloy disks with diameters ranging from 1-2  $\mu\text{m}$  and thicknesses varying from 20-35 nm were exposed on the Si wafer. The permalloy layer was evaporated using an evaporator and then lifted-off in an acetone bath. For the circulation readout, the disks were trimmed by focused ion beam (FIB) at the edge. A detailed description of the sample fabrication is written in chapter 4.

#### (b) Experimental setup

The experimental setup for the MFM measurement with the electrical current is shown in Fig 5.1 (a). For generating the magnetic field pulses, AVTECH AVM-4-B pulse generator was used. The electric current was sent through the sample, and the voltage signal at the sample was detected on an oscilloscope, while the magnetic configuration was imaged by MFM. The microscope needs to be well-calibrated, and it should not contain any magnetic parts in the vicinity of the sample, which may influence the measurement.

The field pulses from the pulse generator were sent to the sample for different time scales of 1-5 ns and voltages 5-8 V. After sending the field pulse, the vortex core is displaced towards the edge of the disk, and the final vortex states were imaged by the MFM. The field pulses were sent both in forward and reversed direction to see the change in vortex polarity and circulation. The rise time and fall time of the applied pulses play a crucial role in switching polarity and circulation.

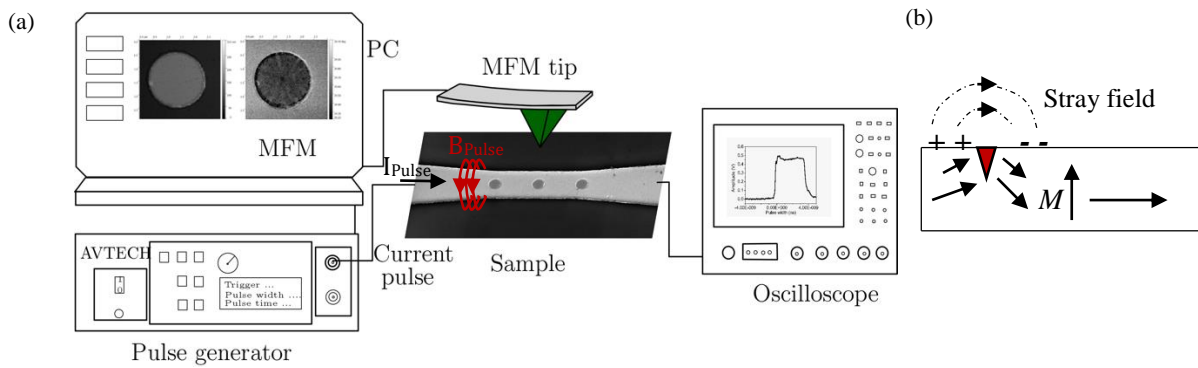


FIG 5.1 (a) Experimental setup for the vortex states measurements by MFM, where the pulse generator sends the field pulses to the sample, and the signal through the sample was detected on an oscilloscope. (b) The stray field around the defect in permalloy disks. (For circulation measurement).

### (c) Results

We performed measurements on 20 samples, and out of them, one of the results is shown below in Fig 5.2, and the disk and pulse parameters are given in Table 5.1.

Table 5.1. Disk and pulse parameters used for circulation and polarity switching

Disk parameters		Pulse parameters	
Disk size	2 $\mu\text{m}$	Pulse width	2 ns
Disk thickness	30 nm	Amplitude	5V

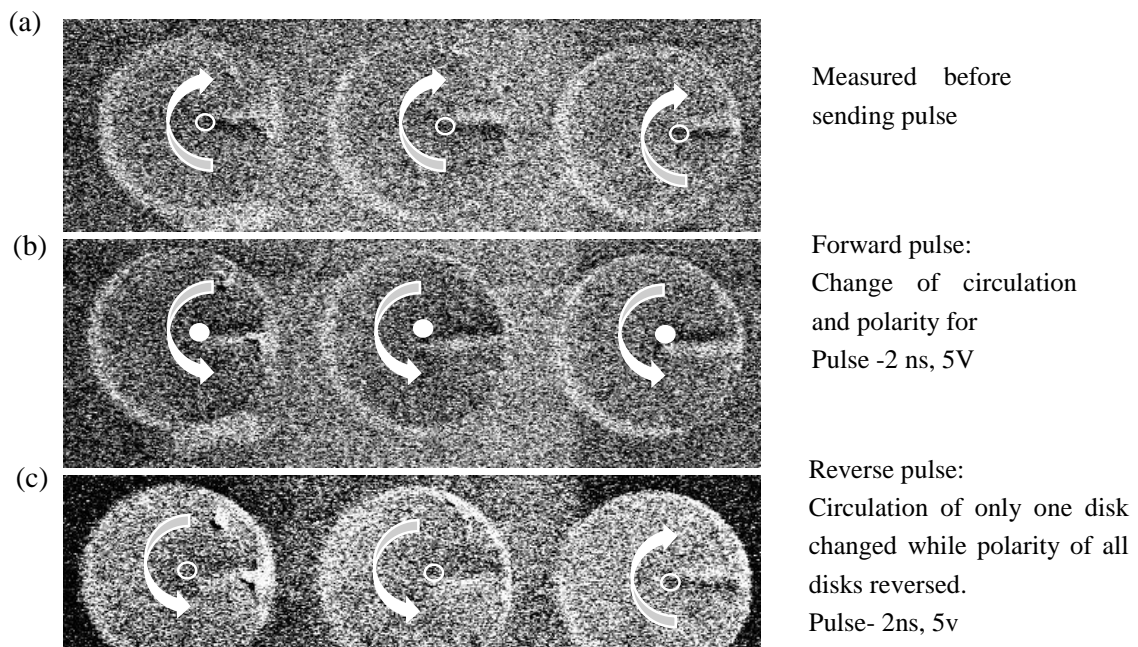


FIG 5.2. Circulation (white arrow) and polarity (white dot) in the disks. (a) The image was taken before sending a pulse. (b) Change of circulation and polarity after sending a pulse of 2 ns and 5 V. (c) Change of circulation back to the initial position in the last disk after sending a reverse pulse of 2 ns and 5 V, and the change of polarity in all disks. The arrows and circles are guides to the eye.

We performed a few experiments to check the pulse amplitude to switch the circulation and polarity in NiFe disks. Later, in August 2015, we got a timeslot at beamline 6.1.2 at the ALS synchrotron, Berkeley, to perform the dynamic measurements of the disks in the diameter range of 500 – 2000 nm and investigate nucleation and annihilation processes of disks up to 4- $\mu$ m diameter with thicknesses ranging from 20 nm to 100 nm.

## 5.2 Polarity control by PMA layer

The goal of the experiment was to determine whether the PMA layer is able to enforce the core polarity during vortex nucleation. We applied a static magnetic field higher than the annihilation field and observed the core polarity by MTXM at the ALS Synchrotron. Later, the PMA layer was also optimized by MFM in-house by sending repeated sequences of in-plane and out-of-plane field.

### 5.2.1 MTXM

Magnetic Transmission X-ray Microscopy was used for the time-resolved study of magnetization dynamics [247].

#### (a) Sample description

We used Si<sub>3</sub>N<sub>4</sub> membrane with a 5x5 mm<sup>2</sup> square frame and a 3x3 mm<sup>2</sup> wide and 200 nm thick central window for the MTXM measurement to ensure transparency of x-rays. The waveguide was exposed by e-beam lithography in the first step, and the disks were then exposed in the second step on the waveguide. For the MTXM measurement, the PMA layer was deposited on the disk with different compositions of Co and Pt. The composition of the PMA layer was Ta 5nm/Pt 5nm/4x (Co 1-1.2nm/Pt 1-1.2 nm)/Co 1-1.2 nm/ Pt 7 nm, followed by the deposition of Ni<sub>80</sub>Fe<sub>20</sub> (30-35 nm). The PMA layer deposition for MTXM measurement was done at the Center for Magnetic Recording Research, University of California, San Diego, while the NiFe deposition was done at BUT. At that time, the magnetron sputtering system in our laboratory was not available. In 2016 CEITEC received its Magnetron sputtering system, and then we started to optimize the PMA layer for further static and dynamic electric measurements. The samples with different compositions of the PMA layer along with the NiFe layer parameters are described in Table 5.2.

Table 5.2. Samples with different layer composition of PMA + NiFe used in MTXM measurements

No.	Layer composition	No. of samples
1.	Ta 5nm/Pt 5nm/4x(Co1 nm/Pt 1.2 nm)/NiFe 30 nm	5
2.	Ta 5nm/Pt 5nm/4x(Co1.2 nm/Pt 7 nm)/NiFe 35 nm	5

#### (b) Experimental setup

The field pulses were sent by the pulse generator to the sample and recorded in real-time on a 4 GHz oscilloscope. The sample was mounted on a unique sample holder tilted by 60° from the x-ray beam. With this orientation, it was possible to measure both in-plane and out-of-plane magnetization components. For the permalloy disk, the images were acquired at Fe L<sub>3</sub> edge at 706 eV. The images for the PMA layer were acquired at the Co L<sub>3</sub> edge at 777 eV when the sample was perpendicular to x-rays.

#### (c) Results

The MTXM experiment results are shown in Fig 5.3 at Fe edge and Fig 5.4 at Co edge.

The MTXM results show that the PMA layer was not stable enough. After applying the annihilation or bias field, there were multidomain configurations in both the permalloy and PMA layer. The behavior of the PMA layer should be out-of-plane with the field and used to impose the polarity. The above results can be summarized as:

- With the out-of-plane field by the external magnet, it got saturated in the perpendicular direction.
- Whenever an in-plane dynamic field was applied, a multidomain appeared in the PMA layer, which negatively influenced the neighboring permalloy layer.

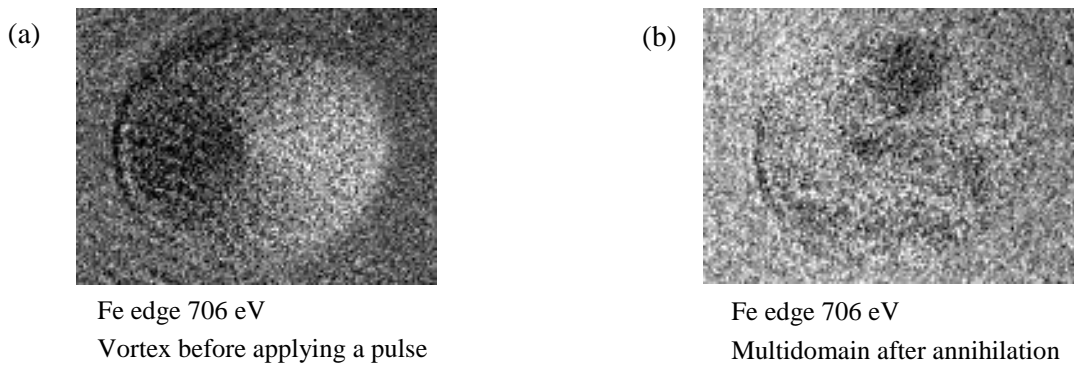


FIG 5.3 (a) MTXM image acquired before sending a pulse (b) Image acquired at a bias magnetic field. Both images were taken for a permalloy disk.

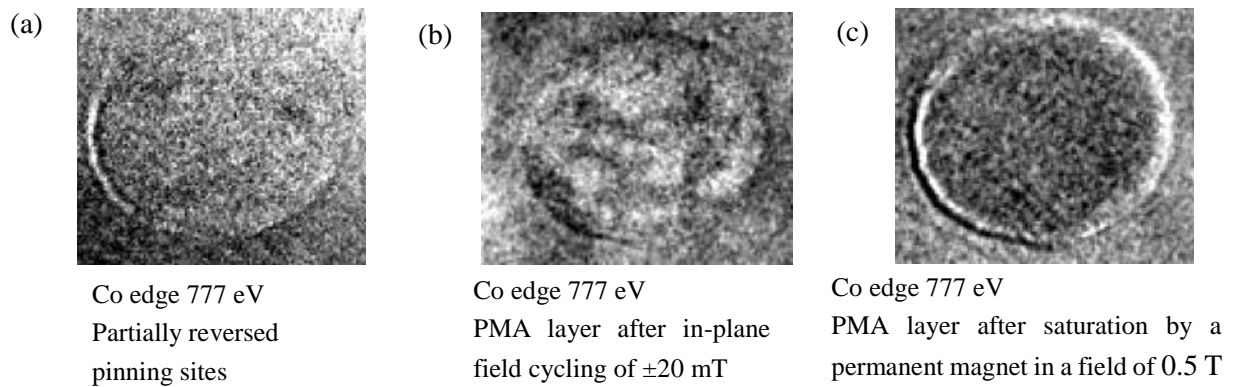


FIG 5.4. (a) MTXM Image of the PMA layer after applying the in-plane bias magnetic field. (b) PMA layer after in-plane cycling of a bias magnetic field. (c) Image of the PMA layer saturated by a permanent magnet.

It means that the PMA layer was not optimized enough to withstand the pulsed in-plane magnetic field. We decided to optimize the PMA layer to be more stable (i.e., magnetically harder) in applied in-plane magnetic fields.

#### (d) Other results – vortex nucleation

MTXM was also used to find out the details of spin configuration in each of the nucleation states. The magnetic vortex nucleation process in nanometer and micrometer magnetic disks undergoes several phases with distinct spin configurations called the nucleation states. Before the formation of the final vortex state, small submicron disks typically proceed through the so-called C-states while the larger



micron-sized disks proceed through, more complicated vortex-pair state or the buckling state. The observed process was further investigated and documented using micromagnetic simulations, Lorentz Transmission Electron Microscopy, and electrical transport measurements [89].

We used 2- $\mu\text{m}$ -wide and 100-nm-thick disks to study the nucleation process. We found out that the nucleated vortex state does not have a single vortex core, but instead, there are two vortex cores with an antivortex in between them, called the vortex-antivortex-vortex triplet (VAV triplet), as shown in Fig 5.5. The VAV triplet is stable in a range of a few mT, and upon the further decrease in the field, it annihilates into a single vortex core. Magnetic contrast at XM-1 is given by the x-ray magnetic circular dichroism (XMCD), which is sensitive to the magnetization component parallel to the incoming X-ray beam (out-of-plane magnetization in our geometry). The MTXM image of the VAV triplet in 2- $\mu\text{m}$ -wide and 100-nm-thick permalloy disk is shown in Fig. 5.5(a), together with the corresponding OOMMF simulation in Fig. 5.5(b). The simulated images in Fig 5.5(b) have the grayscale matched to the  $m_z$  component. The detail of the magnetization distribution in the VAV triplet is shown in Fig 5.5(c).

The VAV triplet is a highly confined spin structure and expected to exhibit eigenfrequencies in the GHz range. It can be suitable for spin-wave generation using a single magnetic element compared to the approach using antiferromagnetically coupled vortices as spin-wave emitters [8].

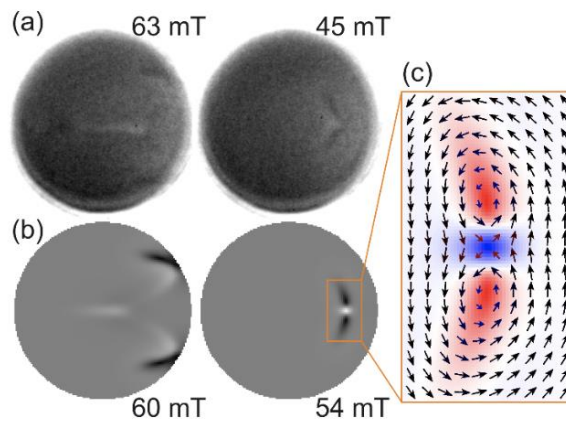


FIG 5.5 Detail of the VAV triplet nucleating from the buckling state in 2  $\mu\text{m}$  wide and 100 nm thick disk. (a) Out-of-plane magnetic patterns imaged by MTXM are compared to (b) the OOMMF simulations. (c) Detail of the simulated VAV triplet [89].

### 5.2.2 MFM

After the first experiments at ALS, it was evident that we need to prepare a more suitable PMA layer. The new PMA layer was then prepared in our Magnetron sputtering system and its properties tested using MFM and MOKE.

The AFM and MFM images of an array of 2  $\mu\text{m}$  disks, after applying the out-of-plane field and then sending the multiple pulse sequences of the in-plane magnetic field are shown in Fig. 5.6. The samples were also checked by the polar magneto-optical Kerr effect (MOKE).

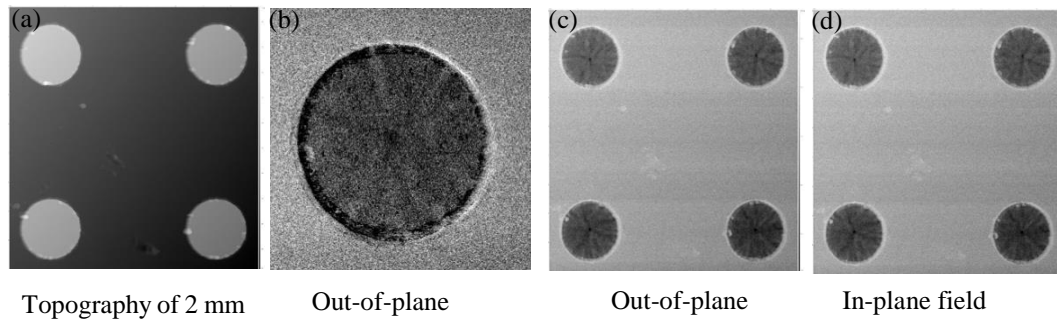


FIG 5.6 (a) Topographic image of an array of 2  $\mu\text{m}$  disks using AFM. (b) MFM image of a single 2  $\mu\text{m}$  PMA multilayer disk after sending the out-of-plane field to check the vortex core polarity. (c) MFM image of an array of 2  $\mu\text{m}$  PMA multilayered disks after sending out-of-plane field to average out the polarity direction. (d) MFM image of an array of 2  $\mu\text{m}$  PMA multilayered disks after sending the in-plane magnetic field sequences to check the stability of vortex core polarity against the in-plane magnetic field.

Fig 5.7(a) shows the SEM image of an array of 2  $\mu\text{m}$  disks with a 200-nm flat edge, and Fig 5.7(b) shows the MOKE graph of a 2  $\mu\text{m}$  disk.

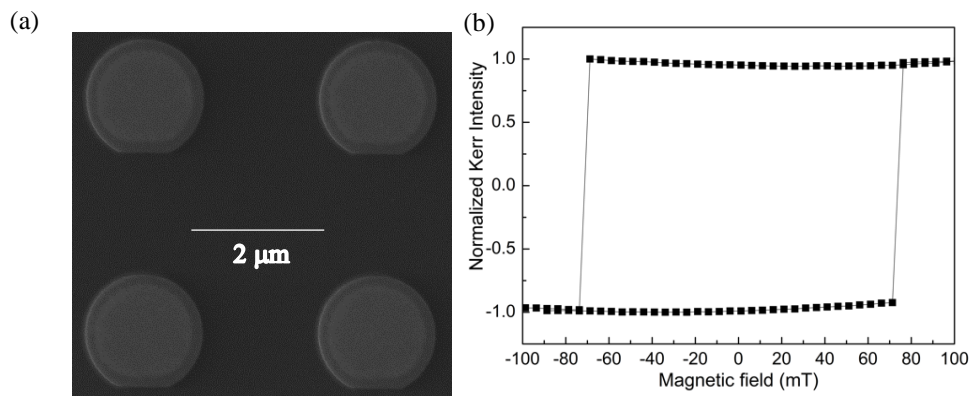


FIG. 5.7 (a) SEM image of an array of 2- $\mu\text{m}$ -wide disks with a 200-nm flat edge. (b) Polar MOKE measurement of a corresponding disk showing the coercive field of approx. 80 mT.

#### (a) Sample description

An array of 2- $\mu\text{m}$  disks with a thickness of 20-35 nm was fabricated by e-beam lithography and lift-off procedure on a Si wafer. For the polarity control, the disks were made of perpendicularly magnetized  $[\text{Co/Pt}]_n$  multilayer covered by the NiFe layer. The PMA and permalloy layers were sputter-deposited using a magnetron system.

For the multilayer stack, the first deposition was a 5-nm Ta base layer to provide better adhesion of the film on the substrate, followed by a 5-nm Pt interfacial layer and then the multilayer deposition of  $[\text{Co/Pt}]_n$ . All the depositions were done by magnetron sputtering at normal incidence at room temperature. The thickness of Co was 0.3 nm, and Pt 0.6 nm. For the Co thickness of 0.2-0.6 nm, the Co/Pt multilayers have strong perpendicular magnetic anisotropy, with the local magnetization oriented either parallel or anti-parallel to the film normal [248, 249]. The Co/Pt layers were successfully repeated



for the multilayer stacks, and the last Pt layer thickness was 1.2-nm-thick. The deposition was then followed by a 2-nm Ta spacer layer and then a NiFe layer on the top. The Co layer has a higher out-of-plane magnetic moment, and the Ta spacer layer was essential to balance the stray field from the bottom [Co/Pt]<sub>n</sub> multilayer with the top NiFe layer. The NiFe layer thickness was 22 nm. The thickness was calculated so that it will help to annihilate the vortex core at the boundary of the disk and will cause circulation switching [95]. The [Co/Pt]<sub>n</sub> multilayer was used to stabilize the vortex core polarity in the top NiFe layer against the external magnetic field and thermal disturbance.

### (b) Experimental setup

The stability of the top NiFe layer was checked by MFM after sending the repeated sequences of the in-plane magnetic field. The vortex core polarity was first set in one particular direction by the out-of-plane field. The repeated sequences of the in-plane magnetic field were sent, followed by checking the polarity by MFM, whether it changes or stays the same. The stability of polarity was tested for both field directions (up and down). The above technique was repeated for various samples, with an array of 2 μm disks, to confirm the stability of the vortex core polarity of PMA multilayered disk against the applied magnetic field.

### (c) Results

The SEM image of a D-shaped disk with Au electrodes is shown in Fig. 5.8(a), and Fig 5.8(b) shows the deposited multilayer stacks for the disk on the Si substrate. Fig 5.8(c) shows the magnetization vs. the applied field, the hysteresis loop of [Co/Pt]<sub>5</sub> multilayers measured by the vibrating sample magnetometer (VSM).

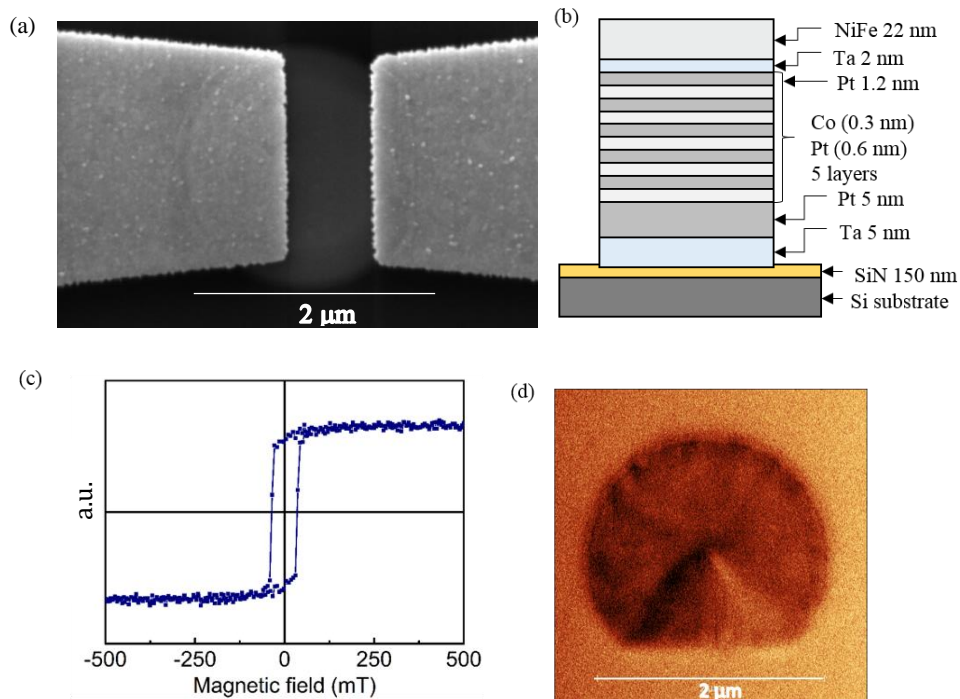


FIG.5.8 (a) SEM image of the sample. The disk is 2-μm-wide and connected with the Au electrodes on the top. The flat edge of the disk is 200 nm. (b) Multilayer stacks of the disk from bottom to top. The [Co/Pt] layers were repeated five times with the defined thickness. (c) MH curve of [Co/Pt]<sub>5</sub> multilayers. The graph shows the coercive field around 80 mT. (d) MFM image of the multilayer disk shows a white dot (polarity) at the center.

The out-of-plane coercive field value depends on the number of bilayer repeats and the thickness of each Co and Pt layers. The anisotropy value increases up to a certain number of bilayer repeats and then suddenly drops. This helps the tunability of the out-of-plane stray field of the  $[\text{Co/Pt}]_n$  multilayer needed to stabilize the vortex core polarity in the top NiFe layer. From the graph, the coercive field for the  $[\text{Co/Pt}]_5$  multilayers is nearly 80 mT, which is enough to provide stability against the vortex core stray field. These  $[\text{Co/Pt}]_5$  multilayers did not affect the in-plane magnetization behavior of the NiFe layer. Fig. 5.8 (d) shows the MFM image of a D-shaped 2- $\mu\text{m}$ -wide disk with the PMA layer and NiFe on the top.

### 5.3 Electric readout of vortex states

The readout of vortex states was carried out using a home-built electrical setup. We started with the measurement of static AMR to find out the circulation sense along with the vortex nucleation and annihilation fields. Then we performed dynamic AMR measurements to read-out the vortex states and selectively control the vortex states.

#### 5.3.1 Static AMR measurement

##### (a) Sample description

The samples for the static AMR measurement were fabricated by e-beam lithography and by lift-off. The permalloy disks with 2- $\mu\text{m}$  and 4- $\mu\text{m}$  diameter and a thickness of 30 nm were exposed on  $\text{Si}_3\text{N}_4$  in the first step, and then the Ta 5nm/Au 100 nm electrodes were exposed in the second step over the disk.

##### (b) Experimental setup

The wire-bonded sample was placed between the yokes of an electromagnet powered by the bipolar source Kepco BOP 20-5M (20V and 5A limits). The field was monitored by using a Hall probe located near the sample position. The magnetoresistance measurement required a sensitive measurement unit because the changes in the resistance were minimal, in order of  $10^{-3} \Omega$ . We used a Keithley 6221 current source and a 2182A nanovoltmeter, with 10 nV voltage measurement sensitivity. The probe current of 100-500  $\mu\text{A}$  was sufficient for measuring  $\sim 20\text{-}40 \Omega$  resistance with the precision of  $10^{-4} \Omega$ . The experiment was controlled by a computer using THAtec Innovation software using a GPIB connection. The electrical setup for the static AMR is shown in Fig 5.9.

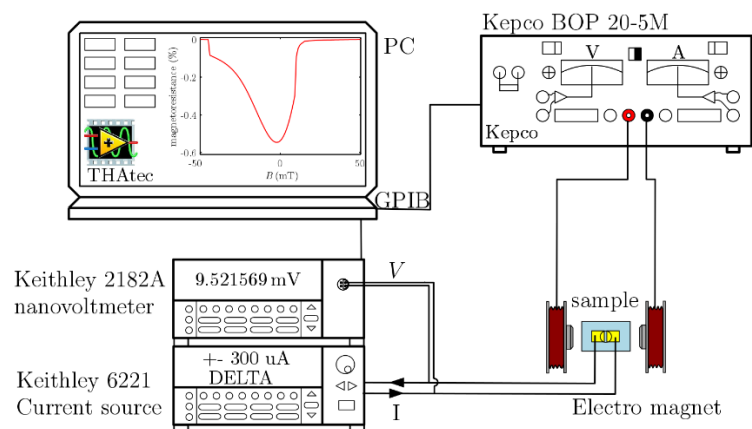


FIG. 5.9 Schematics of the static AMR experimental setup at room temperature. Kepco BOP 20-5M and Keithley 6221/2182A are connected to a computer via the GPIB interface, and the experiment is controlled with the THAtec Innovation software.

### (c) Results

The vortex nucleation proceeds through two mechanisms:

- C-state  $\rightarrow$  vortex, when there is no peak in AMR,
- C-state  $\rightarrow$  S-state  $\rightarrow$  vortex, when there is a peak present in the magnetoresistance curve.

Generally, nucleation through the S-state is common in larger disks, while in the smaller disks, vortices nucleate without any peak in the magnetoresistance curve through the C-state. We prepared ten samples of each 4- $\mu\text{m}$  and 2- $\mu\text{m}$  diameter disk, and the measurement graph for each sample is shown in Fig. 5.10(a) and Fig. 5.10(b), respectively.

The static AMR concept of circulation readout is based on the sign of the slope at zero field, where the vortex core is moving either towards the contacts or away from them. The graph also explains the annihilation field value and the asymmetric core displacement around the zero-external field.

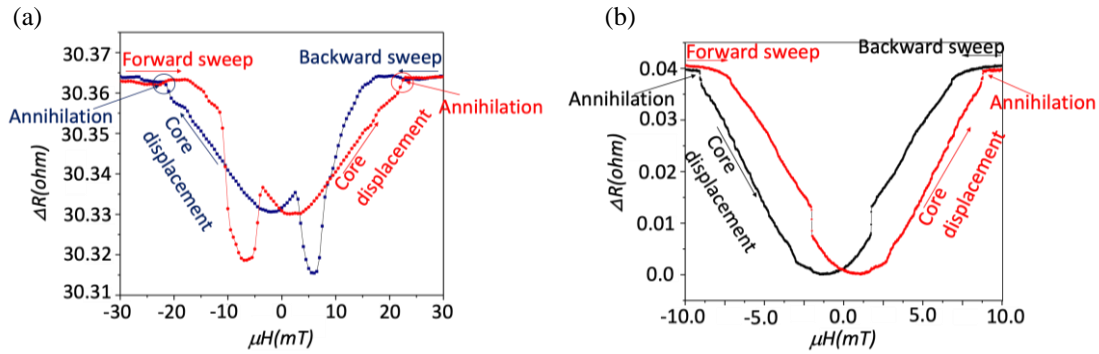


FIG 5.10 (a) AMR graphs for a 4  $\mu\text{m}$  disk under a DC of 100  $\mu\text{A}$  in a field sweep from -30 to 30 mT and represent the nucleation through the S-state. (b) AMR graphs for a 2  $\mu\text{m}$  disk show nucleation through the C-state without any peak in the AMR.

### 5.3.2 Dynamic AMR measurement

In the dynamic AMR measurement, the readout of vortex states was done fully electrically. When the electric current is injected into the ferromagnetic disk, it excites the gyrotropic motion of the vortex core, which leads to oscillation in resistance. It is further mixed with the input rf current to generate a measurable rectified dc voltage. These rectified spectra can precisely detect vortex dynamics. The electrical resistance from the AMR effect decreases with the movement of the vortex core in the direction of the current. In contrast, it increases with the movement of the vortex core in the direction perpendicular to the current. The alignment of the magnetization by the effect of current is shown in Fig 5.11.

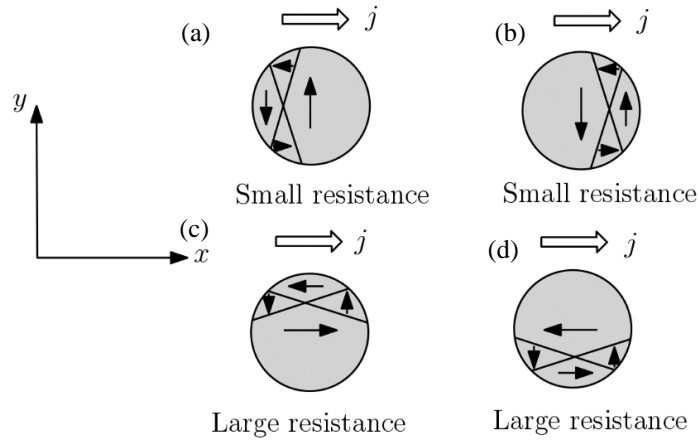


FIG 5.11 Schematic images of the magnetization in the disk and electric current. The resistance in (a) and (b) are smaller than those in (c) and (d) [194].

#### (a) Sample and experimental setup

For the dynamic AMR measurement, a 2- $\mu\text{m}$  disk pattern with a 200-nm flat edge (D-shaped) was exposed on the Si wafer in the first step. The disk was then deposited by a PMA+ NiFe metallic layer. In the second lithography step, electrodes were exposed to the disk. The electrodes were then used to excite and measure the disk at the same time. The entire structure was fabricated on 250 nm thick  $\text{Si}_3\text{N}_4$  deposited over Si wafer to prevent current leakage. The samples were prepared by e-beam lithography and by the lift-off procedure.

For electrical measurements, the samples were wire-bonded to a custom-designed PCB operating at frequencies up to 16 GHz. The electrical setup is shown in Fig 5.12. The PCB was mounted and rotated in between the poles of an electromagnet. The sample was rotated so that the field could be applied parallel and perpendicular to the electrodes.

Two different current sources were used. The AVTECH pulse generator (AVM-4-b) was used for sending the current pulses, and the ROHDE & SCHWARZ SMC100A signal generator (9KHz - 1.1GHz) was used for sending the continuous rf signal for the induction of the rectified dc voltage spectrum in the frequency range of 50 MHz – 200MHz. Keithley 2182A nanovoltmeter was used to detect a small change of voltage with 10-nV voltage measurement sensitivity, and the bipolar current source Kepco BOP 20-5M was used for powering the electromagnet. The magnetic field was calibrated using a tesla meter F.W.Bell 6010.

The current pulses were first sent to the sample using the AVTECH pulser, and then the sample was connected to the measurement setup, where the continuous RF signal was sent to the Bias-tee. The input rf port of the bias-tee was connected to the ROHDE & SCHWARZ signal generator for the continuous rf signal. The voltage and the ground port were connected to the Keithley voltmeter to measure the voltage change in the sample, while the output of Bias-Tee was connected to the sample for sending the rf + dc signal to the sample. The ramping of the external magnetic field through the sample was done by the Kepco power supply and precisely measured by the tesla meter.

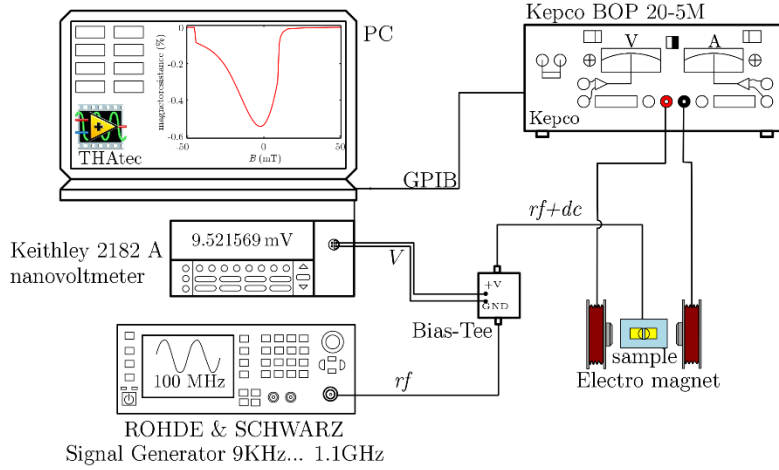


FIG. 5.12 Electrical setup for the dynamic AMR measurement. A signal generator was used to send out the continuous signal for readout, whereas a pulse generator was used to send out the pulses for vortex states' writing. The magnetic field was applied to the sample in-plane and out-of-plane to the electrodes and disk. Kepco, Keithley, and ROHDE & SCHWARZ are connected to a computer via the GPIB interface, and the experiment is controlled with the THAtec Innovation software.

The experiment was controlled by a computer using the THAtec Innovation software using a GPIB connection.

The parameters used during the experiments are written in Table 5.3.

Physical quantity	Symbols	Value
Disk radius	$r$	1 $\mu\text{m}$
Thickness	$L$	39 nm
Electrical resistance	$R$	$\sim 40 \Omega$
Power	$W$	$4.0 \times 10^{-5} \text{ W}$ (-14 dBm)
Resonant frequency	$\omega_Y / 2\pi$	90 MHz
Electrode shift (x-axis)	$x_R$	300 nm
Frequency range	$f$	50-200 MHz

## (b) Results

### (i) Polarity readout

The sample in between the yokes of an electromagnet was placed such that the external static field was applied in the plane of electrodes ( $\theta = 0^\circ$ ), and the field varied in the range of +4 mT to -4 mT. A sinusoidal continuous-wave rf current with a power of  $4.0 \times 10^{-5} \text{ W}$  (-14 dBm) was applied to the disk in the frequency range from 50 MHz to 200 MHz. The measurements were always performed from lower to a higher frequency. The polarity readout technique is already described in chapter 3, in section 3.5.

The electrical measurement graphs for a 2- $\mu\text{m}$  disk at 2-mT applied field are shown in Fig 5.13. Fig 5.13 (a) shows the result of up polarity ( $p = +1$ ), as the voltage peak is positive for a magnetic field of 2 mT, and the voltage peak is negative in the field of -2 mT. Figure 5.13 (b) shows down polarity

( $p = -1$ ), because the voltage peaks are reversed with respect to the previous case. The graphs nicely show the up and down polarity of a vortex core, as explained in section 3.8. The measured voltage peaks are shifted because the chopped disk geometry leads to an asymmetric orbit.

Fig 5.14 shows the external field dependence of the rectifying voltage spectra at the angle of  $\varnothing = 0^\circ$  for up polarity ( $p = +1$ ) and down polarity ( $p = -1$ ) of the vortex core. Above  $\mu_0 H_x = 0$  mT, the spectra for  $p = +1$  are convex upward, whereas the spectra for  $p = -1$  are convex downward. In contrast, below  $\mu_0 H_x = -1$  mT, the spectra for  $p = +1$  are convex downward, whereas the spectra for  $p = -1$  are convex upward.

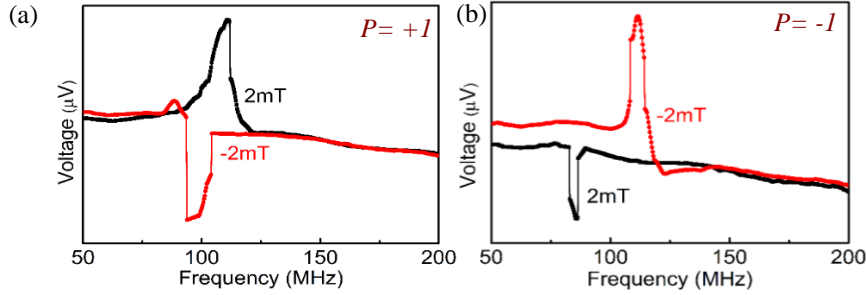


FIG. 5.13 (a) Experimental voltage peaks for up polarity ( $p = +1$ ) at 2 mT and -2 mT. (b) Voltage peaks for down polarity ( $p = -1$ ), as the voltage peaks just reversed at 2 mT and -2 mT external field.

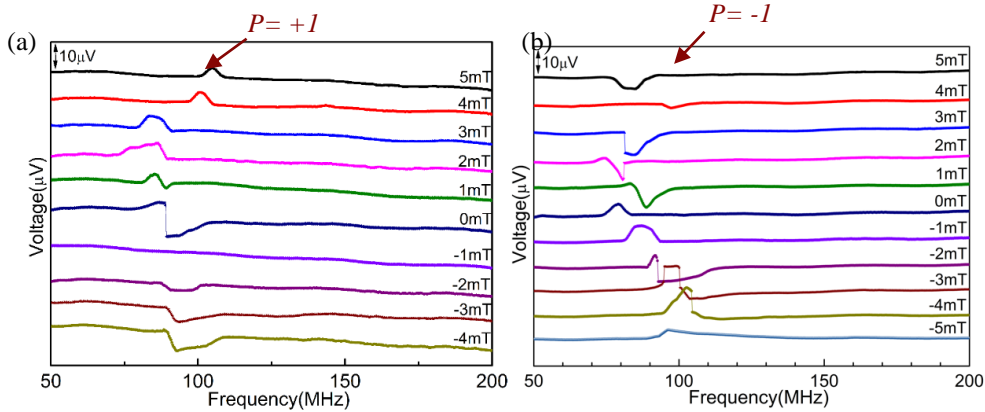


FIG 5.14 (a) Rectified voltage spectra for up polarity ( $p = +1$ ) over an external field range of 5 mT to -4 mT. (b) Rectified voltage spectra for down polarity ( $p = -1$ ) over an external field range of 4 mT to -4 mT.

### (ii) Circulation readout

For the circulation readout, the sample in between the yokes of the electromagnet was rotated by  $90^\circ$  around the  $x$ -axis. Where the external static field was applied at  $90^\circ$  to the electrodes, and the vortex core is displaced either under the Au electrodes or away from the electrodes, as described previously in chapter 3, Fig 3.9.

We applied a positive external field of magnitude 2 mT to the samples, which displaced the vortex core in between the gap of the electrodes and returned a voltage peak. The peak corresponds to the clockwise circulation as previously defined and experimentally demonstrated in Fig 5.15 (a). While keeping the same circulation, when the -2 mT field is applied, the vortex core moves under the Au electrode, and the voltage peak vanishes. While preserving the counterclockwise circulation and the external field is

varied from +ve field to -ve field, the voltage spectrum shape reversed with the applied field, as in Fig 5.15 (b).

Fig 5.16 shows the experimental graph of the external field dependence of rectifying voltage spectra at an angle of  $\theta = 90^\circ$  for clockwise ( $c = +1$ ) and counterclockwise circulation ( $c = -1$ ). We were only able to detect the resonant signal from the vortex gyration above the field  $\mu_0 H_x = 0 \text{ mT}$ , as shown in Fig 5.16 (a). In contrast, the resonant signal was only observed below the field  $\mu_0 H_x = -1 \text{ mT}$ , as shown in Fig 5.16 (b).

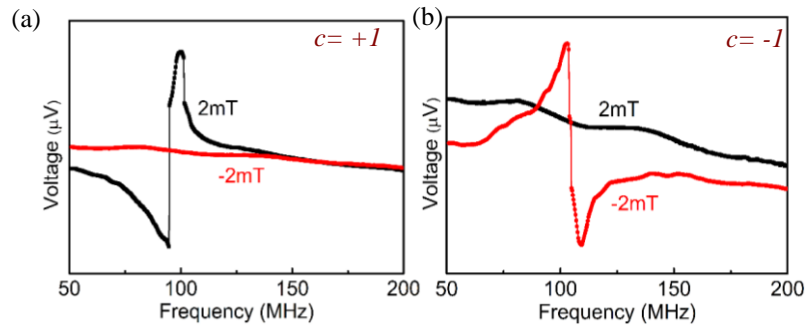


FIG 5.15 (a) Experimental voltage peaks for clockwise ( $c = +1$ ) circulation at 2 mT and -2 mT. (b) Experimental voltage peaks for counterclockwise ( $c = -1$ ) circulation at 2 mT and -2 mT.

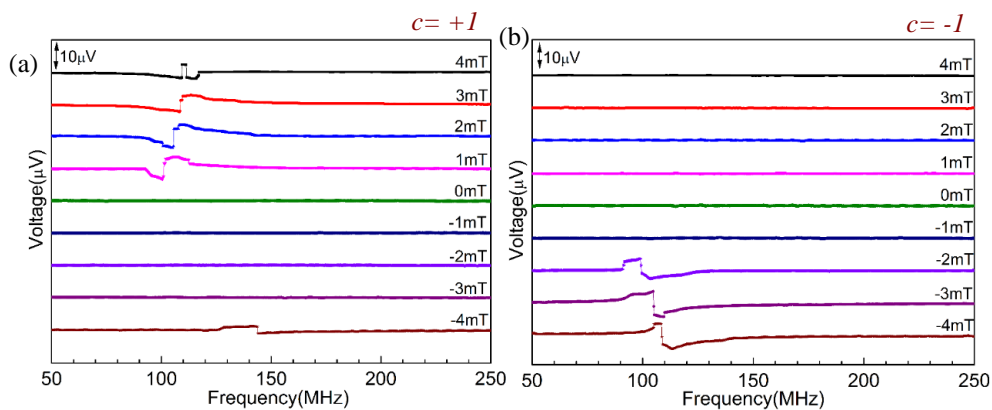


FIG 5.16 (a) Rectified voltage spectra for clockwise circulation ( $c = +1$ ) over an external field range of 4 mT to -4 mT. (b) Rectified voltage spectra for counterclockwise circulation ( $c = -1$ ) over an external field range of 4 mT to -4 mT.

#### 5.4 All electric control (switching and readout) of vortex states

The selective switching of a magnetic vortex state includes combining the electric writing of a particular state and the readout of that state. The PMA layer was used to define the vortex polarity, and a picosecond current pulse was sent to switch it to the required state eventually. After polarity switching, the circulation was also verified to check if the polarity switching affected the sense of circulation. A nanosecond current pulse was used to switch the circulation, while the D-shaped disk defined the sense of circulation.

### 5.4.1 Polarity control and switching

The switching of vortex core polarity [152, 250] has been previously studied by applying the spin-polarized current [154], resonant excitation induced by the A.C magnetic field [44, 139, 148] and by pulse-field [48, 160] or current [156].

We used a short and high amplitude (picosecond) current pulse for the polarity switching. When the picosecond current pulse is applied, the vortex core starts gyrating around its equilibrium point, and the core polarity switches, before reaching the disk boundary. This happens because the current pulse is strong enough to quickly drive the core above the critical velocity, which is several hundreds of m/s. Whenever a current pulse for circulation switching was sent to the disk, the [Co/Pt]<sub>5</sub> multilayers keeps the previously imposed vortex core polarity upon nucleation. So, the combination of a picosecond current pulse and a [Co/Pt]<sub>5</sub> multilayer provides the selective switching of vortex core polarity.

The current pulse used for the polarity switching is shown in Fig 5.17 (a), and Fig 5.17 (b) shows the current pulse used for the circulation switching measured at an oscilloscope with a 20 dB attenuator. The AVTECH pulse generator was used for sending the current pulses to the samples.

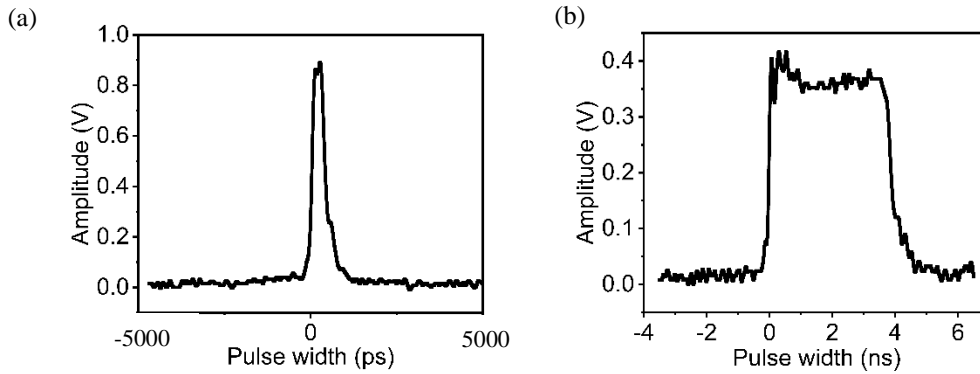


FIG. 5.17 (a) High-amplitude picosecond current pulse for polarity switching measured using an oscilloscope with a 20 dB attenuator. (b) Low-amplitude nanosecond current pulse for circulation switching.

Fig 5.18 (a) and (c) are the voltage spectra defining polarity and circulation of a sample before applying any kind of current pulse. Simultaneously, (b) and (d) show the polarity and circulation after sending the current pulse for polarity switching. The graphs show, when a polarity switching (picosecond) current pulse was applied to the sample, it would switch or affect only the polarity. In contrast, it would not affect the sense of circulation. The graphs are measured over a range of external fields to verify the effect of current pulses.



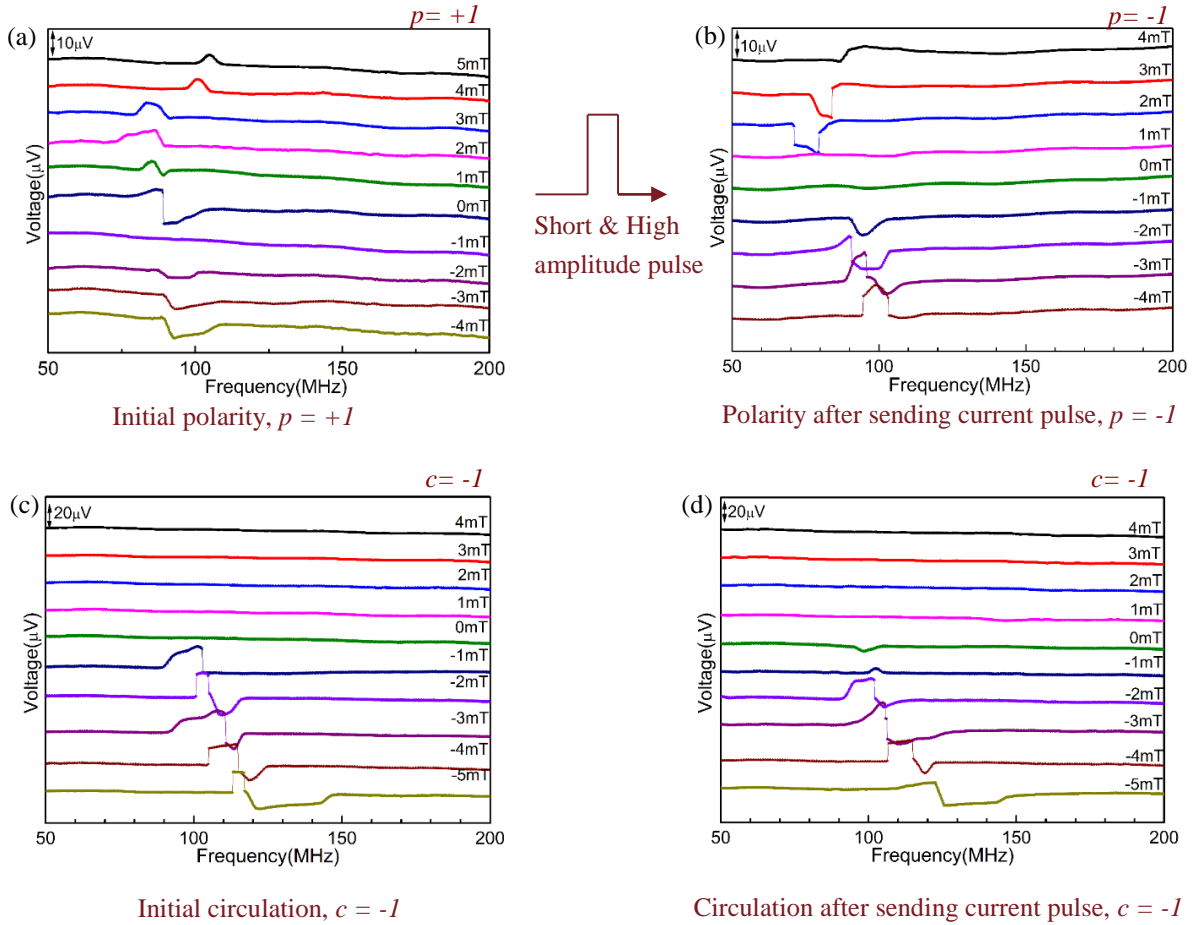


FIG 5.18 (a) Voltage spectra corresponding to the vortex polarity before sending any current pulses. (b) Voltage spectra corresponding to the switched polarity after sending the current pulse. (c) Voltage spectra corresponding to the initial circulation of the same sample before sending any current pulse. (d) Voltage spectra corresponding to the circulation of the sample after sending the current pulse for polarity switching. All the measurements were done at the power of -12 dBm.

#### 5.4.2 Circulation control and switching

The circulation control has been previously studied either using the thickness modulation [45, 251] or by the shape asymmetry [43, 102, 103, 252–257]. The switching of spin circulation is induced by either applying a static in-plane magnetic field [92] or using a magnetic field pulse [45, 95, 169–171]. The magnetic field is required to expel the vortex core to the disk boundary and then form a new vortex with the opposite sense of circulation.

We used shape anisotropy (D-shaped disk) for circulation control, as shown in Fig 5.8 (a). The 2- $\mu\text{m}$  disk was chopped on one side by 200 nm to make the flat edge on one side of the disk. The flat edge of the disk enabled the control of the vortex circulation after the saturation when the applied field was reduced to zero. The resulting sense of circulation is either CW or CCW. The flat edge provides the vortex core's preferential nucleation region, as the demagnetizing field is more significant at the flat edge side than the round edge when the external field was applied parallel to the flat edge side.

For the circulation switching, we used nanosecond low-amplitude current pulses, as shown in Fig 5.17 (b). Whenever the nanosecond current pulse was applied to the disk, it moved the vortex core to the

disk boundary without reaching the critical velocity, thus preventing the polarity switching and providing only the circulation switching, preferably along the flat edge.

During the static displacement of the vortex core, both the flat and round edge were repulsive towards the core, which means, when the vortex core was under gyrotropic motion near the flat edge, it felt a sharply reduced dynamic stiffness. As a result, the net dynamic core stiffness was reduced, leading to a lower gyrotropic frequency at a flat edge than the round edge. By this means, the gyrotropic frequency was sharply decreased (by displacing the vortex core near the flat edge) or increased (by shifting the vortex core towards the round edge) [133, 167].

Fig 5.19 (a) and (c) are the corresponding circulation and polarity of a vortex before sending any current pulse. Simultaneously, (b) and (d) graphs show the circulation and polarity after sending the current pulse for circulation switching. So, when a current pulse is applied to the sample to switch the circulation, it should affect only the circulation, not the polarity. Indeed, Fig 5.18 and Fig 5.19 show the switching of polarity and circulation individually and independently.

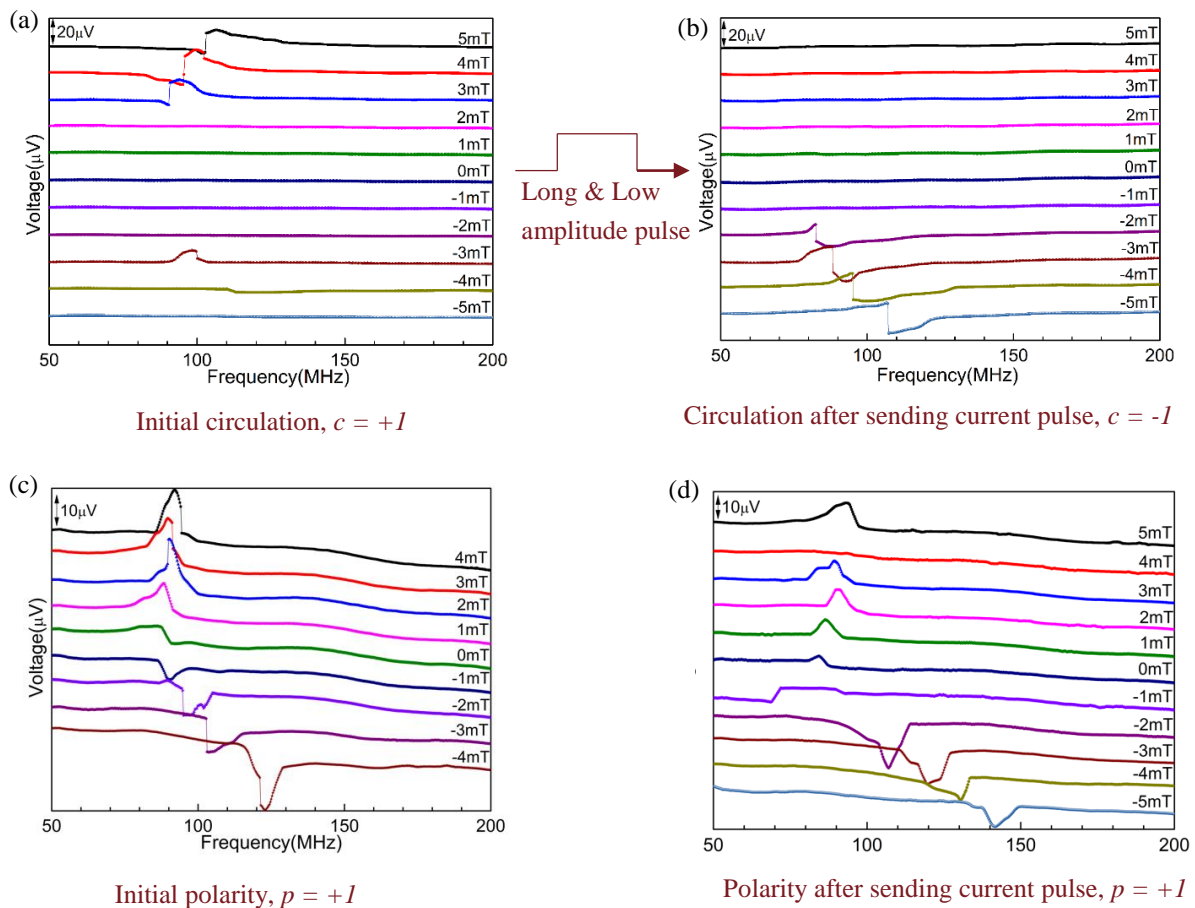


FIG 5.19 (a) Initial circulation of a vortex before sending any current pulses. (b) Circulation after sending the current pulse to switch the circulation. (c) Polarity of the same sample before sending any current pulse. (d) Polarity of the vortex after sending the current pulse for circulation switching. (c) and (d) show that the circulation switching pulse did not affect the polarity.







These two different kinds (picosecond and nanosecond) of current pulses can have both positive and negative amplitude, based on the specific vortex state.

### 5.4.3 Full control (The combination of pulses)

The vortex can only be switched to the desired state by sending a defined pulse sequence, even without reading the circulation and polarity previously. It is described in table 5.4, where the magnetization is imprinted in one direction in the PMA layer, let's say up, which will support the up polarity ( $p = +1$ ) of the vortex, until it will be switched in the other direction by a subsequent current pulse. The first state ( $p = 1, c = -1$ ) can be obtained by sending the nanosecond current pulse, which will ensure to have the counterclockwise ( $c = -1$ ) state. In contrast, the polarity ( $p = 1$ ) is supported by the up orientation of the PMA layer. The second state ( $p = 1, c = 1$ ) can be obtained by the same kind of nanosecond current pulse but with a negative amplitude. The third state ( $p = -1, c = 1$ ) in a magnetic vortex can be introduced by sending both picosecond and nanosecond current pulses to the magnetic disk. The long and low negative amplitude current pulse was sent to specify the clockwise circulation with the help of a flat edge of the disk.

In contrast, the short and high negative amplitude current pulse was sent to define the vortex core's down polarity. Both pulses can be sent one after another because one is not affected by the other. On the contrary, the fourth state of the magnetic vortex ( $p = -1, c = -1$ ) can be defined by the same kind of current pulses with a positive amplitude.

Table 5.4. The four configurations of a vortex that can be obtained by the combination of different current pulses.

No.	P	C	Pulse 1	Pulse 2	Comment
1.	1	-1			Long and low amplitude pulse for circulation switching
2.	1	1			Long and low amplitude (negative) pulse for circulation switching
3.	-1	1			Long and low amplitude (negative) pulse for circulation switching + Short and high amplitude pulse for polarity switching
4.	-1	-1			Long and low amplitude pulse for circulation switching + Short and high amplitude pulse for polarity switching

#### (a) Sample description and experimental setup

For the full control of vortex states measurement, the entire structure was fabricated on 100-300 nm thick  $\text{Si}_3\text{N}_4$  deposited over Si wafer to prevent any current leakage. The samples were prepared by e-beam lithography and by lift-off procedure.

The experimental setup for the measurement of full control of vortex states is the same as dynamic AMR measurement and shown in Fig. 5.20 (a), and Fig. 5.20 (b) shows the external magnetic field configuration for the polarity readout, while Fig. 5.20 (c) shows the external magnetic field configuration for circulation readout.

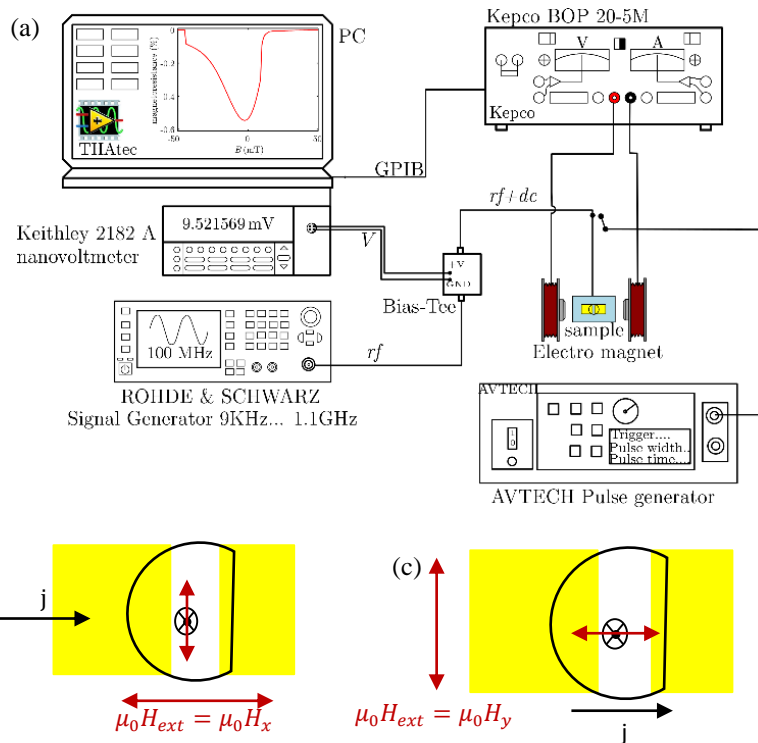


FIG. 5.20 Electrical setup for the dynamic AMR measurement. A signal generator was used to send out the continuous signal for readout, whereas a pulse generator was used to send out the pulses for the writing of vortex states. The magnetic field was applied to the sample in-plane and out-of-plane to the electrodes and disk. Kepeco, Keithley, ROHDE & SCHWARZ, and AVTECH are connected to a computer via the GPIB interface, and the experiment is controlled with the THAtec Innovation software. (b) Define the external magnetic field direction for polarity readout. (c) Define the external magnetic field direction for circulation readout.

### (b) Results

Fig 5.21 shows the various current pulses used for selective switching with the corresponding states.

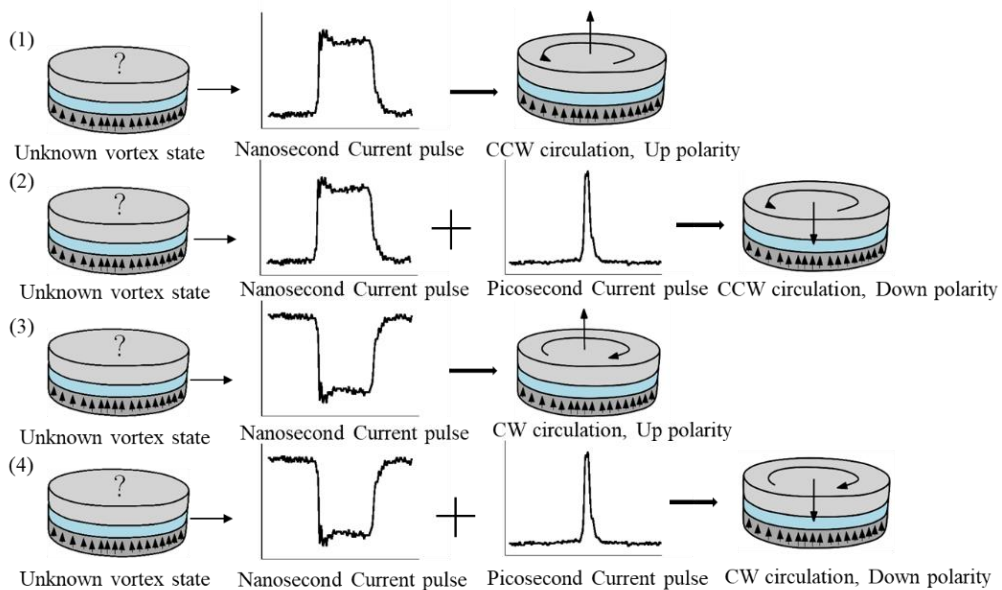


FIG 5.21 Pulses used to switch the particular vortex states selectively. The applied pulse amplitude was both positive and negative for switching the vortex states.

The four possible configurations of a magnetic vortex are shown in Fig 5.22. All the above graphs were measured at an rf power of -14 dBm, at an external field of 2 mT and -2 mT. The polarity graphs were measured with the external field in-plane of electrodes, and the circulation graphs were measured with the external field at 90° to the electrodes, as shown in Fig 5.22 (a) and (b), respectively.

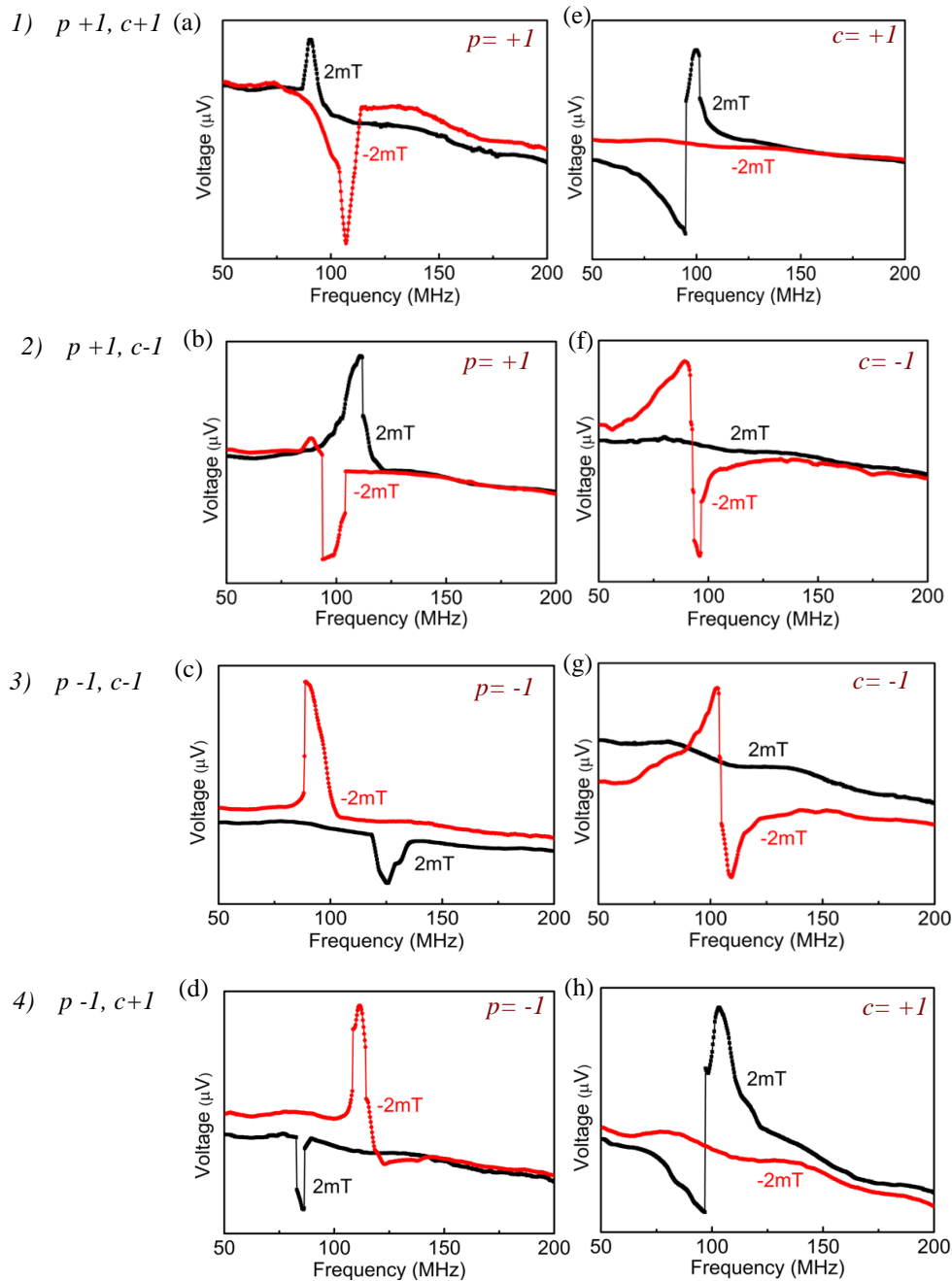


FIG 5.22 (a)-(d) Effect of external static field direction on the polarity measurements. (f)-(h) Effect of external static field direction on the circulation measurements.

### 5.5 Reliability of vortex states switching

The switching probability as a function of voltage and pulse duration is shown in Fig 5.23. The switching probability can be described as the ratio of the number of times switching to the total number of attempts. The switching probability was determined experimentally for the particular values of

voltage and current pulses. Fig 5.23 (a) shows the switching probability for vortex core polarity. The maximum switching probability (100%) is obtained at a pulse duration of 525 ps and 9.85 V. At the same time, the measurements for switching were performed at a pulse duration of 400 – 550 ps and 9.7 – 9.95 V. So, from the graph, we showed the measured switching probability range. Fig 5.23 (b) shows the switching probability range for circulation. The highest switching probability (100%) for circulation happens at 3.2 ns and 4.8 V, while the measured switching probability range varies in the region of 1 – 4.4 ns pulse duration and 4.6 – 5 V.

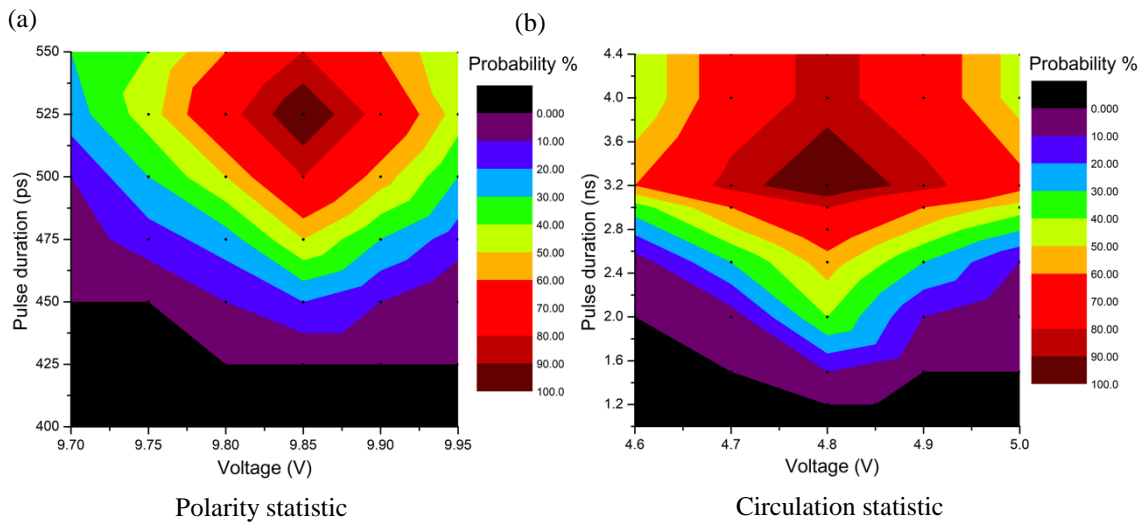


FIG 5.23 (a) Switching probability statistics for polarity switching as a function of pulse duration and voltage. The maximum switching happens at 525 ps, and 9.85 V. (b) Switching probability for circulation switching. The highest switching probability is around 3.2 ns and 4.8 V.

So, from the graphs, we are experimentally able to define the highest switching probability range for both circulation and polarity. We also show that, by a single current pulse, we can switch the circulation and polarity. Simultaneously, we can control them by shape asymmetry and the  $[\text{Co/Pt}]_n$  multilayer, respectively. Thus, we can selectively switch both circulation and polarity.

## 5.6 Resonance frequency splitting

The rf signal used for the readout of the vortex state had a lower amplitude compared to the one used for the writing of vortex states so that the rf signal does not affect the readout signal. The amplitude of the readout signal was -14 to -11 dBm (85-120 mV), which is quite low compared to the 3-5 V for circulation switching current pulses and 9.6-10 V for polarity switching current pulses. As the amplitude of the readout signal started increasing from -10 to -8 dBm, the dc voltage spectrum signal started splitting. Fig 5.24 (a) shows the circulation graph at -12 dBm, with clockwise circulation ( $c = +1$ ). The voltage peak at -12 dBm does not show any sign of frequency splitting while going towards higher amplitude at -10 dBm, the voltage signal started splitting and even started showing the signal in the negative field. According to the dc voltage equation of circulation readout, for clockwise circulation, it should show the signal only in the positive field, when the vortex core was in between the electrodes. There should not be any signal if the vortex core were displaced under the electrodes. The frequency splitting and signal in the positive field were the effects of higher rf power; the theory about frequency splitting and signal loss at higher power was already described in section 2.3.3(d) [134, 258].

Similarly, in Fig 5.24 (d), the voltage signal at -12 dBm shows a clear voltage peak in different field values. The spectrum shows down polarity ( $p = +1$ ). As the rf power starts increasing, the false signal peak and frequency splitting start occurring. At even higher rf power up to -8 dBm, the voltage signal loss starts happening, while the signal peak can be reversed back at a lower rf power from -14 dBm to -12 dBm. This effect needs to be taken into account when interpreting the AMR spectra of vortex dynamics.

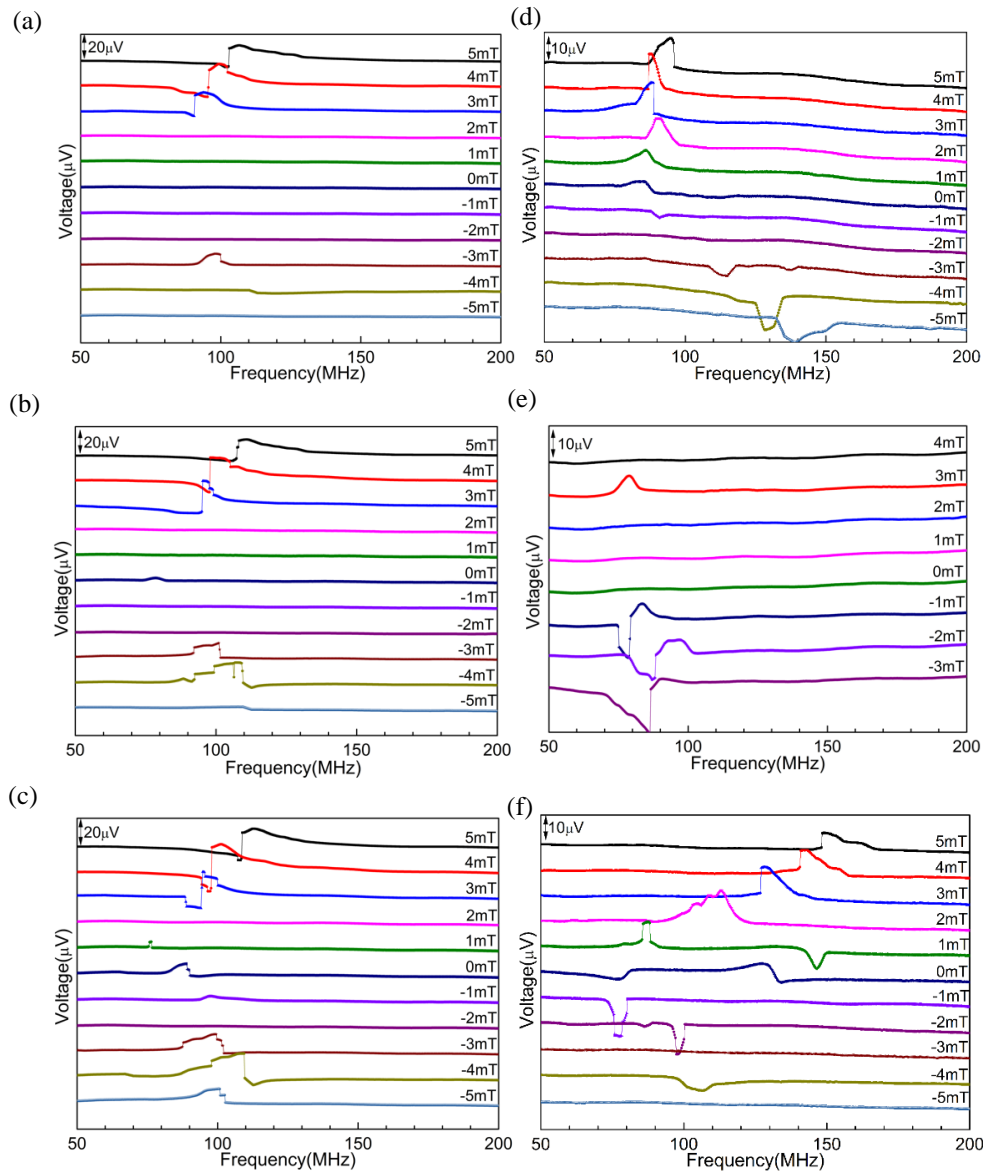


FIG 5.24 (a)-(c) Circulation spectra at the power from -12 dBm to -8 dBm. (d)-(f) Polarity spectra at the power from -12 dBm to -8 dBm.



## 6. Conclusion

In this thesis, we studied the dynamics of a magnetic vortex by electrical measurements, which, unlike other laboratory-based techniques, provide a means for efficient switching and readout of all four vortex configurations. A significant part of the thesis was devoted to develop the setup for all-electric switching and readout of the vortex states. The readout measurement is primarily based on the anisotropic magnetoresistance effect. For this purpose, we have designed samples that were lithographically prepared by a combination of e-beam lithography and the lift-off technique.

The main goal of the thesis was to perform the selective switching of a magnetic vortex into the desired vortex state. It includes selective switching of both vortex circulation and polarity on a nanosecond or picosecond time scale, respectively. Until now, experiments reported in the literature presented switching of a single vortex characteristic, circulation or polarity, not fully selective switching. During the course of this thesis, Shimon et al. presented magnetic field control of both states, using magnetic force microscopy for the readout of the vortex states, and Goto et al. presented the electric readout of vortex states. However, full electric readout and writing of vortex states have been missing. Besides obtaining robust statistics of the switching efficiency, such an approach allows integration into a single device, which has a higher significance for the application of magnetic vortices in electronics.

Regarding the write/read process, we have developed and optimized the following procedure. In case vortex circulation switching is not required, the polarity can be toggle switched by a sub-nanosecond field pulse (525 ps, 9.85 V for 2- $\mu$ m-wide and 36-nm-thick disks).

Vortex circulation switching requires the annihilation of the vortex by a field or current pulse and nucleation of a vortex with the specified circulation. Initially, the quasi-static nucleation and annihilation fields for a specific disk were determined by the static AMR measurements. Subsequently, a low-amplitude 3.2 ns, 4.8 V field pulse was used to annihilate the initial vortex state. The vortex nucleation proceeds through a C-state defined by an asymmetrically shaped disk, which provides the final sense of circulation during the nucleation process. During the annihilation process, the vortex polarity information is lost. However, it can be deterministically imposed by a PMA layer in the magnetic multilayer stack. The magnetic configuration of the PMA layer breaks up into a multidomain structure for disks larger than 3-4  $\mu$ m. Therefore, we selected a diameter range of 1-2  $\mu$ m to ensure the magnetization around the disk edge is always aligned in one direction perpendicularly to the surface. If needed, the polarity can be then toggle-switched to the opposite orientation. Lastly, the dynamic AMR measurements were performed to verify the final vortex state.

So, the combination of the PMA layer with a fast and high-amplitude field pulse can be used for the polarity control, and the geometrical asymmetry of the disk along with a low-amplitude nanosecond field pulse can be used for circulation control. These conditions provide maximum switching efficiency.

The statistical study shows that the maximum switching (100 %) probability for the polarity occurs at a pulse parameter of 525 ps  $\pm$  1%, and 9.85 V, while for circulation, the 100 % switching happens at the pulse parameters of 3.25 ns and 4.8 V. So, from the statistic, we can define the range of most



switching probability events for both circulation and polarity. The statistic study also provides the reliability of the device.

Chapter 5 describes all the acquired results during all measurements and shows the type of pulses used for writing a particular state, and shows the statistic study for polarity and circulation. In appendix A, we show all the possible combinations of a vortex state, and in appendix B, we have listed the samples used during our measurements.

The future perspective of the study can be extended to different geometrical shapes and other material for a longer life and to the smaller structures (in the sub-nanometer range) to improve the density of the device. The study can also be done over a range of temperatures from  $-40^{\circ}\text{C}$  to  $125^{\circ}\text{C}$ , and the study further can be extended to the STT-MRAM with MTJ. Currently, there are low storage MRAM available, but the research is still going on to improve the storage and better speed. The other applications include logic circuits, radio-frequency devices, and sensors.

# Appendix A

The vortex states switching from one kind of vortex state to another gives twelve different combinations of states, which will further confirm the role of both types of the current pulse in the switching of vortex states.

Fig A.1(a) has three different states switching from the original state ( $c\ 1, p\ 1$ ). In the first state, a picosecond current pulse was sent to switch the polarity from ( $p\ 1 \rightarrow p\ -1$ ) state. The switching of states is shown with electrical measurement graphs. The measurements were done over an external field range of ( $+5\ mT$  to  $-5\ mT$ ). The second state includes switching from ( $c\ 1, p\ 1 \rightarrow c\ -1, p\ 1$ ) states, which needs only to switch the circulation by nanosecond current pulse, and the polarity can stay the same. Whereas in the third state, both ( $c\ 1, p\ 1 \rightarrow c\ -1, p\ -1$ ) circulation and polarity need to be switched.

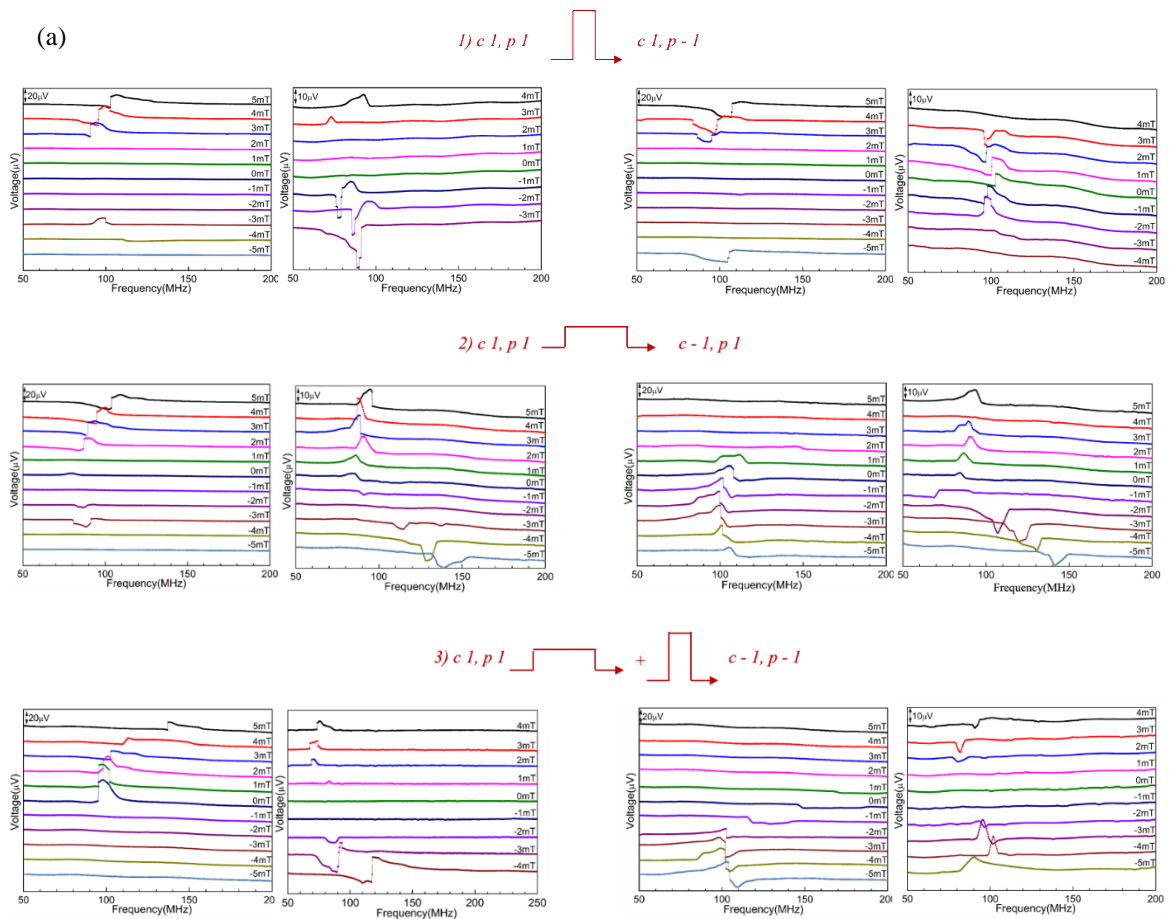


FIG A.1(a) Different combinations of vortex states obtained from ( $c\ 1, p\ 1$ ) state.

Fig A.1 (b) shows the following three combinations of circulation and polarity and their switching by different current pulses.

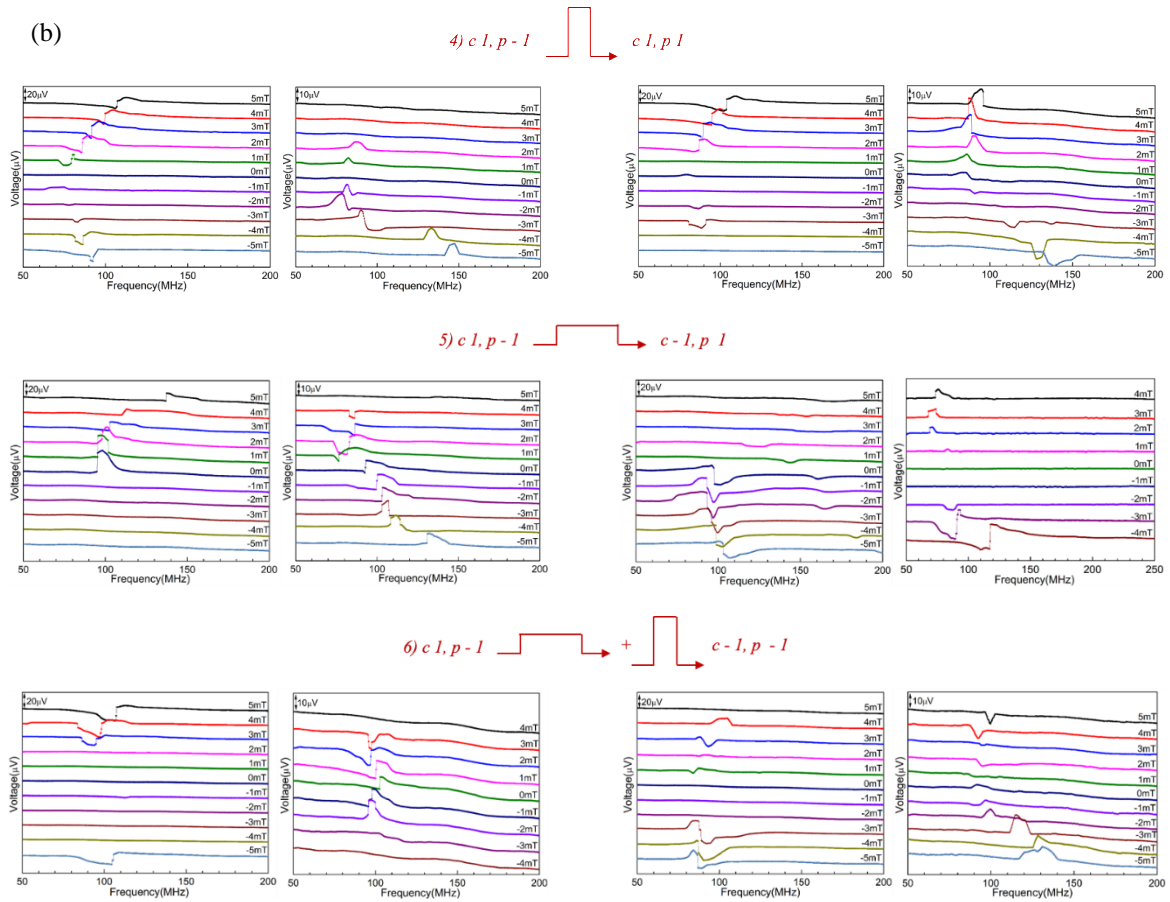
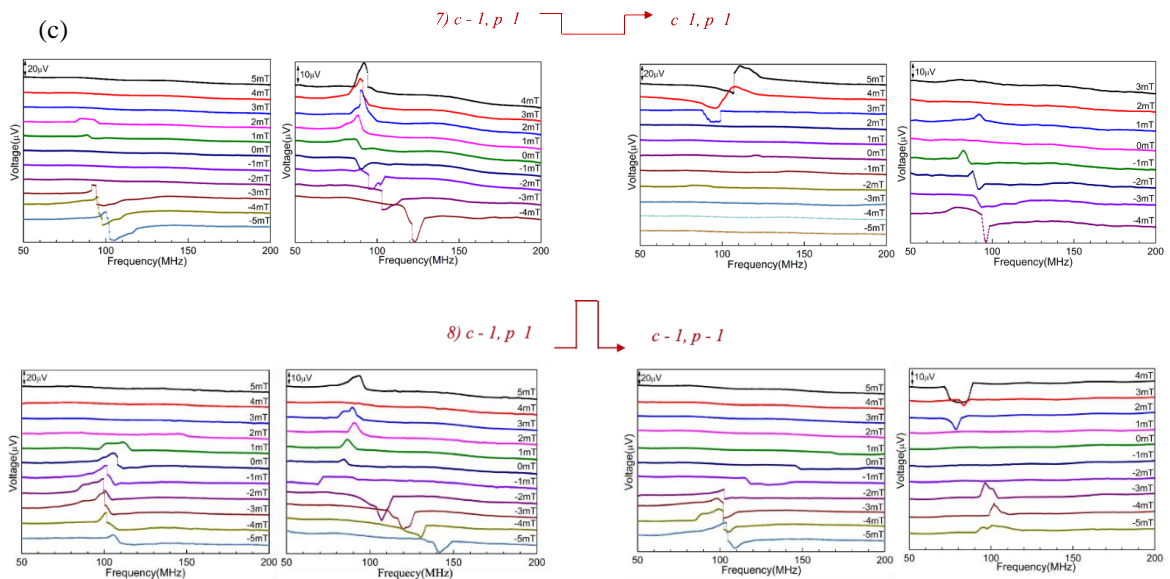


FIG A.1 (b) Different combinations of vortex states obtained from  $(c\ l, p\ -l)$  state.

Fig A.1 (c) shows the further three combinations of circulation and polarity and their switching by different current pulses.



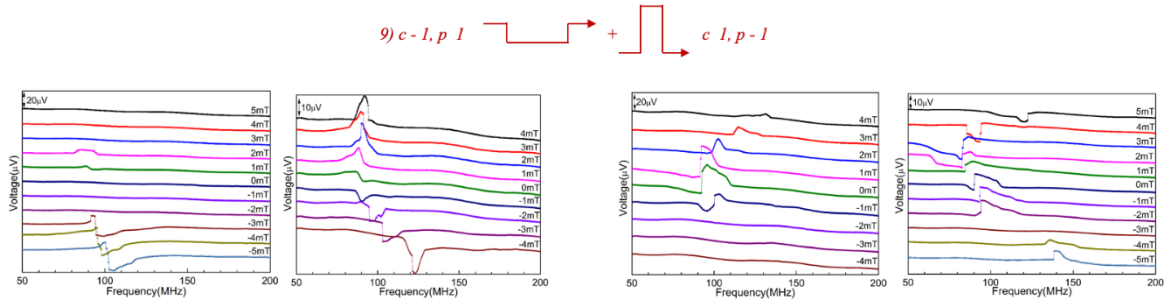


FIG A.1 (c) Different combinations of vortex states obtained from  $(c-l, p-l)$  state.

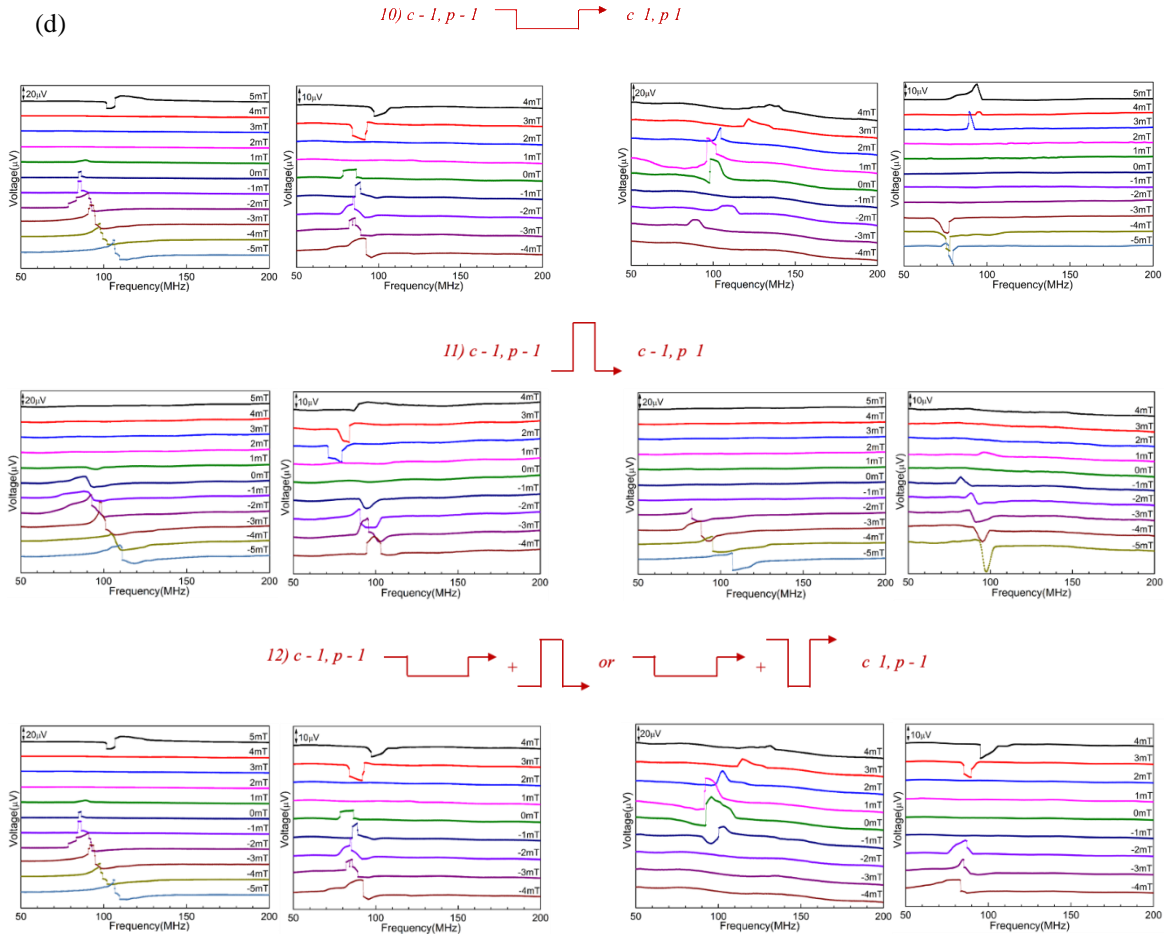


FIG A.1 (d) Different combinations of vortex states obtained from  $(c-l, p-l)$  state. FIG (a)-(d) shows the twelve different possible configurations with various states and their switching by current pulses. The above measurements were performed at rf power of -14 dBm to -11 dBm.

## Appendix B

In this section, I describe the samples used in the thesis.

No.	Sample ID	Description	Analysis done	Comment
1.	S. 1-10	1 $\mu\text{m}$ , 30(50) nm NiFe disks on Au waveguide	MFMM + Pulse generator	
2.	S. 11-20	2 $\mu\text{m}$ , 30(50) nm NiFe disks on Au waveguide	MFMM + Pulse generator	SID #13, Results used in Fig. 5.2.
3.	S.1-5	Ta 5nm/Pt 5nm/4x(Co 1nm/Pt 1.2nm)/NiFe 30nm	MTXM	2 samples destroyed at ALS SID #4, Results used in Fig. 5.3, Fig.5.4.
4.	S.6-10	Ta 5nm/Pt 5nm/4x(Co1.2 nm/Pt 7 nm)/NiFe 35 nm	MTXM	3 samples destroyed at ALS
5.	PMA 1, S. 1-12	Ta 5nm/Pt 5nm/5(10,15)xCo 0.2nm/Pt 0.4nm(last Pt 2nm)/(NiFe 30 nm)	MFMM + magnetic field + MOKE + VSM	
6.	PMA 2, S. 1-12	Ta 5nm/Pt 5nm/5(10,15)xCo 0.3nm/Pt 0.6nm(last Pt 2nm)/(NiFe 30 nm)	MFMM + magnetic field + MOKE + VSM	SID #2, Results used in Fig. 5.6.
7.	PMA 3, S. 1-12	Ta 5nm/Pt 5nm/5(10,15)xCo 0.5nm/Pt 1.0nm/(NiFe 30 nm)	MFMM + magnetic field + MOKE + VSM	
8.	PMA 4, S. 1-12	Ta 5nm/Pt 5nm/5(10,15)xCo 0.8nm/Pt 1.6nm/(NiFe 30 nm)	MFMM + magnetic field + MOKE + VSM	
9.	PMA 5, S. 1-12	Ta 5nm/Pt 5nm/5(10,15)xCo 1nm/Pt 2nm/(NiFe 30nm)	MFMM + magnetic field + MOKE + VSM	

10.	S. 1-10	4 $\mu\text{m}$ NiFe disk on Au waveguide 2 $\mu\text{m}$ chopped PMA + NiFe disk on Au waveguide	Static AMR	SID #3, Results used in Fig. 5.10(a). SID #8, Results used in Fig. 5.10(b).
11.	S. 1-200	2 $\mu\text{m}$ chopped PMA + NiFe disk on Au waveguide	Dynamic AMR	SID #31, Results used in Fig. 5.13, Fig. 5.14, Fig. 5.15, Fig. 5.16. SID #53, Results used in Fig. 5.18, Fig. 5.19, Fig. 5.22. SID #99, Results used in Fig. 5.23. SID #135, Results used in Fig. A1. Few samples burnt during wire-bonding(10%), some damage by static discharge (20%), some after repeated measurements

## References

1. Bohlens S, Krüger B, Drews A, et al (2008) Current controlled random-access memory based on magnetic vortex handedness. *Appl Phys Lett* 93:231–233. <https://doi.org/10.1063/1.2998584>
2. Blachowicz T, Ehrmann A (2011) Fourfold nanosystems for quaternary storage devices. *J Appl Phys* 110:1–4. <https://doi.org/10.1063/1.3646490>
3. J.P.J.Groenland (1992) Permalloy thin-film magnetic sensors. *Sensors and Actuators* 30:89–100
4. Kumar D, Barman S, Barman A (2014) Magnetic vortex based transistor operations. *Sci Rep* 4:. <https://doi.org/10.1038/srep04108>
5. Pribiag VS, Krivorotov IN, Fuchs GD, et al (2007) Magnetic vortex oscillator driven by d.c. spin-polarized current. *Nat Phys* 3:498–503. <https://doi.org/10.1038/nphys619>
6. Novosad V, Fradin FY, Roy PE, et al (2005) Magnetic vortex resonance in patterned ferromagnetic dots. *Phys Rev B - Condens Matter Mater Phys* 72:1–5. <https://doi.org/10.1103/PhysRevB.72.024455>
7. Hasegawa N, Sugimoto S, Fujimori H, et al (2015) Selective mode excitation in three-chained magnetic vortices. *Appl Phys Express* 8:. <https://doi.org/10.7567/APEX.8.063005>
8. Wintz S, Tiberkevich V, Weigand M, et al (2016) Magnetic vortex cores as tunable spin-wave emitters. *Nat Nanotechnol* 11:948–953. <https://doi.org/10.1038/nnano.2016.117>
9. Chappert C, Fert A, Van Dau FN (2007) The emergence of spin electronics in data storage. *Nat Mater* 6:813–823. <https://doi.org/10.1038/nmat2024>
10. Prinz GA (1999) Magnetoelectronics applications. *J Magn Magn Mater* 200:57–68. [https://doi.org/10.1016/S0304-8853\(99\)00335-2](https://doi.org/10.1016/S0304-8853(99)00335-2)
11. Yu YS, Jung H, Lee KS, et al (2011) Memory-bit selection and recording by rotating fields in vortex-core cross-point architecture. *Appl Phys Lett* 98:230–232. <https://doi.org/10.1063/1.3551524>
12. Huai Y (2008) Spin-transfer torque MRAM (STT-MRAM): Challenges and prospects. *AAPPS Bull* 18:33–40
13. Hertel R (2013) Vortex states à la carte. *Nat Nanotechnol* 8:318–320. <https://doi.org/10.1038/nnano.2013.81>
14. Shinjo T, Okuno T, Hassdorf R, et al (2000) Magnetic Vortex Core Observation in Circular Dots of Permalloy. *Science* (80- ) 289:930–931
15. Novosad V, Grimsditch M, Guslienko KY, et al (2002) Spin excitations of magnetic vortices in ferromagnetic nanodots. *Phys Rev B - Condens Matter Mater Phys* 66:524071–524074. <https://doi.org/10.1103/PhysRevB.66.052407>
16. A.R.Volkel (1994) Collective-variable approach to the dynamics of nonlinear magnetic excitations with application to vortices. *Phys Rev B* 50:95–97. <https://doi.org/10.7205/MILMED-D-16-00057>
17. Fernandez A, Cerjan CJ (2000) Nucleation and annihilation of magnetic vortices in submicron-scale Co dots. *J Appl Phys* 87:1395–1401. <https://doi.org/10.1063/1.372026>
18. Lee KS, Choi S, Kim SK (2005) Radiation of spin waves from magnetic vortex cores by their dynamic motion and annihilation processes. *Appl Phys Lett* 87:1–3. <https://doi.org/10.1063/1.2128478>
19. Thomas J (2007) vortex ups and downs. *Nat Nanotechnol* 2:.

<https://doi.org/10.1089/ars.2007.1714>

20. P.Szary (2009) Vortex stabilization in magnetic trilayer dots. *Mater Sci* 1:569–576. <https://doi.org/10.2755/jcmm010.003.20>
21. Bogdanov A (1994) Thermodynamically stable magnetic vortex states in magnetic crystals. *J Magn Magn Mater* 138:255–269. <https://doi.org/10.1057/palgrave.jors.2602213>
22. Cowburn RP, Koltsov DK, Adeyeye AO, et al (1999) Single-Domain Circular Nanomagnets. *Phys Rev Lett* 83:2–5. <https://doi.org/10.1103/PhysRevLett.83.1042>
23. Cowburn RP (2002) Magnetic nanodots for device applications. *J Magn Magn Mater* 242–245:505–511. [https://doi.org/10.1016/S0304-8853\(01\)01086-1](https://doi.org/10.1016/S0304-8853(01)01086-1)
24. Cowburn RP (2007) Spintronics: Change of direction. *Nat Mater* 6:255–256. <https://doi.org/10.1038/nmat1877>
25. Cowburn RP (2000) Property variation with shape in magnetic nanoelements. *J Phys D Appl Phys* 33:1–16. <https://doi.org/10.1088/0022-3727/33/1/201>
26. Cowburn RP, Koltsov DK, Adeyeye AO, Welland ME (1999) Designing nanostructured magnetic materials by symmetry. *Europhys Lett* 48:221–227. <https://doi.org/10.1209/epl/i1999-00469-9>
27. Pokhil T, Song D, Nowak J (2000) Spin vortex states and hysteretic properties of submicron size NiFe elements. *J Appl Phys* 87:6319–6321. <https://doi.org/10.1063/1.372692>
28. J.Raabe RP (2000) Magnetization Pattern of Permalloy Nanodisks. *J Appl Phys* 88:93040
29. Mamica S, Lévy JCS, Depondt P, Krawczyk M (2011) The effect of the single-spin defect on the stability of the in-plane vortex state in 2D magnetic nanodots. *J. Nanoparticle Res.* 13:6075–6083
30. Cowburn RP, Welland ME (1998) Micromagnetics of the single-domain state of square ferromagnetic nanostructures. *Phys Rev B* 58:9217–9226
31. Bogdanov A, Hubert A (1999) The stability of vortex-like structures in uniaxial ferromagnets. *J Magn Magn Mater* 195:182–192. [https://doi.org/10.1016/S0304-8853\(98\)01038-5](https://doi.org/10.1016/S0304-8853(98)01038-5)
32. Miyata M, Nonoguchi S, Yakata S, et al (2011) Static and dynamical properties of a magnetic vortex in a regular polygonal nanomagnet. *IEEE Trans Magn* 47:2505–2507. <https://doi.org/10.1109/TMAG.2011.2158408>
33. Koltsov DK, Cowburn RP, Welland ME (2000) Micromagnetics of ferromagnetic equilateral triangular prisms. *J Appl Phys* 88:5315–5317. <https://doi.org/10.1063/1.1315618>
34. Shi J, Tehrani S, Scheinfein MR (2000) Geometry dependence of magnetization vortices in patterned submicron NiFe elements. *Appl Phys Lett* 76:2588–2590. <https://doi.org/10.1063/1.126417>
35. Usov NA, Chang CR, Wei ZH (2001) Nonuniform magnetization structures in thin soft type ferromagnetic elements of elliptical shape. *J Appl Phys* 89:7591–7593. <https://doi.org/10.1063/1.1357133>
36. Hertel R, Kirschner J (2004) Dynamics of solenoidal magnetic structures in soft magnetic thin-film elements. *J Magn Magn Mater* 270:364–370. <https://doi.org/10.1016/j.jmmm.2003.08.031>
37. Liu X, Chapman JN, McVitie S, Wilkinson CDW (2004) Introduction and control of metastable states in elliptical and rectangular magnetic nanoelements. *Appl Phys Lett* 84:4406–4408. <https://doi.org/10.1063/1.1757647>
38. Vaz CAF, Kläui M, Bland JAC, et al (2006) Fundamental magnetic states of disk and ring



- elements. *Nucl Instruments Methods Phys Res* 246:13–19. <https://doi.org/10.1016/j.nimb.2005.12.006>
39. Shim JH, Kim DH, Mesler B, et al (2010) Magnetic vortex dynamics on a picoseconds timescale in a hexagonal Permalloy pattern. *J Appl Phys* 107:30–32. <https://doi.org/10.1063/1.3358223>
  40. Masseboeuf A, Fruchart O, Toussaint JC, et al (2010) Dimensionality crossover in magnetism: From domain walls (2D) to vortices (1D). *Phys Rev Lett* 104:2–5. <https://doi.org/10.1103/PhysRevLett.104.127204>
  41. Jung H, Choi YS, Lee KS, et al (2012) Logic operations based on magnetic-vortex-state networks. *ACS Nano* 6:3712–3717. <https://doi.org/10.1021/nn3000143>
  42. Kikuchi N, Okamoto S, Kitakami O, et al (2001) Vertical bistable switching of spin vortex in a circular magnetic dot. *J Appl Phys* 90:6548–6549. <https://doi.org/10.1063/1.1416132>
  43. Schneider M, Hoffmann H, Zweck J (2001) Magnetic switching of single vortex permalloy elements. *Appl Phys Lett* 79:3113–3115. <https://doi.org/10.1063/1.1410873>
  44. Van Waeyenberge B, Puzic A, Stoll H, et al (2006) Magnetic vortex core reversal by excitation with short bursts of an alternating field. *Nature* 444:461–464. <https://doi.org/10.1038/nature05240>
  45. Uhlř V, Urbánek M, Hladík L, et al (2013) Dynamic switching of the spin circulation in tapered magnetic nanodisks. *Nat Nanotechnol* 8:341–346. <https://doi.org/10.1038/nnano.2013.66>
  46. Choi YS, Yoo MW, Lee KS, et al (2010) Out-of-plane current controlled switching of the fourfold degenerate state of a magnetic vortex in soft magnetic nanodots. *Appl Phys Lett* 96:2010–2012. <https://doi.org/10.1063/1.3310017>
  47. Y. Gaididei et. al. (2010) Magnetic vortex dynamics induced by an electrical current. *Int J Quantum Chem* 110:83–97. <https://doi.org/10.1002/qua>
  48. Weigand M, Van Waeyenberge B, Vansteenkiste A, et al (2009) Vortex core switching by coherent excitation with single in-plane magnetic field pulses. *Phys Rev Lett* 102:20–23. <https://doi.org/10.1103/PhysRevLett.102.077201>
  49. Guslienko K, Lee K-S, Kim S-K (2008) Dynamic Origin of Vortex Core Switching in Soft Magnetic Nanodots. *Phys Rev Lett* 100:027203. <https://doi.org/10.1103/PhysRevLett.100.027203>
  50. Curcic M, Van Waeyenberge B, Vansteenkiste A, et al (2008) Polarization selective magnetic vortex dynamics and core reversal in rotating magnetic fields. *Phys Rev Lett* 101:1–4. <https://doi.org/10.1103/PhysRevLett.101.197204>
  51. Kammerer M, Weigand M, Curcic M, et al (2011) Magnetic vortex core reversal by excitation of spin waves. *Nat Commun* 2:276–279. <https://doi.org/10.1038/ncomms1277>
  52. Garcia F, Westfahl H, Schoenmaker J, et al (2010) Tailoring magnetic vortices in nanostructures. *Appl Phys Lett* 97:173–175. <https://doi.org/10.1063/1.3462305>
  53. Shimon G, Ravichandar V, Adeyeye AO, Ross CA (2014) Simultaneous control of vortex polarity and chirality in thickness-modulated [Co/Pd]<sub>n</sub>/Ti/Ni<sub>80</sub>Fe<sub>20</sub> disks. *Appl Phys Lett* 105:. <https://doi.org/10.1063/1.4897954>
  54. Kammerer M, Stoll H, Noske M, et al (2012) Fast spin-wave-mediated magnetic vortex core reversal. *Phys Rev B - Condens Matter Mater Phys* 86:1–5. <https://doi.org/10.1103/PhysRevB.86.134426>
  55. Cowburn RP, Koltsov DK, Adeyeye AO, Welland ME (2000) Lateral interface anisotropy in nanomagnets. *J Appl Phys* 87:7067–7069. <https://doi.org/10.1063/1.372933>

56. Cambel V, Karapetrov G (2011) Control of vortex chirality and polarity in magnetic nanodots with broken rotational symmetry. *Phys Rev B - Condens Matter Mater Phys* 84:1–5. <https://doi.org/10.1103/PhysRevB.84.014424>
57. Nakano K, Chiba D, Ohshima N, et al (2011) All-electrical operation of magnetic vortex core memory cell. *Appl Phys Lett* 99:1–3. <https://doi.org/10.1063/1.3673303>
58. Nakano K, Tanabe K, Hiramatsu R, et al (2013) Real-time observation of electrical vortex core switching. *Appl Phys Lett* 102:2–4. <https://doi.org/10.1063/1.4793212>
59. Nishimura N, Hirai T, Koganei A, et al (2002) Magnetic tunnel junction device with perpendicular magnetization films for high-density magnetic random access memory. *J Appl Phys* 91:5246–5249. <https://doi.org/10.1063/1.1459605>
60. Sort J, Buchanan K, Novosad V, et al (2006) Imprinting Vortices into Antiferromagnets. *Phys Rev Lett* 97:067201. <https://doi.org/10.1103/PhysRevLett.97.067201>
61. Salazar-Alvarez G, Kavich JJ, Sort J, et al (2009) Direct evidence of imprinted vortex states in the antiferromagnet of exchange biased microdisks. *Appl Phys Lett* 95:012510. <https://doi.org/10.1063/1.3168515>
62. J.M.D.Coe (2009) *Magnetism and Magnetic Materials*
63. Antos R, Otani Y, Shibata J (2008) Magnetic vortex dynamics. *J Phys Soc Japan* 77:1–8. <https://doi.org/10.1143/JPSJ.77.031004>
64. Aharoni A (1996) *Introduction to the Theory of Ferromagnetism (International Series of Monographs on Physics)*. 336
65. Blundell S (2015) *Magnetism in Condensed Matter*. OXFORD Univ Press 1:251. <https://doi.org/10.1017/CBO9781107415324.004>
66. Zagorodny JP, Gaididei Y, Mertens FG, Bishop AR (2003) Switching of vortex polarization in 2D easy-plane magnets by magnetic fields. *Eur Phys J B* 31:471–487. <https://doi.org/10.1140/epjb/e2003-00057-y>
67. Hrabec A (2011) *Domain wall dynamics in magnetic nanostructures : Effect of magnetic field and electric current*. Phd thesis
68. K.Y.Guslienko (2001) Evolution and stability of a magnetic vortex in a small cylindrical ferromagnetic particle under applied field. *Phys Rev B - Condens Matter Mater Phys* 63:1–4. <https://doi.org/10.1063/1.3462305>
69. Kamionka T, Martens M, Drews A, et al (2011) Influence of temperature on the gyrotropic eigenmode of magnetic vortices. *Phys Rev B - Condens Matter Mater Phys* 83:1–6. <https://doi.org/10.1103/PhysRevB.83.224424>
70. Hubert A (2009) *Magnetic domains: The Analysis of Magnetic Microstructures*
71. Scharbach PN (1983) A Dynamical Theory of the Electromagnetic Field. *Phys. Bull.* 34:522–522
72. Staňo M (2014) *Characterization of magnetic nanostructures by magnetic force microscopy*
73. Lopusnik R, Nibarger JP, Silva TJ, Celinski Z (2003) Different dynamic and static magnetic anisotropy in thin permalloy<sup>TM</sup> films. *Appl Phys Lett* 83:96–98. <https://doi.org/10.1063/1.1587255>
74. Thiaville A, Rohart S, Jué É, et al (2012) Dynamics of Dzyaloshinskii domain walls in ultrathin magnetic films. *Epl* 100:. <https://doi.org/10.1209/0295-5075/100/57002>
75. Bogdanov AN, Rößler UB (2001) Chiral symmetry breaking in magnetic thin films and

- multilayers. Phys Rev Lett 87:37203-1-37203-4. <https://doi.org/10.1103/PhysRevLett.87.037203>
76. Hertel R, Kirschner J (2004) Resonant modes of vortex structures in soft-magnetic nanodisks. *J Magn Magn Mater* 272–276:655–656. <https://doi.org/10.1016/j.jmmm.2003.12.678>
  77. J.Stohr Magnetism: From fundamentals to nanoscale dynamics
  78. He L, Doyle WD, Fujiwara H (1994) High Speed Coherent Switching Below the Stoner-Wohlfarth Limit. *IEEE Trans Magn* 30:4086–4088. <https://doi.org/10.1109/20.333997>
  79. LANDAU L, LIFSHITZ E (1935) On the theory of the dispersion of magnetic permeability in ferromagnetic bodies. *Perspect Theor Phys* 8:153–169. <https://doi.org/10.1016/b978-0-08-036364-6.50008-9>
  80. Gilbert TL (2004) A phenomenological theory of damping in ferromagnetic materials. *IEEE Trans Magn* 40:3443–3449. <https://doi.org/10.1109/TMAG.2004.836740>
  81. Uhlíř V (2010) Current induced magnetization dynamics in nanostructures. Phd thesis
  82. Mallinson JC (1987) On Damped Gyromagnetic Precession. *IEEE Trans Magn* 23:2003–2004. <https://doi.org/10.1109/TMAG.1987.1065181>
  83. Chien CL, Zhu FQ, Zhu JG (2007) Patterned nanomagnets. *Phys Today* 60:40–45. <https://doi.org/10.1063/1.2754602>
  84. Balajka J (2013) Switching vortex chirality in magnetostatically coupled permalloy nanodisks. Master Thesis
  85. Usov NA, Peschany SE (1993) Magnetization curling in a fine cylindrical particle. *J Magn Magn Mater* 118:290–294. [https://doi.org/10.1016/0304-8853\(93\)90428-5](https://doi.org/10.1016/0304-8853(93)90428-5)
  86. Guslienko KY (2006) Low-frequency vortex dynamic susceptibility and relaxation in mesoscopic ferromagnetic dots. *Appl Phys Lett* 89:. <https://doi.org/10.1063/1.2221904>
  87. Hengstmann TM, Grundler D, Heyn C, Heitmann D (2001) Stray-field investigation on permalloy nanodisks. *J Appl Phys* 90:6542–6544. <https://doi.org/10.1063/1.1413238>
  88. Rahm M, Schneider M, Biberger J, et al (2003) Vortex nucleation in submicrometer ferromagnetic disks. *Appl Phys Lett* 82:4110–4112. <https://doi.org/10.1063/1.1581363>
  89. Vaňatka M, Urbánek M, Jíra R, et al (2017) Magnetic vortex nucleation modes in static magnetic fields. *AIP Adv* 7:. <https://doi.org/10.1063/1.5006235>
  90. Scholz W, Guslienko KY, Novosad V, et al (2003) Transition from single-domain to vortex state in soft magnetic cylindrical nanodots. *J Magn Magn Mater* 266:155–163. [https://doi.org/10.1016/S0304-8853\(03\)00466-9](https://doi.org/10.1016/S0304-8853(03)00466-9)
  91. Novosad V, Guslienko KY, Shima H, et al (2001) Nucleation and annihilation of magnetic vortices in sub-micron permalloy dots. *IEEE Trans Magn* 37:2088–2090. <https://doi.org/10.1109/20.951062>
  92. Guslienko KY, Novosad V, Otani Y, et al (2001) Field evolution of magnetic vortex state in ferromagnetic disks. *Appl Phys Lett* 78:3848–3850. <https://doi.org/10.1063/1.1377850>
  93. Guslienko KY, Novosad V, Otani Y, et al (2001) Magnetization reversal due to vortex nucleation, displacement, and annihilation in submicron ferromagnetic dot arrays. *Phys Rev B - Condens Matter Phys* 65:244141–2441410. <https://doi.org/10.1103/PhysRevB.65.024414>
  94. M.J.Donahue and D.G.Porter (1999) OOMMF user’s guide, version 1.0. Natl Inst Stand Technol

95. Urbánek M, Uhlíř V, Lambert CH, et al (2015) Dynamics and efficiency of magnetic vortex circulation reversal. *Phys Rev B* 91:1–11. <https://doi.org/10.1103/PhysRevB.91.094415>
96. W.F.Brown (1968) The Fundamental Theorem of Fine-Ferromagnetic-Particle Theory. *J Alloys Compd* 39:992–994. [https://doi.org/10.1142/9789812384904\\_0009](https://doi.org/10.1142/9789812384904_0009)
97. Aharoni A (1990) Upper bound to a single-domain behavior of a ferromagnetic cylinder. *J Appl Phys* 68:2892–2900. <https://doi.org/10.1063/1.346422>
98. K.L.Metlov (2002) Stability of magnetic vortex in soft magnetic nano sized circular cylinder. *J Magn Magn Mater* 242–245:1015–1017. [https://doi.org/10.1016/S0304-8853\(01\)01360-9](https://doi.org/10.1016/S0304-8853(01)01360-9)
99. Goirienea-Goikoetxea M, Guslienko KY, Rouco M, et al (2017) Magnetization reversal in circular vortex dots of small radius. *Nanoscale* 9:11269–11278. <https://doi.org/10.1039/c7nr02389h>
100. Chung SH, McMichael RD, Pierce DT, Unguris J (2010) Phase diagram of magnetic nanodisks measured by scanning electron microscopy with polarization analysis. *Phys Rev B* 81:1–7. <https://doi.org/10.1103/PhysRevB.81.024410>
101. Höllinger R, Killinger A, Krey U (2003) Statics and fast dynamics of nanomagnets with vortex structure. *J Magn Magn Mater* 261:178–189. [https://doi.org/10.1016/S0304-8853\(02\)01471-3](https://doi.org/10.1016/S0304-8853(02)01471-3)
102. Yakata S, Miyata M, Nonoguchi S, et al (2010) Control of vortex chirality in regular polygonal nanomagnets using in-plane magnetic field. *Appl Phys Lett* 97:2–4. <https://doi.org/10.1063/1.3521407>
103. Jaafar M, Yanes R, Perez De Lara D, et al (2010) Control of the chirality and polarity of magnetic vortices in triangular nanodots. *Phys Rev B* 81:1–7. <https://doi.org/10.1103/PhysRevB.81.054439>
104. K.Yu.Guslienko (2008) Magnetic vortex state stability, reversal and dynamics in restricted geometries. *J Nanosci Nanotechnol* 8:2745–2760. <https://doi.org/10.1063/1.3409957>
105. Guslienko KY, Novosad V, Otani Y, et al (2002) Magnetization reversal due to vortex nucleation, displacement, and annihilation in submicron ferromagnetic dot arrays. *Phys Rev B - Condens Matter Mater Phys* 65:244141–2441410. <https://doi.org/10.1103/PhysRevB.65.024414>
106. Vanatka M Spin vortex states in magnetostatically coupled magnetic nanodisks. Master Thesis 459–513
107. Schneider M, Hoffmann H, Otto S, et al (2002) Stability of magnetic vortices in flat submicron permalloy cylinders. *J Appl Phys* 92:1466–1472. <https://doi.org/10.1063/1.1490623>
108. Thiele AA (1973) Steady-state motion of magnetic domains. *Phys Rev Lett* 30:230–233. <https://doi.org/10.1103/PhysRevLett.30.230>
109. D.L.Huber (1982) Dynamics of spin vortices in two-dimensional planar magnets. *Phys Rev B* 26:3758–3765. <https://doi.org/10.1103/PhysRevB.26.3758>
110. Dussaux A, Khvalkovskiy A V., Bortolotti P, et al (2012) Field dependence of spin-transfer-induced vortex dynamics in the nonlinear regime. *Phys Rev B - Condens Matter Mater Phys* 86:1–10. <https://doi.org/10.1103/PhysRevB.86.014402>
111. J.Shibata (2007) Magnetic vortex dynamics induced by spin-transfer torque. *J Magn Magn Mater* 310:2041–2042. <https://doi.org/10.1103/PhysRevLett.100.176601>
112. Guslienko KY, Heredero RH, Chubykalo-Fesenko O (2010) Nonlinear gyrotropic vortex dynamics in ferromagnetic dots. *Phys Rev B - Condens Matter Mater Phys* 82:1–9. <https://doi.org/10.1103/PhysRevB.82.014402>

113. Yoo MW, Lee KS, Han DS, Kim SK (2011) Perpendicular-bias-field-dependent vortex-gyration eigenfrequency. *J Appl Phys* 109:1–4. <https://doi.org/10.1063/1.3563561>
114. Pigeau B (2013) Magnetic vortex dynamics nanostructures. PhD thesis
115. Dussaux A, Georges B, Grollier J, et al (2010) Large microwave generation from current-driven magnetic vortex oscillators in magnetic tunnel junctions. *Nat Commun* 1:1–6. <https://doi.org/10.1038/ncomms1006>
116. Chen T-Y (2012) Magnetic Vortex Dynamics : Non-linear Dynamics , Pinning Mechanisms , and Dimensionality Crossover. Phd thesis
117. Guslienko KY, Ivanov BA, Novosad V, et al (2002) Eigenfrequencies of vortex state excitations in magnetic submicron-size disks. *J Appl Phys* 91:8037–8039. <https://doi.org/10.1063/1.1450816>
118. Lee KS, Kim SK (2008) Two circular-rotational eigenmodes and their giant resonance asymmetry in vortex gyrotropic motions in soft magnetic nanodots. *Phys Rev B - Condens Matter Mater Phys* 78:1–6. <https://doi.org/10.1103/PhysRevB.78.014405>
119. Feiring MT (2015) Magnetic vortex dynamics in interacting micromagnets
120. Toscano D, Leonel SA, Dias RA, et al (2011) Vortex core scattering and pinning by impurities in nanomagnets. *J Appl Phys* 109:3–5. <https://doi.org/10.1063/1.3573518>
121. Uhlig T, Rahm M, Dietrich C, et al (2005) Shifting and pinning of a magnetic vortex core in a permalloy dot by a magnetic field. *Phys Rev Lett* 95:1–4. <https://doi.org/10.1103/PhysRevLett.95.237205>
122. Compton RL, Crowell PA (2006) Dynamics of a pinned magnetic vortex. *Phys Rev Lett* 97:. <https://doi.org/10.1103/PhysRevLett.97.137202>
123. Kim JS, Boule O, Verstoep S, et al (2010) Current-induced vortex dynamics and pinning potentials probed by homodyne detection. *Phys Rev B - Condens Matter Mater Phys* 82:1–7. <https://doi.org/10.1103/PhysRevB.82.104427>
124. Compton R (2007) Vortex pinning and dynamics
125. Vavassori P, Bisero D, Bonanni V, et al (2008) Magnetostatic dipolar domain-wall pinning in chains of permalloy triangular rings. *Phys Rev B - Condens Matter Mater Phys* 78:1–7. <https://doi.org/10.1103/PhysRevB.78.174403>
126. Min H, McMichael RD, Miltat J, Stiles MD (2011) Effects of disorder on magnetic vortex gyration. *Phys Rev B - Condens Matter Mater Phys* 83:1–8. <https://doi.org/10.1103/PhysRevB.83.064411>
127. Moriya R, Thomas L, Hayashi M, et al (2008) Probing vortex-core dynamics using current-induced resonant excitation of a trapped domain wall. *Nat Phys* 4:368–372. <https://doi.org/10.1038/nphys936>
128. Sugimoto S, Hasegawa N, Niimi Y, et al (2014) Detection of a symmetric circular gyration of the vortex core via the second-order harmonic magnetoresistance oscillation. *Appl Phys Express* 7:3–6. <https://doi.org/10.7567/APEX.7.023006>
129. Chen TY, Galkiewicz AT, Crowell PA (2012) Phase diagram of magnetic vortex dynamics. *Phys Rev B - Condens Matter Mater Phys* 85:1–5. <https://doi.org/10.1103/PhysRevB.85.180406>
130. Buchanan KS, Grimsditch M, Fradin FY, et al (2007) Driven dynamic mode splitting of the magnetic vortex translational resonance. *Phys Rev Lett* 99:1–4. <https://doi.org/10.1103/PhysRevLett.99.267201>

131. Guslienko KY, Slavin AN, Tiberkevich V, Kim SK (2008) Dynamic origin of azimuthal modes splitting in vortex-state magnetic dots. *Phys Rev Lett* 101:1–4. <https://doi.org/10.1103/PhysRevLett.101.247203>
132. Awad AA, Guslienko KY, Sierra JF, et al (2010) Precise probing spin wave mode frequencies in the vortex state of circular magnetic dots. *Appl Phys Lett* 96:3–5. <https://doi.org/10.1063/1.3268453>
133. Buchanan KS, Roy PE, Grimsditch M, et al (2006) Magnetic-field tunability of the vortex translational mode in micron-sized permalloy ellipses: Experiment and micromagnetic modeling. *Phys Rev B - Condens Matter Mater Phys* 74:1–5. <https://doi.org/10.1103/PhysRevB.74.064404>
134. Sushruth M, Fried JP, Anane A, et al (2016) Electrical measurement of magnetic-field-impeded polarity switching of a ferromagnetic vortex core. *Phys Rev B* 94:1–5. <https://doi.org/10.1103/PhysRevB.94.100402>
135. De Loubens G, Riegler A, Pigeau B, et al (2009) Bistability of vortex core dynamics in a single perpendicularly magnetized nanodisk. *Phys Rev Lett* 102:1–4. <https://doi.org/10.1103/PhysRevLett.102.177602>
136. Uhlíř V, Urbánek M, Fischer P, et al Magnetic vortices: controlled dynamic switching of the curl made fast and energy-efficient. 1–5
137. Guslienko KY, Lee KS, Kim SK (2008) Dynamic origin of vortex core switching in soft magnetic nanodots. *Phys Rev Lett* 100:1–4. <https://doi.org/10.1103/PhysRevLett.100.027203>
138. Khvalkovskiy A V., Slavin AN, Grollier J, et al (2010) Critical velocity for the vortex core reversal in perpendicular bias magnetic field. *Appl Phys Lett* 96:. <https://doi.org/10.1063/1.3291064>
139. Hertel R, Gliga S, Fähnle M, Schneider CM (2007) Ultrafast nanomagnetic toggle switching of vortex cores. *Phys Rev Lett* 98:1–4. <https://doi.org/10.1103/PhysRevLett.98.117201>
140. Sheka DD, Gaididei Y, Mertens FG (2007) Current induced switching of vortex polarity in magnetic nanodisks. *Appl Phys Lett* 91:89–92. <https://doi.org/10.1063/1.2775036>
141. Guslienko KY, Han XF, Keavney DJ, et al (2006) Magnetic vortex core dynamics in cylindrical ferromagnetic dots. *Phys Rev Lett* 96:1–4. <https://doi.org/10.1103/PhysRevLett.96.067205>
142. Xiao QF, Rudge J, Choi BC, et al (2006) Dynamics of vortex core switching in ferromagnetic nanodisks. *Appl Phys Lett* 89:. <https://doi.org/10.1063/1.2424673>
143. MacHado TS, Rappoport TG, Sampaio LC (2008) Static and dynamic properties of vortices in anisotropic magnetic disks. *Appl Phys Lett* 93:. <https://doi.org/10.1063/1.2985901>
144. Kravchuk VP, Gaididei Y, Sheka DD (2009) Nucleation of a vortex-antivortex pair in the presence of an immobile magnetic vortex. *Phys Rev B - Condens Matter Mater Phys* 80:1–4. <https://doi.org/10.1103/PhysRevB.80.100405>
145. Yoo MW, Lee KS, Jeong DE, Kim SK (2010) Origin, criterion, and mechanism of vortex-core reversals in soft magnetic nanodisks under perpendicular bias fields. *Phys Rev B* 82:1–5. <https://doi.org/10.1103/PhysRevB.82.174437>
146. Okuno T, Shigeto K, Ono T, et al (2002) MFM study of magnetic vortex cores in circular permalloy dots: Behavior in external field. *J Magn Magn Mater* 240:1–6. [https://doi.org/10.1016/S0304-8853\(01\)00708-9](https://doi.org/10.1016/S0304-8853(01)00708-9)
147. Thiaville A, García JM, Dittrich R, et al (2003) Micromagnetic study of Bloch-point-mediated vortex core reversal. *Phys Rev B - Condens Matter Mater Phys* 67:1–12. <https://doi.org/10.1103/PhysRevB.67.094410>

148. Curcic M, Stoll H, Weigand M, et al (2011) Magnetic vortex core reversal by rotating magnetic fields generated on micrometer length scales. *Phys Status Solidi Basic Res* 248:2317–2322. <https://doi.org/10.1002/pssb.201147208>
149. Vansteenkiste A, Wiele B Van de, Weigand M (2011) Observation of non-linear magnetic vortex gyration by X-ray microscopy and micromagnetic simulations. *Condens Mater* 1–11
150. Kasai S, Nakatani Y, Kobayashi K, et al (2007) Magnetization reversal in a ferromagnetic circular dot under current induced resonant excitation. *J Magn Magn Mater* 310:2351–2352. <https://doi.org/10.1016/j.jmmm.2006.11.102>
151. Zhong Z, Zhang H, Tang X, et al (2009) Vortex chirality control in magnetic submicron dots with asymmetrical magnetic properties in lateral direction. *J Magn Magn Mater* 321:2345–2349. <https://doi.org/10.1016/j.jmmm.2009.02.030>
152. Kasai S, Nakatani Y, Kobayashi K, et al (2006) Current-driven resonant excitation of magnetic vortices. *Phys Rev Lett* 97:1–4. <https://doi.org/10.1103/PhysRevLett.97.107204>
153. Nakatani Y, Ono T (2011) Effect of the Oersted field on a vortex core switching by pulse spin current. *Appl Phys Lett* 99:5–7. <https://doi.org/10.1063/1.3643140>
154. Yamada K, Kasai S, Nakatani Y, et al (2007) Electrical switching of the vortex core in a magnetic disk. *Nat Mater* 6:269–273. <https://doi.org/10.1038/nmat1867>
155. Kim SK, Choi YS, Lee KS, et al (2007) Electric-current-driven vortex-core reversal in soft magnetic nanodots. *Appl Phys Lett* 91:1. <https://doi.org/10.1063/1.2773748>
156. Yamada K, Kasai S, Nakatani Y, et al (2008) Switching magnetic vortex core by a single nanosecond current pulse. *Appl Phys Lett* 93:91–94. <https://doi.org/10.1063/1.3001588>
157. Shibata J, Nakatani Y, Tataru G, et al (2006) Current-induced magnetic vortex motion by spin-transfer torque. *Phys Rev B* 73:1. <https://doi.org/10.1016/j.jmmm.2006.10.949>
158. Nakatani Y, Shibata J, Tataru G, et al (2008) Nucleation and dynamics of magnetic vortices under spin-polarized current. *Phys Rev B - Condens Matter Mater Phys* 77:1–7. <https://doi.org/10.1103/PhysRevB.77.014439>
159. Caputo JG, Gaididei Y, Mertens FG, Sheka DD (2007) Vortex polarity switching by a spin-polarized current. *Phys Rev Lett* 98:1–4. <https://doi.org/10.1103/PhysRevLett.98.056604>
160. Pigeau B, De Loubens G, Klein O, et al (2011) Optimal control of vortex-core polarity by resonant microwave pulses. *Nat Phys* 7:26–31. <https://doi.org/10.1038/nphys1810>
161. Rückriem R, Schrefl T, Albrecht M (2014) Ultra-fast magnetic vortex core reversal by a local field pulse. *Appl Phys Lett* 104:18–22. <https://doi.org/10.1063/1.4864275>
162. Kravchuk VP, Sheka DD, Gaididei Y, Mertens FG (2007) Controlled vortex core switching in a magnetic nanodisk by a rotating field. *J Appl Phys* 102:1–4. <https://doi.org/10.1063/1.2770819>
163. Keavney DJ, Cheng XM, Buchanan KS (2009) Polarity reversal of a magnetic vortex core by a unipolar, nonresonant in-plane pulsed magnetic field. *Appl Phys Lett* 94:1–3. <https://doi.org/10.1063/1.3111430>
164. Novosad V, Guslienko KY, Shima H, et al (2002) Effect of interdot magnetostatic interaction on magnetization reversal in circular dot arrays. *Phys Rev B - Condens Matter Mater Phys* 65:1–4. <https://doi.org/10.1103/PhysRevB.65.060402>
165. Vargas NM, Allende S, Leighton B, et al (2011) Asymmetric magnetic dots: A way to control magnetic properties. *J Appl Phys* 109:1–5. <https://doi.org/10.1063/1.3561483>
166. Antos R, Urbanek M, Otani Y (2010) Controlling spin vortex states in magnetic nanodisks by

- magnetic field pulses. *J Phys Conf Ser* 200:. <https://doi.org/10.1088/1742-6596/200/4/042002>
167. Sushruth M, Fried JP, Anane A, et al (2017) Chirality-mediated bistability and strong frequency downshifting of the gyrotropic resonance of a magnetic vortex due to dynamic destiffening. *Phys Rev B* 96:1–5. <https://doi.org/10.1103/PhysRevB.96.060405>
  168. Mironov VL, Gribkov BA, Fraerman AA, et al (2007) MFM probe control of magnetic vortex chirality in elliptical Co nanoparticles. *J Magn Magn Mater* 312:153–157. <https://doi.org/10.1016/j.jmmm.2006.09.032>
  169. Gaididei Y, Sheka DD, Mertens FG (2008) Controllable switching of vortex chirality in magnetic nanodisks by a field pulse. *Appl Phys Lett* 92:. <https://doi.org/10.1063/1.2829795>
  170. Konoto M, Yamada T, Koike K, et al (2008) Formation and control of magnetic vortex chirality in patterned micromagnet arrays. *J Appl Phys* 103:1–4. <https://doi.org/10.1063/1.2828177>
  171. Yakata S, Miyata M, Honda S, et al (2011) Chirality control of magnetic vortex in a square Py dot using current-induced Oersted field. *Appl Phys Lett* 99:. <https://doi.org/10.1063/1.3669410>
  172. Antos R, Otani Y (2009) Simulations of the dynamic switching of vortex chirality in magnetic nanodisks by a uniform field pulse. *Phys Rev B - Condens Matter Mater Phys* 80:1–4. <https://doi.org/10.1103/PhysRevB.80.140404>
  173. Nickel J (1995) Magnetoresistance Overview. 11
  174. Mcguire TR, Potter RI (1975) Anisotropic Magnetoresistance in Ferromagnetic 3D Alloys. *IEEE Trans Magn* 11:1018–1038. <https://doi.org/10.1109/TMAG.1975.1058782>
  175. I.A.Campbell (1982) Transport properties of ferromagnets
  176. Parkin SSP (1991) Systematic variation of the strength and oscillation period of indirect magnetic exchange coupling through the 3d, 4d, and 5d transition metals. *Phys Rev Lett* 67:3598–3601. <https://doi.org/10.1103/PhysRevLett.67.3598>
  177. Moodera JS, Kinder LR, Wong TM, Meservey R (1995) Large magnetoresistance at room temperature in ferromagnetic thin film tunnel junctions. *Phys Rev Lett* 74:3273–3276. <https://doi.org/10.1103/PhysRevLett.74.3273>
  178. Meservey R, Tedrow PM, Fulde P (1970) Magnetic field splitting of the quasiparticle states in superconducting aluminum films. *Phys Rev Lett* 25:1270–1272. <https://doi.org/10.1103/PhysRevLett.25.1270>
  179. M.D.Stiles (2006) Spin transfer torque and dynamics. *spin Dyn Confin Magn Struct III* 101:225–308. <https://doi.org/10.1007/b12462>
  180. Ralph DC, Stiles MD (2008) Spin transfer torques. *J Magn Magn Mater* 320:1190–1216. <https://doi.org/10.1016/j.jmmm.2007.12.019>
  181. Han H-S (2016) Magnetic Vortex Dynamics in the Thick Ferromagnetic Nanoelement. Master Thesis
  182. Choi YS, Kim SK, Lee KS, Yu YS (2008) Understanding eigenfrequency shifts observed in vortex gyrotropic motions in a magnetic nanodot driven by spin-polarized out-of-plane dc current. *Appl Phys Lett* 93:. <https://doi.org/10.1063/1.3012380>
  183. Strachan JP, Chembrolu V, Acremann Y, et al (2008) Direct observation of spin-torque driven magnetization reversal through nonuniform modes. *Phys Rev Lett* 100:. <https://doi.org/10.1103/PhysRevLett.100.247201>
  184. Heyne L, Rhensius J, Ilgaz D, et al (2010) Direct determination of large spin-torque nonadiabaticity in vortex core dynamics. *Phys Rev Lett* 105:1–4.



- <https://doi.org/10.1103/PhysRevLett.105.187203>
185. Allenspach R, Eib P (2010) The alphabet of spin in nanostructures. *Physics* (College Park Md) 3:.. <https://doi.org/10.1103/Physics.3.91>
  186. Berger L (1978) Low-field magnetoresistance and domain drag in ferromagnets. *J Appl Phys* 49:2156–2161. <https://doi.org/10.1063/1.324716>
  187. Berger L (1979) Domain drag effect in the presence of variable magnetic field or variable transport current. *J Appl Phys* 50:2137–2139. <https://doi.org/10.1063/1.327083>
  188. Sugimoto S, Fukuma Y, Kasai S, et al (2011) Dynamics of coupled vortices in a pair of ferromagnetic disks. *Phys Rev Lett* 106:11–14. <https://doi.org/10.1103/PhysRevLett.106.197203>
  189. Gangwar A, Bauer HG, Chauleau JY, et al (2015) Electrical determination of vortex state in submicron magnetic elements. *Phys Rev B - Condens Matter Mater Phys* 91:2–6. <https://doi.org/10.1103/PhysRevB.91.094407>
  190. Slonczewski JC (1996) current driven excitation of magnetic multilayer. *J Magn Magn Mater* 159:L1–L7. <https://doi.org/10.4028/www.scientific.net/AMR.873.865>
  191. Mistral Q, Van Kampen M, Hrkac G, et al (2008) Current-driven vortex oscillations in metallic nanocontacts. *Phys Rev Lett* 100:1–4. <https://doi.org/10.1103/PhysRevLett.100.257201>
  192. Finocchio G, Pribiag VS, Torres L, et al (2010) Spin-torque driven magnetic vortex self-oscillations in perpendicular magnetic fields. *Appl Phys Lett* 96:96–98. <https://doi.org/10.1063/1.3358387>
  193. Goto M, Hata H, Yamaguchi A, et al (2011) Electric spectroscopy of vortex states and dynamics in magnetic disks. *Phys Rev B - Condens Matter Mater Phys* 84:1–9. <https://doi.org/10.1103/PhysRevB.84.064406>
  194. Goto M, Hata H, Yamaguchi A, et al (2011) Electrical detection of vortex states in a ferromagnetic disk using the rectifying effect. *J Appl Phys* 109:.. <https://doi.org/10.1063/1.3536390>
  195. Krüger B, Drews A, Bolte M, et al (2007) Harmonic oscillator model for current- and field-driven magnetic vortices. *Phys Rev B - Condens Matter Mater Phys* 76:1–5. <https://doi.org/10.1103/PhysRevB.76.224426>
  196. Cui X, Hu S, Hidegara M, et al (2015) Sensitive detection of vortex-core resonance using amplitude-modulated magnetic field. *Sci Rep* 5:6–10. <https://doi.org/10.1038/srep17922>
  197. Thiaville A, Nakatani Y, Miltat J, Suzuki Y (2005) Micromagnetic understanding of current-driven domain wall motion in patterned nanowires. *Europhys Lett* 69:990–996. <https://doi.org/10.1209/epl/i2004-10452-6>
  198. He J, Li Z, Zhang S (2006) Current-driven vortex domain wall dynamics by micromagnetic simulations. *Phys Rev B - Condens Matter Mater Phys* 73:1–7. <https://doi.org/10.1103/PhysRevB.73.184408>
  199. Rettner C, Thomas L, Hayashi M, et al (2006) Dependence of Current and Field Driven Depinning of Domain Walls on Their Structure and Chirality in Permalloy Nanowires. *Phys Rev Lett* 97:1–4. <https://doi.org/10.1103/physrevlett.97.207205>
  200. Youk H, Chern GW, Merit K, et al (2006) Composite domain walls in flat nanomagnets: The magnetostatic limit. *J Appl Phys* 99:99–102. <https://doi.org/10.1063/1.2167049>
  201. Tulapurkar AA, Suzuki Y, Fukushima A, et al (2005) Spin-torque diode effect in magnetic tunnel junctions. *Nat Lett* 438:339–342. <https://doi.org/10.1038/nature04207>

202. Zhu X, Grütter P (2004) Imaging , Manipulation , and Spectroscopic Measurements of Nanomagnets by Magnetic Force Microscopy. 457–462
203. Park MH, Hong YK, Gee SH, et al (2003) Magnetization configuration and switching behavior of submicron NiFe elements: Pac-man shape. *Appl Phys Lett* 83:329–331. <https://doi.org/10.1063/1.1592002>
204. Stoll H, Puzic A, Van Waeyenberge B, et al (2004) High-resolution imaging of fast magnetization dynamics in magnetic nanostructures. *Appl Phys Lett* 84:3328–3330. <https://doi.org/10.1063/1.1723698>
205. S.-B.Choe (2004) Vortex Core – Driven Magnetization Dynamics. *Science* (80- ) 304:420–422. <https://doi.org/10.1006/biol.2001.0291>
206. P.Fishcer (2006) Soft x-ray microscopy of nanomagnetism. *Mater Today* 9:. <https://doi.org/10.1103/PhysRevLett.106.167202>
207. Acremann Y (2008) Magnetization dynamics: ultra-fast and ultra-small. *Elsevier* 9:585–594. <https://doi.org/10.1016/j.crhy.2007.05.017>
208. Bolte M, Meier G, Krüger B, et al (2008) Time-resolved X-ray microscopy of spin-torque-induced magnetic vortex gyration. *Phys Rev Lett* 100:1–4. <https://doi.org/10.1103/PhysRevLett.100.176601>
209. Mesler BL, Buchanan K, Im M-Y, et al (2010) Magnetic soft x-ray imaging of vortex core dynamics. *Am vacuum Soc* 28:198–201. <https://doi.org/10.1116/1.3275939>
210. Yu XW, Pribiag VS, Acremann Y, et al (2011) Images of a spin-torque-driven magnetic nano-oscillator. *Phys Rev Lett* 106:1–4. <https://doi.org/10.1103/PhysRevLett.106.167202>
211. Schneider M, Hoffmann H, Zweck J (2000) Lorentz microscopy of circular ferromagnetic permalloy nanodisks. *Appl Phys Lett* 77:2909–2911. <https://doi.org/10.1063/1.1320465>
212. Vavassori P, Grimsditch M, Metlushko V, et al (2005) Magnetoresistance of single magnetic vortices. *Appl Phys Lett* 86:1–3. <https://doi.org/10.1063/1.1866212>
213. Segal A, Gerber A (2012) Core contribution to magnetotransport of ferromagnetic dots in vortex state. *J Appl Phys* 111:1–5. <https://doi.org/10.1063/1.3698504>
214. Cui X, Hu S, Kimura T (2014) Detection of a vortex nucleation position in a circular ferromagnet using asymmetrically configured electrodes. *Appl Phys Lett* 105:. <https://doi.org/10.1063/1.4894216>
215. Wren T, Kazakova O (2015) Anisotropic magnetoresistance effect in sub-micron nickel disks. *J Appl Phys* 117:. <https://doi.org/10.1063/1.4918967>
216. Ohe JI, Barnes SE, Lee HW, Maekawa S (2009) Electrical measurements of the polarization in a moving magnetic vortex. *Appl Phys Lett* 95:. <https://doi.org/10.1063/1.3237166>
217. Yamaguchi A, Motoi K, Miyajima H, et al (2010) Nonlinear Vortex Motion Induced by the Simultaneous Application of RF and DC Currents in a Micron-Sized Fe<sub>19</sub>Ni<sub>81</sub> disk. *IEEE Trans Magn* 46:1994–1997. <https://doi.org/10.1109/TMAG.2010.2040372>
218. Yue L, Liou SH (2011) Magnetic force microscopy studies of magnetic features and nanostructures. *Nanosci Technol* 116:287–319. [https://doi.org/10.1007/978-3-642-10497-8\\_10](https://doi.org/10.1007/978-3-642-10497-8_10)
219. Eaton P (2014) Atomic Force Microscopy Peter Eaton and Paul West. *MRS Bull* 39:379–379. <https://doi.org/10.1557/mrs.2014.72>
220. Agarwal DH, Bhatt PM, Pathan AM, et al (2012) Development of portable experimental set-up for AFM to work at cryogenic temperature. *AIP Conf Proc* 1447:531–532.

<https://doi.org/10.1063/1.4710113>

221. Fischer P (2010) Viewing spin structures with soft X-ray microscopy. *Mater Today* 13:14–22. [https://doi.org/10.1016/S1369-7021\(10\)70161-9](https://doi.org/10.1016/S1369-7021(10)70161-9)
222. Kasai S, Fischer P, Im MY, et al (2008) Probing the Spin polarization of current by soft X-ray imaging of current-induced magnetic vortex dynamics. *Phys Rev Lett* 101:1–4. <https://doi.org/10.1103/PhysRevLett.101.237203>
223. Qiu ZQ (2000) Surface magneto-optic Kerr effect. *Rev Sci Instrum* 71:
224. Flajsman L (2014) vectorial kerr magnetometry. Master Thesis
225. MacHado TS, Argollo De Menezes M, Rappoport TG, Sampaio LC (2011) Magnetotransport in nanostructures: The role of inhomogeneous currents. *J Appl Phys* 109:1–6. <https://doi.org/10.1063/1.3582149>
226. Huang YS, Wang CC, Adeyeye AO (2006) Determination of vortex chirality using planar Hall effect. *J Appl Phys* 100:. <https://doi.org/10.1063/1.2211327>
227. Ishida T, Kimura T, Otani Y (2006) Current induced vortex displacement and annihilation in a single permalloy disk. *Phys Rev B* 74:. <https://doi.org/10.1016/j.jmmm.2006.10.903>
228. Franssila S (2010) Introduction to Microfabrication
229. K.Suzuki (2007) Microlithigraphy. CRC Press Taylor Fr Gr Scienc an:
230. Li SP, Natali M, Lebib A, et al (2002) Magnetic nanostructure fabrication by soft lithography and vortex-single domain transition in Co dots. *J Magn Magn Mater* 241:447–452. [https://doi.org/10.1016/S0304-8853\(01\)00441-3](https://doi.org/10.1016/S0304-8853(01)00441-3)
231. Vieu C, Carcenac F, Pépin A, et al (2000) Electron beam lithography: Resolution limits and applications. *Appl Surf Sci* 164:111–117. [https://doi.org/10.1016/S0169-4332\(00\)00352-4](https://doi.org/10.1016/S0169-4332(00)00352-4)
232. R.Tyndall Electron beam lithography: resolution limits and applications
233. Altissimo M (2010) E-beam lithography for micro-/nanofabrication. *Biomicrofluidics* 4:. <https://doi.org/10.1063/1.3437589>
234. Cen Shawn Wu YM and CC (2010) High-energy Electron Beam Lihtography for Nanoscale Fabrication. *Intech open* 241–267. <https://doi.org/10.5772/32009>
235. Levinson HJ (2010) Principles of Lithography. SPIE press
236. Arzt A del C and E (2008) Fabrication Approaches for Generating Complex Micro- and Nanopatterns on Polymeric Surfaces. *Chem Rev* 108:911–945
237. Helbert JN, Publishing WA, York N HANDBOOK OF VLSI MICROLITHOGRAPHY
238. Madou MJ (2002) Fundamentals of Microfabrication. CRC Press 1–70
239. Cui B Lithography. 1–35
240. Mladenov GM, Koleva E, Vutova K (2011) Electron lithography of submicron- and nanostructures
241. Liddle JA, Blakey MI, Bolan K, et al (2001) Space-charge effects in projection electron-beam lithography: Results from the SCALPEL proof-of-lithography system. *Am vaccum Soc* 19:476–481. <https://doi.org/10.1116/1.1359174>
242. Greve MM, Holst B (2013) Optimization of an electron beam lithography instrument for fast, large area writing at 10kV acceleration voltage. *J Vac Sci Technol B Microelectron Nanom Struct* 31:. <https://doi.org/10.1116/1.4813325>

243. Zhang Z, Duan H, Wu Y, et al (2014) Improving the adhesion of hydrogen silsesquioxane (HSQ) onto various substrates for electron-beam lithography by surface chemical modification. *Microelectron Eng* 128:59–65. <https://doi.org/10.1016/j.mee.2014.05.027>
244. Allresist (2014) Positive PMMA E-Beam Resists AR-P 630-670 series Investigations of 2-layer PMMA lift-off structures. 15–17
245. Ghosh KP (2009) Process Optimization on Raith-150 TWO E-Beam Lithography Tool for sub-100nm CMOS device fabrication Submitted in partial fulfillment of the requirements. Master Thesis
246. Dhankhar M, Vaňatka M, Urbanek M (2018) Fabrication of Magnetic Nanostructures on Silicon Nitride Membranes for Magnetic Vortex Studies Using Transmission Microscopy Techniques. *J Vis Exp* 1–7. <https://doi.org/10.3791/57817>
247. Puzic A, Van Waeyenberge B, Chou KW, et al (2005) Spatially resolved ferromagnetic resonance: Imaging of ferromagnetic eigenmodes. *J Appl Phys* 97:. <https://doi.org/10.1063/1.1860971>
248. Hellwig O, Berger A, Kortright JB, Fullerton EE (2007) Domain structure and magnetization reversal of antiferromagnetically coupled perpendicular anisotropy films. *J Magn Magn Mater* 319:13–55. <https://doi.org/10.1016/j.jmmm.2007.04.035>
249. Kim KJ, Lee JC, Yun SJ, et al (2010) Electric control of multiple domain walls in Pt/Co/Pt nanotracks with perpendicular magnetic anisotropy. *Appl Phys Express* 3:. <https://doi.org/10.1143/APEX.3.083001>
250. Kim SK, Lee KS, Yu YS, Choi YS (2008) Reliable low-power control of ultrafast vortex-core switching with the selectivity in an array of vortex states by in-plane circular-rotational magnetic fields and spin-polarized currents. *Appl Phys Lett* 92:1–3. <https://doi.org/10.1063/1.2807274>
251. Shimon G, Adeyeye AO, Ross CA (2013) Magnetic vortex dynamics in thickness-modulated Ni80Fe 20 disks. *Phys Rev B - Condens Matter Mater Phys* 87:1–8. <https://doi.org/10.1103/PhysRevB.87.214422>
252. Taniuchi T, Oshima M, Akinaga H, Ono K (2005) Vortex-chirality control in mesoscopic disk magnets observed by photoelectron emission microscopy. *J Appl Phys* 97:. <https://doi.org/10.1063/1.1862032>
253. Huang CH, Wu KM, Wu JC, Horng L (2013) Vortex annihilation in magnetic disks with different degrees of asymmetry. *J Appl Phys* 113:. <https://doi.org/10.1063/1.4795115>
254. Kimura T, Otani Y, Masaki H, et al (2007) Vortex motion in chirality-controlled pair of magnetic disks. *Appl Phys Lett* 90:. <https://doi.org/10.1063/1.2716861>
255. Dumas RK, Gilbert DA, Eibagi N, Liu K (2011) Chirality control via double vortices in asymmetric Co dots. *Phys Rev B - Condens Matter Mater Phys* 83:1–4. <https://doi.org/10.1103/PhysRevB.83.060415>
256. Huang L, Schofield MA, Zhu Y (2010) Control of double-vortex domain configurations in a shape-engineered trilayer nanomagnet system. *Adv Mater* 22:492–495. <https://doi.org/10.1002/adma.200902488>
257. Wu KM, Wang JF, Wu YH, et al (2008) Vortex motion in magnetic disks with different geometric asymmetry. *J Appl Phys* 103:. <https://doi.org/10.1063/1.2834251>
258. Sukhostavets O V., Pigeau B, Sangiao S, et al (2013) Probing the anharmonicity of the potential well for a magnetic vortex core in a nanodot. *Phys Rev Lett* 111:1–5. <https://doi.org/10.1103/PhysRevLett.111.247601>

# List of acronyms and abbreviations

AC – Alternating current  
AMR – Anisotropy Magnetoresistance  
AFM – Atomic Force Microscopy  
AR-P – Allresist-Positive  
AR-N – Allresist-Negative  
ALS –Advanced Light Source  
BOE – Buffered Oxide Etch  
CW – Clockwise  
CCW – Counterclockwise  
CCD – Charged Coupled Device  
CSAR – Chemical Semi-Amplified Resist  
DC – Direct current  
DRAM – Dynamic Random Access-Memory  
DMI - Dzyaloshinskii - Moriya Interaction  
DWL – Direct Write Laser  
EBL- Electron-Beam Lithography  
EBPVD - Electron Beam Physical Vapor Deposition  
FIB – Focused Ion Beam  
GDS – Global Distribution System  
GPIB - General Purpose Interface Bus  
GMR – Giant Magnetoresistance  
HF – Hydrofluoric Acid  
HSQ - Hydrogen Silsesquioxane  
IC – Integrated Circuit  
IBE – Ion Beam Etching  
*IBS – Ion Beam Sputtering*  
IPA – Iso Propyl Alcohol  
LL - Landau – Lifshitz  
LLG - Landau – Lifshitz – Gilbert  
LTEM - Lorentz Transmission Electron Microscopy  
LCP - Left Circularly Polarized  
MRAM- Magnetic Random Access-Memory  
MTJ – Magnetic Tunnel Junction  
MFM – Magnetic Force Microscopy  
MR – Magnetoresistance  
MTXM - Magnetic Transmission X-ray Microscopy  
MOKE - Magneto-Optical Kerr Effect  
MEMS – Microelectromechanical System

MIBK - *Methyl Isobutyl Ketone*  
MH – Magnetic Hysteresis  
NaOH - Sodium Hydroxide  
NEMS –Nanoelectromechanical System  
OOMMF- Object-Oriented MicroMagnetic Framework  
PCB – Printed Circuit Board  
PMMA - Polymethyl Methacrylate  
rf – Radio frequency  
RCP - Right Circularly Polarized  
R&D – Research and Development  
RVM – Rigid Vortex Model  
SIMS - Secondary Ion Mass Spectrometer  
SEM – Secondary Electron Microscopy  
SiN – Silicon Nitride  
STT – Spin-Transfer-Torque  
TMR - Tunnel Magnetoresistance  
TMAH - Tetramethylammonium Hydroxide  
*TDMAT* - Tetrakis Dimethyl Amido Titanium  
UV – Ultra-Violet  
VAV – Vortex- Antivortex-Vortex  
VSM – Vibrating Sample Magnetometer  
XMCD - X-ray Magnetic Circular Dichroism

# List of Symbols

$A$  – Exchange interaction  
 $a$  – Vortex core radius  
 $a_L$  – Lattice parameter  
 $\alpha$  – damping coefficient  
 $a_c$  – Vortex core size  
 $\vec{B}$  – Magnetic induction  
 $B_{sat}$  – Saturation field  
 $B_{nuc}$  – Nucleation field  
 $B_{an}$  – Annihilation field  
 $\beta$  – Disk aspect ratio  
 $\vec{C}$  – Position of vortex core  
 $C, \varphi$  – polar coordinates  
 $c$  – circulation  
 $D$  – Diameter of the disk  
 $\hat{D}$  – Damping constant  
 $\hat{\partial}$  – Partial derivative  
 $e$  – charge of an electron  
 $\varepsilon_{tot}$  – Total energy  
 $\varepsilon_d$  – Dipolar energy  
 $\varepsilon_{ex}$  – Exchange energy  
 $\varepsilon_a$  – Anisotropy energy  
 $\varepsilon_z$  – Zeeman energy  
 $\vec{F}$  – Force  
 $\vec{G}$  – Gyrovector  
 $\vec{H}$  – Magnetic field intensity  
 $\vec{H}_{app}$  – External magnetic field  
 $\vec{H}_{eff}$  – Effective magnetic field  
 $\vec{H}_d$  – Demagnetizing field  
 $\vec{H}_{rf}$  – Radio-frequency field  
 $H_{ext}$  – External static field  
 $\mathcal{H}_{ex}$  – Heisenberg Hamiltonian  
 $h_{ext}$  – RF-Oersted field  
 $J$  – Current density  
 $J_{i,j}$  – Exchange constant  
 $K_u$  – Anisotropy constant  
 $k$  – numerical constant

$\kappa$  – Effective stiffness constant  
 $\kappa_m$  – Stiffness constant of magnetostatic energy  
 $\kappa_{ex}$  – Stiffness constant of exchange energy  
 $L$  – Thickness  
 $l_{ex}$  – Exchange length  
 $\vec{M}$  – Magnetization vector  
 $M_0$  – Spontaneous magnetization  
 $M_s$  – Saturation magnetization  
 $m_e$  – mass of electron  
 $m_x, m_y, m_z$  – The unit magnetization vector component  
 $\hat{N}$  – Demagnetizing factor  
 $p$  – polarity  
 $R$  – Radius of disk  
 $R_{an}$  – Annihilation radius  
 $S_{i,j}$  – Spin alignment  
 $s$  – Vortex core displacement from the center  
 $t$  – time  
 $t_{rise}$  – Rise time  
 $u$  – Spin torque  
 $\mu_0$  – Permeability of free space  
 $\mu_B$  – Bohr magnetron  
 $V$  – Volume  
 $v_{max}$  – Maximum velocity  
 $v_{crit}$  – Critical core velocity  
 $v_s$  – Velocity at position  $s$   
 $W$  – Potential energy  
 $\vec{\omega}$  – Angular velocity  
 $\omega_G$  – Gyrotropic frequency  
 $\chi$  – Vortex core susceptibility  
 $\hat{x}, \hat{y}, \hat{z}$  – Unit vectors  
 $x_{max}$  – Maximum distance of vortex core in x-axis  
 $\gamma$  – gyromagnetic ratio  
 $\lambda$  – Magnetization relaxation  
 $z_c$  – Number of atoms per unit cell  
 $\nabla$  – Hamilton operator



## Own Publications

- [1] Vaňatka M, Urbánek M, Jíra R, Flajšman L, Dhankhar M, Im M-Y, Michalička J, Uhlíř V, Šíkola T,(2017) Magnetic vortex nucleation modes in static magnetic fields. AIP Adv 7:.. <https://doi.org/10.1063/1.5006235>
- [2] Dhankhar M, Vaňatka M, Urbanek M (2018) Fabrication of Magnetic Nanostructures on Silicon Nitride Membranes for Magnetic Vortex Studies Using Transmission Microscopy Techniques. J Vis Exp 1–7. <https://doi.org/10.3791/57817>
- [3] Kaushik P, Basu A, Dhankhar M (2021) Synthesis of Nanomaterials and Nanostructures. CRC Press Taylor Fr Gr 39–48, ISBN 9780367085889.
- [4] Dhankhar M, Urbánek M, Uhlíř V, Vaňatka M, Flajšman L, Šíkola T, Selective Switching of a Magnetic Vortex State. To be submitted.